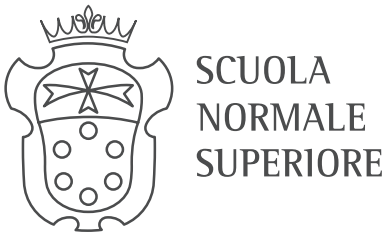


Scuola Normale Superiore

Classe di Scienze

Tesi di Perfezionamento in Methods and Models for Molecular Sciences

XXXIV CICLO

# Polarizable QM/MM Approaches for Molecular Excited States in Complex Environments

Settore Scientifico Disciplinare CHIM/02

*Candidate:*

Dr. Sulejman Skoko

*Supervisor:*

Prof. Chiara Cappelli

Academic Year: 2022/2023

*To my wife Emina*

.

# Acknowledgements

Želio bih da se zahvalim profesorici Chiari Cappeli na pruženoj prilici i mogućnosti da radim i istražujem ono sto volim, hvala za njen veliki doprinos mojoj profesionalnoj karijeri.
Hvala mojim sadašnjim i bivšim kolegama istraživačke grupe Embedlab na profesionalnoj i moralnoj podršci.
Hvala mojoj velikoj familiji, tati Hasibu, mami Azizi, sestri Selmi, bratu Ibrahimu, sestri Sevdi, bratu Kemalu i bratu Harisu. Hvala mojim bliskim prijateljima.
I na kraju, veliko hvala mojoj Ženi za sve.

This thesis has been submitted in partial fulfillment of the requirements for obtaining a Ph.D. degree in Methods and Models for Molecular Sciences at Scuola Normale Superiore di Pisa, Italy, Classe di Scienze. The work was carried out under the supervision of Professor Chiara Cappelli in a four-year period: December 2018 – November 2022. During the first three years of the doctoral studies, the student was enrolled as a fellow in the H2020–MSCA–ITN–2017, Marie Sklodowska Curie Innovative Training Network "COmputational Spectroscopy In Natural sciences and Engineering (COSINE, grant number 765739)".

# Contents

**1 Introduction** **1**

1.1 QM/MM approaches to the spectroscopy of aqueous systems . . . . . 4

1.1.1 Sampling the solute-solvent configurational space . . . . . 4

1.1.2 QM/MM approaches . . . . . 5

1.2 Fully Polarizable QM/FQ approach for the spectroscopy of aqueous solutions 7

1.3 Computational Protocol . . . . . 9

**2 Overview of the Attached Papers** **12**

**3 Simulating Absorption Spectra of Flavonoids in Aqueous Solution: A Polarizable QM/MM Study** **14**

**4 Quantum Mechanics/Fluctuating Charge Protocol to Compute Solvatochromic Shifts** **39**

**5 Towards a Cost-Effective Modeling of Fluorescence in the Condensed Phase** **57**

**6 Summary and Conclusions** **78**

# Papers Attached

1. Simulating Absorption Spectra of Flavonoids in Aqueous Solution: A Polarizable QM/MM Study
   **S. Skoko**, M. Ambrosetti, T. Giovannini, and C. Cappelli, *Molecules*, **2020**, 25(24), p.5853.

2. Quantum Mechanics/Fluctuating Charge Protocol to Compute Solvatochromic Shifts.
   M. Ambrosetti, **S. Skoko**, T. Giovannini and C. Cappelli, *J. Chem. Theory Comput.*, **2021**, 7146-7156

3. Towards a Cost-Effective Modeling of Fluorescence in the Condensed Phase
   **S. Skoko**, C. Micheletti, E. Grifoni, F. Egidi, T. Giovannini, A. Pucci and C. Cappelli, *Dyes and Pigments*, **2023**, p.111227.

# CHAPTER 1

# Introduction

The aim of this Thesis is the application of multi-scale theoretical models to describe excited state properties of molecular systems in solution. In general, solutions consist of a large number of molecules mutually interacting through electrostatic, van der Waals, and hydrogen bonding intermolecular interactions. The intensity and presence of certain interactions depend on the polarity of the solvent.[1] This phenomenon can be observed for example for the Reichard's dye, where a great sensitivity of spectral properties to small changes in solvent polarity is observed, thus clearly indicating the complexity of solvent-solute interactions and solvated systems in general.[2]

In order to model excited state properties of solvated systems, a way to evaluate the excitation energy is needed and fortunately, a number of different theoretical models of increasing accuracy and computational cost have been developed.[3,4] In this thesis results solely based on time-dependent density functional theory (TD-DFT) are reported, due to the fact that such methods are the most widely used for simulating absorption spectra of organic molecules, thanks to their favorable scaling and the availability of a variety of density functionals, which permit to reach a remarkable accuracy at reproducing experimental results[5–14] However, in case of solvated systems the quality of DFT functional and basis set are not the only factors affecting the quality of computed spectra. In fact, solvated systems are complex and the presence of a solvent around a molecule modifies properties, energy, dynamics, and reactivity, in both the ground and excited states. Therefore any absence of solvent effects in the computational modeling can result in simulated spectra in poor agreement with experimental data.[15–28]

A straightforward approach to account solute–solvent interactions is by keeping the same

description as isolated systems, i.e. to consider the solvent and the solute at the same level of theory. Clearly, this way of proceeding would imply to consider a sizable part of the system, thus making the treatment of molecules in solution far more complicated and computationally intractable. This issue can be partly solved by accounting only for a few solvent molecules around the solute, but this approach is not physically consistent with the real solution.[29]

Another way, which is actually the most used in real applications, is to treat the solvent at a lower level of sophistication than the solute. This is possible because the spectral response in the large majority of cases arises from the solute, not from the solvent, which means that the solute has to be always accurately described in all its degrees of freedom, while the solvent can be treated at a lower level of theory. In other words, while the calculation of spectroscopic properties requires a QM description of the solute, the solvent can be treated with classical physics (QM/classical approach).

The key point of the success of QM/classical approaches is to gain accurate modeling of solute-solvent interactions, i.e. of the interaction between the QM and classical portions of the system. Various solvent models have been developed and have achieved great success in modern chemical research because they can be effectively coupled with all QM descriptions, ranging from semi-empirical methods to DFT or Wavefunction Theory (WFT), at a computational cost very close to the QM calculation for the corresponding isolated molecule.

As mentioned above, the challenge of QM/classical approaches is represented by the definition of the solute-solvent coupling term. In fact, after being set, it can be inserted into the solute's QM Hamiltonian through explicit terms; this permits the exploitation of the quantum chemistry machinery to obtain the desired spectral properties in the same way as they are calculated for isolated systems. This permits us to take full advantage of decades of research and development for isolated systems.

Different solvent models exist, which basically differ in the way they describe the separation between the solute and the solvent. The two conceptual alternatives are presented in Fig. 1.1. The most basic protocol uses the implicit polarizable continuum model (PCM).[26,27,30–32] In this model, the environment is described as a polarizable continuum dielectric, where the solute is located in a molecule-shaped cavity (see figure 1.1). However, this protocol fails to account for directional interaction such as hydrogen bonds (HB) which can play an important role. This limitation can be solved by including explicit solvent molecules treated at QM level around the solute, however this approach relies on a static description of the systems and doesn't account for different

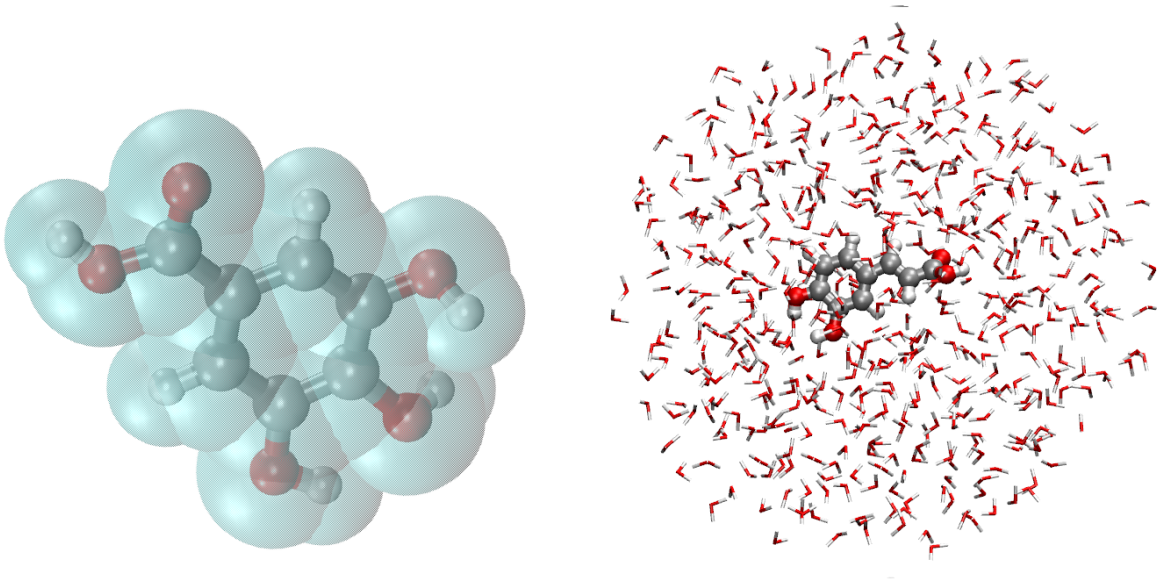

**Figure 1.1.** Implicit solvent model (left) and Explicit solvent model (right)

solute–solvent configurations, while in real situations solvents move around the solute and different configurations need to be sampled.

In order to overcome the limitations of continuum models, fully atomistic (explicit) solvent approaches have been developed over the past years (see figure 1.1, right panel).[33–35] The widest-used explicit solvent model is the Quantum mechanics/molecular mechanics (QM/MM) multiscale scheme in which the system is divided into the portion directly responsible for a spectral property, which is described at QM level, and the surrounding solvent, which is described at the MM (classical) level through ad-hoc constructed force fields (FF). The most basic QM/MM approach only accounts for the electrostatic interaction between the two portions, where MM atoms are assigned fixed pre-parametrized charges. In order to attain a better physical description of the interactions between the QM and MM portions, a number of polarizable QM/MM models have been developed. There, mutual polarization effects are considered.[36–39]

In this Thesis, we specifically focus on the fully polarizable QM/Fluctuating charges (QM/FQ) approach.[40–42] In this scheme, the solute is treated at the QM level, while the solvent is treated at the classical level and is described by a force field, which assigns each MM atom with a charge that can fluctuate in response to the QM potential and due to differences in electronegativity. QM/FQ has been extended to allow calculations of different molecular properties and spectroscopies due to its variational formalism.[35,43–48]

The dynamical aspects of the solvation phenomena are in this Thesis considered by coupling QM/FQ with classical Molecular Dynamics (MD) simulations,[49] which can be performed in a wide range of solvents and by exploiting numerous available force fields.[50] In addition, the force field can be re-parametrized in order to obtain configurations with improved interatomic and intermolecular potentials and/or obtain parameters for systems that lack them, such as in the case of excited states of organic molecules.[51,52]

## 1.1. QM/MM approaches to the spectroscopy of aqueous systems

A successful QM/MM model for spectroscopy needs to correctly describe the physics and chemistry of the solvent-solute system and its interaction with external radiation. In fact, empirical models that are formulated so to fit a certain system's behavior without being based on the underlying solute–solvent interactions, can be very successful in obtaining a specific type of spectroscopic response of a specific set of systems, but totally lack transferability. We will present in the following pages the strategy which has been followed in the next sections.

### 1.1.1. Sampling the solute-solvent configurational space

Solvated systems consist of a large number of mobile molecular subsystems. A reliable sampling of the solute-solvent phase-space is needed to model spectral properties, and to this end classical molecular dynamics (MD), Monte Carlo (MC), or even ab-initio MD can be exploited. This Thesis exploits MD as a sampling methodology; it consists of the numerical (step-by-step) solution of the classical equations of motion, which for a simple atomic system may be written as follows:

$$m_i \ddot{r}_i = f_i = -\frac{\partial}{\partial r_i} U \tag{1.1}$$

Such equations need forces $f_i$ acting on atoms; they are usually derived from the potential energy U($r^N$ ), where $r^N = (r_1, r_2, \ldots r_N)$ represents the complete set of 3N atomic coordinates. Let us take as reference the AMBER[53] FF, which reads:

$$U(r^N) = U_{non-bonded}(r^N) + U_{bonded}(r^N) \tag{1.2}$$

The first term accounts for non-bonded interactions between all atom-pairs, i.e.

$$U_{non-bonded}(r^N) = \sum_{j=i}^{N-1} \sum_{i=j+1}^{N} f_{ij} e_{ij} [(\frac{r_{ij}^0}{r_{ij}})^{12} - 2(\frac{r_{ij}^0}{r_{ij}})^6] + \frac{q_i q_j}{4\pi\epsilon_0 r_{ij}} \tag{1.3}$$

The first term in equation 1.3 accounts for van der Waals interactions, which are calculated using the equilibrium distance ($r_{ij}^0$) between two atom pairs and the well depth ($\epsilon_{ij}$). The second term is a Coulomb-like potential, where $q_i$ and $q_j$ are atomic partial charges and $\epsilon_0$ is the vacuo permittivity.
The bonded potential $U_{bonded}(r^N)$ reads as follows:

$$U_{bonded}(r^N) = \sum_{i \in bonds} k_{bi}(l_i - l_i^0)^2 + \sum_{i \in angles} k_{ai}(\Theta_i - \Theta_i^0)^2 + \sum_{i \in tors} \sum_{n} \frac{1}{2} V_i^n [1 + \cos(n\omega_i - \gamma_i)] \tag{1.4}$$

Bond stretching (first term in eq.1.4) is represented by a simple harmonic function that describes oscillations around the equilibrium bond length $l_i^0$ with force constant $k_{bi}$. The second term describes bending motions, which are also approximated by a harmonic function describing oscillation around the equilibrium angle $\Theta_i^0$ with force constant $k_{ai}$. The last term is the torsion potential, where $\omega_i$ is the torsional rotation angle, n is a non-negative integer that defines periodicity and $\gamma$ is the phase shift angle.
Many families of FF have been developed. AMBER,[53] CHARMM[54] and OPLS20[55] are fitted to large molecules in condensed phases and usually well describe the majority of molecules. However, spectral properties are generally sensitive to the quality of interatomic potentials, therefore a refinement in the parametrization of the force field is required. Luckily, several parametrization tools have been developed, which permit to obtain parameters for systems with poorly described interatomic potential by standard force fields or systems which lacks available FF parameters, such as excited states of organic molecules.[51,56] Also, besides the improvement of molecular interatomic potentials, solvent-solute interactions can be refined by including virtual sites at lone pair positions for atoms involved in strong hydrogen bonding interactions.[57] In this way, a more physically consistent description of the directionality of hydrogen bonding is obtained.[57–59]

### 1.1.2. QM/MM approaches

The total energy of a QM/MM system can be expressed as follows:

$$E = E_{QM} + E_{MM} + E_{QM/MM} \tag{1.5}$$

where $E_{QM/MM}$ represents the interaction energy between the QM and MM portions. $E_{QM/MM}$ can be partitioned as:

$$E = E^{ele}_{QM/MM} + E^{pol}_{QM/MM} + E^{vdW}_{QM/MM} \tag{1.6}$$

where $E^{ele}_{QM/MM}$ is the electrostatic energy, $E^{pol}_{QM/MM}$ is the polarization energy, and $E^{vdW}_{QM/MM}$ accounts for van der Waals contributions, i.e. Pauli repulsion and dispersion energies.

QM/MM approaches can be classified based on the description of $E^{ele}_{QM/MM}$ and $E^{pol}_{QM/MM}$ terms presented in eqn 1.6. In particular, two main classes of methods can be identified:

- Electrostatic Embedding (EE): eqn 1.6 is limited only to the first term ($E^{ele}_{QM/MM}$):

$$E^{EE}_{QM/MM} = E^{ele}_{QM/MM}(\rho_{QM}) = \sum_{i}^{N_q} q_i V i(\rho_{QM}) \tag{1.7}$$

The electrostatic interaction energy is described by a set of fixed charges located on MM atoms, which interact with the QM density. In eqn 1.7 index i runs over the number of charges $N_q$ and $V_i$ is the QM electric potential calculated at the i-th charge $q_i$ placed on the MM portion. $E^{ele}_{QM/MM}(\rho_{QM})$ is expressed in terms of Coulomb's law and it is dependent on QM density.

- Polarizable Embedding (PE): the mutual polarization between the two moieties is considered. Therefore, the coupling between the two portions is expressed as:

$$E^{PE}_{QM/MM} = E^{ele}_{QM/MM}(\rho_{QM}) + E^{pol}_{QM/MM}(\rho_{QM}) = E^{ele}_{QM/MM}(\rho_{QM}) + \sum_{i} x_i(\rho_{QM}) si(\rho_{QM}) \tag{1.8}$$

The various PE approaches differ in the way they describe the polarization energy $E^{pol}_{QM/MM}$ in terms of the QM density $\rho_{QM}$, i.e. in the way the electrostatic quantities $x$ and the QM electric sources $s$ are specified.

In the Drude model[60–67] polarization effects are recovered by including an induced electric dipole at each MM site defined in terms of a couple of charges of the same magnitude but opposite sign connected by harmonic spring. The first charge is fixed and located at the nucleus of the MM atom, where the second charge is mobile and thus polarization arises from the competition between forces acting on harmonic potential.[68] In the Induced dipole model,[38,39,69–75] induced dipoles are assigned to each MM atom, whereas each atom is endowed with isotropic atomic polarizability, from which the induced dipoles are originating as a response to the environment. The induced dipole formalism is also

the basis for a variety of different polarizable QM/MM approaches, which differ by the treatment of the electrostatic part of the force field. In the case of MMpol[76–78] and AMOEBA,[33,79–84] the charge distribution of the solvent is approximated through the dipolar term, where $x = \mu$, while $s$ is in all instances the electric field produced by the QM portion (solute). The electric field $F$ generated by the QM density polarizes the surrounding solvent molecules, by changing their dipoles $\mu$. On the other hand, solvent molecules polarize the QM density and the mutual interactions enter the QM Hamiltonian through an energy term -$\mu E$.

In this work, the Fluctuating Charges (FQ)[85–87] force field is exploited. It will be treated in more detail in the next section, where it is specified for the coupling with a QM Hamiltonian (QM/FQ).

## 1.2. Fully Polarizable QM/FQ approach for the spectroscopy of aqueous solutions

The polarizable QM/FQ approach[35,40,42–46,48,88–96] provides a computationally efficient way of introducing polarization effects in QM/MM calculations. In this model, every atom is endowed with a charge (the fluctuating charge $q$) that is able to fluctuate as a result of differences in atomic electronegativities (electronegativity equalization principle[97,98]). Two sets of parameters are necessary to specify the FQ energy, i.e. atomic hardnesses and atomic electronegativities. The set of charges $q$ can be obtained by minimizing the following functional:[99]

$$F(q,\lambda) = \sum_{\alpha,i} q_{\alpha i}\chi_{\alpha i} + \frac{1}{2}\sum_{\alpha,i}\sum_{\beta,i} q_{\alpha i}J_{\alpha i\beta j}q_{\beta j} + \sum_{\alpha}\lambda_{\alpha}(\sum_{i} q_{\alpha i} - Q_{\alpha}) \tag{1.9}$$

where the greek indices $\alpha$ run over molecules and the Latin $i$ run over the atoms of each molecule. $\lambda$ is a set of Lagrangian multipliers to ensure charge conservation, and J is the Ohno interaction kernel.[100] FQ has been coupled to a QM Hamiltonian. The interaction term is defined as the classical electrostatic interaction in the following equation:

$$E_{QM/FQ} = \sum_{i=1}^{Nq} V_{QM}[\rho](r_i)q_i \tag{1.10}$$

where $V_{QM}[\rho](r_i)q_i$ is the electrostatic potential due to the QM density computed at the i-th $q_i$ placed at $r_i$.

QM/FQ has been extended to compute excitation energies (UV-Vis absorption and fluorescence spectra) through a linear response formalism. For a more detailed discussion on this topic, we refer the reader to Ref. 46. The following matrices, depending on the FQ charges, are defined:

$$\tilde{A}_{ai,bj} = (\epsilon_a - \epsilon_i)\delta_{ab}\delta_{ij} + \langle aj||ib\rangle - \sum_{kl}^{Nq} V_{ia}^{\dagger} D^{-1} V_{jb} \tag{1.11}$$

$$\tilde{B}_{ai,bj} = \langle ab||ij\rangle - \sum_{kl}^{Nq} V_{ia}^{\dagger} D^{-1} V_{bj} \tag{1.12}$$

where $i, j$ are occupied orbitals whereas $a, b$ are virtual orbitals. $\epsilon$ are orbital energies. The sum runs over the molecules in the classical portion and $V$ is the electrostatic potential, while $D$ is the FQ matrix. Then, excitation energies and transition amplitudes are obtained by solving the so-called Casida's equations:

$$\begin{pmatrix} \tilde{A} & \tilde{B} \\ \tilde{A}^* & \tilde{B}^* \end{pmatrix} \begin{pmatrix} X \\ Y \end{pmatrix} = \omega \begin{pmatrix} 1 & 0 \\ -1 & 0 \end{pmatrix} \begin{pmatrix} X \\ Y \end{pmatrix} \tag{1.13}$$

Notice that QM/FQ can be extended so as to give rise to the Fluctuating Charges and Dipoles (QM/FQF$\mu$) method.[47,96,101–104] There, in addition to the fluctuating charges (q), atomic fluctuating dipoles ($\mu$) are assigned to the MM atoms. Both FQs and F$\mu$s vary as a response to the external electric potential and electric field. QM/FQF$\mu$ has also been extended to the linear response formalism, thus allowing the evaluation of absorption and fluorescence spectra.[47]

In order to fully model solvent-solute interactions, exchange-repulsion, and dispersion energy terms need to be considered. Such terms often play an important role in the description of the spectral properties of solvated systems. QM/FQ has been extended to non-electrostatic QM/MM terms by taking advantage of an approach[105,106] which models quantum repulsion as a function of an auxiliary density on the MM portion, while QM/MM dispersion interactions are described by extending the DFT formalism developed by Tkatchenko and Scheffler.[107–110]

This approach is easily coupled to any type of QM/MM model, due to the formulation of repulsion and dispersion terms which is independent of the choice of the electrostatic or polarizable force field.

All QM/MM models need to define and determine a set of parameters to describe the interaction energy between the two portions. This is also the case with the QM/FQ model, which is specified in terms of atomic electronegativities, hardnesses.[42] Model's parameters are responsible for the variation of the degree of mutual polarization, therefore, they directly affect the spectral response of the solute. Appropriate parametrization can be achieved by fitting computed data of selected observables, such as the interaction or total energy with the respect to reference values. A parametrization strategy for different solvents is detailed in Chapter 4. This approach extends the applicability of QM/FQ and sets a procedure that allows the parametrization of a variety of other different solvents.

## 1.3. Computational Protocol

In this section, the computational protocol (see figure 1.2) that has been applied in the following studies is presented. It consists of the following five steps, which are discussed in more detail in Ref.111.

1. Definition of the QM/MM system. Spectral properties of solvated systems are in general determined by the solute, and modified by the solvent. For this reason, focused models, i.e. those that focus the attention on a specific part of the system, are particularly successful. Within the QM/MM framework, defining a focused model means choosing the parts of the systems which will be treated at QM and MM levels. Such a choice depends on the system's chemical properties and its potential interactions with the surrounding environment. In general, the solute molecule is always treated at QM level, while in some special cases, the QM portion can be extended to the nearest solvent molecules. In the particular case of aqueous solutions, such extensions result in including in the QM portion those water molecules which form H-bonds with the solute.

2. Conformational sampling. The actual "computational sample" on which the spectral properties will be computed needs to be defined. A possible way is to resort to MD simulations. There, the degree of flexibility of the molecule can determine the way of modeling the solute during the simulation. In fact, the frozen minimum energy structure of solute can be exploited in "fixed" dynamics in the case of rigid systems. For flexible molecules, such an approximation would not be justified, therefore the configurational space needs to be sampled without freezing any solute degrees of freedom. In all cases, a suitable parametrization is

needed, and this is even more important for flexible systems. In the majority of cases, standard parametrization engines perform reasonably well, but sometimes, refinement of parameters is required in order to increase the quality of the sampling and therefore the spectral properties. In some specific cases, such as excited states, which will be shown in the following studies, appropriate re-parametrization is necessary. In addition to intramolecular structural changes, reliable sampling of solvent configurations around the solute is as important as the quality of the interatomic potential of the solute molecule. Furthermore, it is necessary that MD simulations are long enough to take into account all possible conformational changes and that FF parameters correctly reproduce all possible system configurations. Sampling the phase space of solutions using classical Molecular Dynamics has been performed in all the following studies, where temperature and pressure are chosen to mirror the desired experimental setup.

3. Extraction of structures. A number of representative snapshots are extracted from MD runs and treated for further QM/MM calculations. Snapshots are spherical droplets that are obtained by cutting spheres of given radii centered on the solute from standard MD boxes. The radius of the droplets is chosen to be large enough to account for all solvent-solute interactions in a physically consistent way. The total number of snapshots is chosen so as to reach convergence of desired spectral properties and it can vary depending on the system and property to be modelled.

4. QM/MM simulations. The QM level of theory, MM force field, and model for the coupling of the QM and MM portions needs to be chosen. Then, a QM/MM calculation of the spectral property is performed on each droplet.

5. Spectra extraction. First, raw stick spectra are extracted from each droplet and collected to produce final stick spectra (raw data). Then, UV/Vis spectra are obtained from stick spectra through a convolution procedure on each stick. The final spectra are then compared with experimental or other reference data. If the quality of the comparison is low, all the steps above are possibly refined.

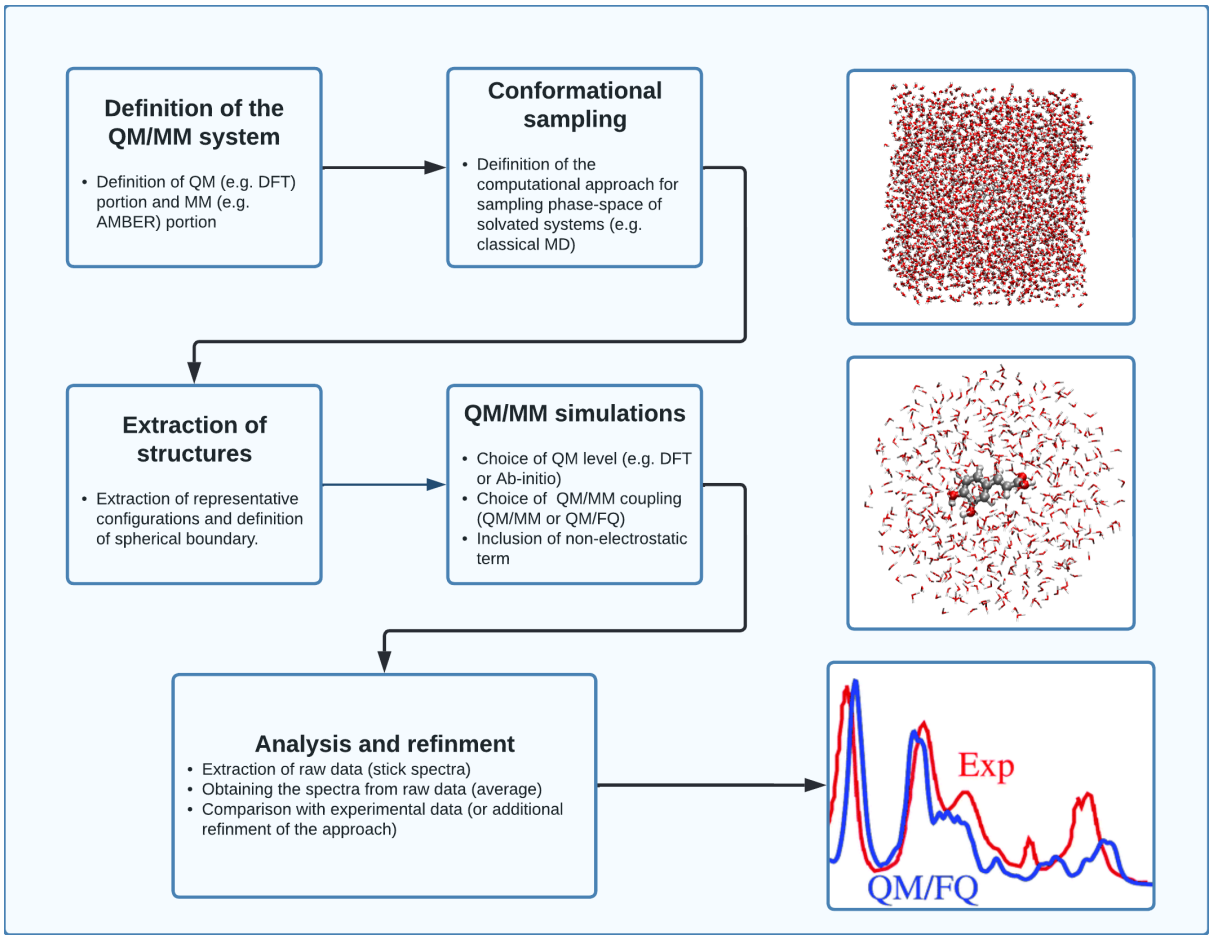


**Figure 1.2.** Schematic view of the employed computational protocol

# CHAPTER 2

## Overview of the Attached Papers

In **Paper 1**, a computational study of UV/Vis spectra of four flavonoids (luteolin, kaempferol, quercetin, and myricetin) in aqueous solution is presented. Spectra are simulated by the fully polarizable QM/MM model based on the fluctuating charge (FQ) force field, coupled with configurational sampling obtained by performing classical molecular dynamics (MD) simulations. The description of solute-solvent hydrogen bonding (HB) interactions is refined by exploiting "virtual sites" (VS) located at lone pair positions of each oxygen site. MD is analyzed in terms of radial distribution functions of oxygen sites and dihedral distribution functions of selected angles, that in order to obtain information about hydrogen-bonding interactions and their effect on the rotation freedom of selected dihedral angles during MD runs. The QM/FQ spectrum of each flavonoid has been computed on a set of 300 uncorrelated snapshots and compared with the experimental data. The comparison shows that $MD_{VS}$ coupled with QM/FQ provides the best agreement, probably due to better configurational sampling and HB description.

In **Paper 2**, a novel parametrization of QM/FQ for non-aqueous environments is discussed. In particular, a machine learning-based parametrization procedure is proposed and applied to find a parametrization of dioxane, tetrahydrofuran, acetonitrile, ethanol, and methanol. In order to challenge the model, QM/FQ calculations are performed with the new set of parameters in order to reproduce solvatochromic shifts of selected dyes of increasing physicochemical complexity. Computed and experimental solvatochromic shifts are compared, along with a comparison with the implicit QM/PCM and a non-polarizable QM/MM approach.

In **Paper 3**, a reliable and cost-effective computational protocol that is capable of

accurately describing fluorescence spectra in an aqueous solution is proposed. Besides strong hydrogen bonding interactions, the model also considers dynamic aspects of the solvation phenomenon in both the ground (GS) and, remarkably, excited state (ES). The approach is tested on acetone, for which different methods are applied, and their quality is evaluated against experimental values.The computational protocol is also challenged to reproduce experimentally measured spectra of selected water-soluble fluorescent dyes, of applicative interest. An almost perfect agreement is reported, thus confirming the robustness and reliability of the methodology.

# CHAPTER 3

# Simulating Absorption Spectra of Flavonoids in Aqueous Solution: A Polarizable QM/MM Study

molecules

MDPI

Article

# Simulating Absorption Spectra of Flavonoids in Aqueous Solution: A Polarizable QM/MM Study

**Sulejman Skoko [1], Matteo Ambrosetti [1], Tommaso Giovannini [2] and Chiara Cappelli [1,*]**

[1] Scuola Normale Superiore, Piazza dei Cavalieri 7, I-56126 Pisa, Italy; sulejman.skoko@sns.it (S.S.); matteo.ambrosetti@sns.it (M.A.)
[2] Department of Chemistry, Norwegian University of Science and Technology (NTNU), 7491 Trondheim, Norway; tommaso.giovannini@ntnu.no
* Correspondence: chiara.cappelli@sns.it

Academic Editors: Demeter Tzeli and Stacey Wetmore
Received: 23 November 2020; Accepted: 7 December 2020; Published: 11 December 2020


**Abstract:** We present a detailed computational study of the UV/Vis spectra of four relevant flavonoids in aqueous solution, namely luteolin, kaempferol, quercetin, and myricetin. The absorption spectra are simulated by exploiting a fully polarizable quantum mechanical (QM)/molecular mechanics (MM) model, based on the fluctuating charge (FQ) force field. Such a model is coupled with configurational sampling obtained by performing classical molecular dynamics (MD) simulations. The calculated QM/FQ spectra are compared with the experiments. We show that an accurate reproduction of the UV/Vis spectra of the selected flavonoids can be obtained by appropriately taking into account the role of configurational sampling, polarization, and hydrogen bonding interactions.

**Keywords:** flavonoids; QM/MM; MD; QM/FQ; absorption spectrum; UV/Vis

## 1. Introduction

Flavonoids belong to the family of polyphenolic secondary metabolites, which are widely found in natural products, such as vegetables and fruits [1]. In particular, their structure derives from phenylchromene, which after being hydroxylated or methoxylated in different positions leads to the different flavonoid compounds [2]. Flavonoids have attracted much interest, due to their biochemical and antioxidant effects which might be beneficial to treat different diseases such as cancer, Alzheimer's disease, and atherosclerosis [3–5]. Thanks to their antioxidant and anti-inflammatory properties, together with their ability to inhibit enzyme functions, a large number of flavonoid compounds have been used in a plethora of medicinal, pharmaceutical, and cosmetic applications [6–8]. Recently, flavonoids have been proposed as potential drugs for therapeutics against coronavirus disease 2019 (COVID-19) [9–11].

In addition to their therapeutic usages, flavonoids play a crucial biological activities in plants and animals [12–16]. In plants, flavonoids are responsible for the colour and aroma of flowers and fruits [17–20]. One of the most relevant examples is given by wine, and in particular red wine, in which flavonoids provide organoleptic and disease prevention properties [21–26].

Flavonoids also protect plants thanks to their ability to filter the UV radiation, indicating unique optical properties [27]. The latter are very sensitive to the environment, for instance flavonoids' maximum UV/Vis absorption occurs at different wavelengths when they are dissolved in different solvents. However, flavonoids natural environment is water, which is ubiquitous in both vegetables and fruits [28–30]. In this work, we model the absorption spectra of Luteolin (**L**), Kaempferol (**K**), Quercetin (**Q**), and Myricetin (**M**) in aqueous solution (see Figure 1 for their molecular structures) [28]. Luteolin is a yellow dye, which can be derived from the plant Reseda luteola [31]; kaempferol can

be found in different vegetables [32], whereas quercetin and myricetin are among the most diffuse flavonoids in red wine [24,33,34]. As it can be noticed from Figure 1, all selected flavonoids are characterized by several OH groups, which can be involved in Hydrogen Bonding (HB) interactions with the surrounding aqueous environment.

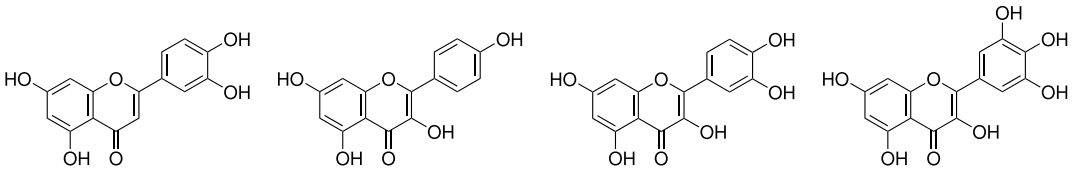


**Figure 1.** Molecular structure of the studied Flavonoids.

From the theoretical point of view, in order to accurately simulate the absorption spectra of dyes in aqueous solution, both the solute and the solvent molecules have to be described atomistically to capture specific solute–solvent interactions, such as HB [35–38]. These kinds of problems are usually treated by resorting to the so-called focused models [35,39–42], which are based on the assumption that the solute gives rise to the spectral property, which is modified, but not determined, by the external environment. Within this framework, the solute is treated at the Quantum Mechanical (QM) level, whereas the solvent is described classically either by exploiting an implicit continuum approach [40,43], or an explicit atomistic model. When specific (HB) interactions take place between the solute and the solvent, the atomistic description of the environment usually overperforms the implicit continuum approach [37,44–47]. In most atomistic approaches, the solvent is described by means of a classical force field (FF), resulting in the QM/Molecular Mechanics (QM/MM) methods, in which the interaction between the QM and MM portions is described in terms of classical electrostatics [48–51]. The mutual polarization between the two portions can be introduced by resorting to polarizable QM/MM methods [52–58].

In this work, the absorption spectra of the selected flavonoids in aqueous solution (see Figure 1) are calculated by exploiting the polarizable QM/Fluctuating Charge (QM/FQ) approach [35,36,42]. In this scheme, the solute is treated at the QM level, and the solvent water molecules are described by means of the FQ force field [59–61]. In particular, each MM atom is endowed with a charge, which can fluctuate as a response to the QM potential [54]. The FQs enter in the definition of the QM Hamiltonian and the Self Consistent Field procedure is iterated until a mutual solute–solvent polarization is reached [54]. The QM/FQ method is usually coupled with classical Molecular Dynamics (MD), which allows for taking into account the dynamical aspect of the solvation phenomenon [46,62–64]. Such an approach has been shown to be particularly suitable to accurately describe the properties of aqueous solutions [35,36]. Major details on its approach can be found in a recent review by some of the present authors [35].

The manuscript is organized as follows. In the next section, we discuss the computational protocol which is exploited in the calculations. The numerical results and a discussion of the main findings of the present study are then presented. A summary and some conclusions end the manuscript.

## 2. Results and Discussion

In this section, we first discuss the computational protocol exploited in the calculations. Then, MD results for each flavonoid depicted in Figure 1 are presented, by analyzing conformational distributions of the main dihedral angles and hydrogen bonding patterns. Then, QM/FQ absorption spectra are presented and compared to experiments.

### *2.1. Computational Protocol*

In order to investigate the electronic properties of the selected molecules dissolved in aqueous solution, we rely on a well established multi-step computational protocol [35,36]:

1. Definition of the system. The geometry of each of the four flavonoids depicted in Figure 1 was first optimized by resorting to an implicit Polarizable Continuum Model (PCM) [40] description of the solvent, and then surrounded by a number of randomly-placed water molecules large enough to represent the solvation shell.
2. Classical MD simulations. An equilibration (NPT) and a subsequent production (NVT) runs were performed in order to sample the system under study. In particular, MD production runs were carried out for each of the four molecules for a time long enough to obtain an accurate sampling of the phase space, in order to correctly reproduce all possible system configurations and their relative energy.

   In order to recover the directionality of hydrogen bonding (HB) interactions, we also placed off-site charges (the so-called virtual sites (VS) or dummy atoms) to better describe the lone pairs of the Oxygen atom (see Figure 2 for a graphical representation) [44,65,66]. Therefore, two different classical MD simulation runs were performed for each molecule, i.e., with or without the inclusion of VS ($MD_{VS}$ or $MD_{noVS}$, respectively). From MD runs, a set of snapshots was extracted to be used in QM/FQ calculations.
3. Definition of the different regions of the two-layer QM/FQ scheme and their boundaries. For each snapshot extracted from MD runs, a sphere centered on the solute was cut. The radius of the droplet was chosen to retain specific solute–water interactions.
4. QM/FQ calculations and comparison with experimental data reported in [28,67]. QM/FQ excitation energies calculations were performed on the set of structures obtained for the four molecules at step 2 of the protocol. The results obtained for each spherical snapshot were then extracted and averaged to produce the final spectrum, which was compared with experiments.

All QM calculations were performed using a locally modified version of the Gaussian16 suite [68]. In all instances, the B3LYP functional in combination with the 6-311+g(d,p) basis set were employed. All MD runs were performed by using the GROMACS package [69]. The GAFF force field was adopted to describe both intramolecular and intermolecular interactions of the solutes [70]. The TIP3P force field was used to describe water molecules [71]. In order to refine the solute electrostatic interactions, RESP charges [72] were computed at the B3LYP/6-311 + g(d,p) level of theory. Electrostatic interactions were treated by using the particle–mesh Ewald (PME) method with a grid spacing of 0.16 Å and a spline interpolation of order 4 [73]. The cross-interactions for Lennard–Jones terms were calculated using the Lorentz–Berthelot mixing rules and intramolecular interactions between atom pairs separated up to three bonds were excluded.

A single molecule was dissolved in a cubic box containing at least 2500 water molecules. In $MD_{VS}$, the position of virtual sites was determined by performing a molecular orbital localization by means of the Boys procedure [74]. In particular, a pair of VS was assigned to each Oxygen atom (green spheres in Figure 2). The charge of each oxygen atom was uniformly split between its virtual sites.

The molecular systems were initially brought to 0 K applying the steepest descent minimization procedure and then heated to 298.15 K in an NVT ensemble using the velocity-rescaling [75] method with an integration time step of 0.1 fs and a coupling constant of 0.1 ps for 200 ps. A 500 ps long NPT run was performed, using the Parrinello–Rahman barostat and a coupling constant of 1.0 ps, to obtain a uniform distribution of molecules in the box and for thermalization purposes. Finally, 30 ns long MD production runs were carried out in the NVT ensemble, with a 0.1 fs time step.

A snapshot every 100 ps was extracted in order to obtain a total of 300 uncorrelated snapshots for each system. From each snapshot, a solute-centered sphere with radius 15 Å was cut. For each obtained

droplet, the solute excitation energies were computed using the polarizable QM/FQ model [35,36,42]. The QM portion was treated at the B3LYP/6-311+g(d,p) level. The FQ SPC parametrization proposed by Rick et al [59]. was exploited. All computed absorption spectra were convoluted with a Gaussian band shape with a Full Width at Half Maximum (FWHM) of 0.37 eV, and then averaged to obtain the final spectrum.

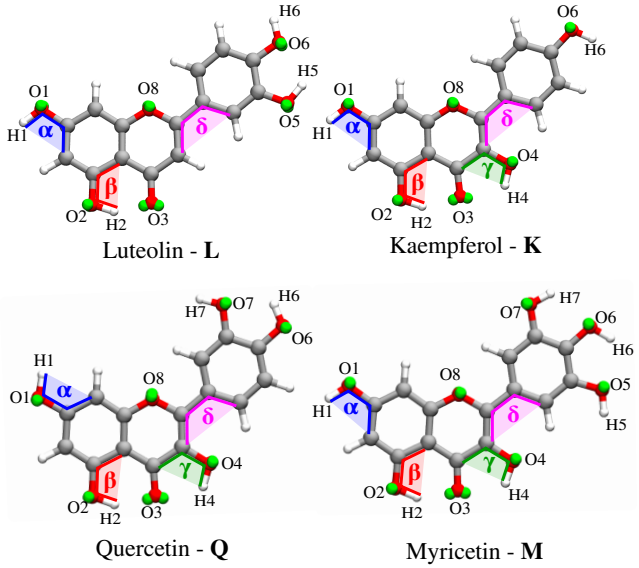


**Figure 2.** Atom labeling and definition of dihedral angles and oxygen virtual sites for the four flavonoids.

## 2.2. MD Analysis

The analysis of each MD trajectory was performed by using the TRAVIS package [76]. Two different observables are presented and discussed: the radial distribution function (RDF) and the dihedral distribution function (DDF). Then, hydration patters defining HB interactions are discussed for the atomic sites highlighted in Figure 2. All results are commented for both $MD_{noVS}$ and $MD_{VS}$.

### 2.2.1. Conformational Analysis Based on MD Simulations

DDFs were extracted for four dihedral angles ($\alpha$, $\beta$, $\gamma$, $\delta$, see Figure 2 for their definition) from both $MD_{VS}$ and $MD_{noVS}$. $\alpha$, $\beta$, and $\gamma$ represent the dihedral angle between the molecular plane and the selected hydroxyl groups, whereas $\delta$ describes the relative orientation of the phenyl group with respect to the main molecular plane (see Figure 2). The $\alpha$, $\beta$, $\gamma$ DDFs for Myricetin **M** as obtained from both $MD_{noVS}$ and $MD_{VS}$ are reported in Figure 3. The same DDFs for the other flavonoids are reported in Figures S1–S3 in the Supplementary Materials (SM).

The $\alpha$ DDF depicted in Figure 3 is centered at 0 and 180 degrees, with a range of variability of about 50 degrees. This indicates that the hydroxyl group involved in the definition of $\alpha$ presents a high rotation freedom. In addition, all studied molecules present similar $\alpha$ DDFs (see Figures S1–S3 in the SM), showing that the different number of OH groups on the phenyl moiety does not affect $\alpha$ conformational stability. The $\beta$ and $\gamma$ DDFs are characterized by a sharp distribution centered at zero degrees. Such a low rotational freedom of the selected hydroxyl groups is due to the intramolecular interaction which is established with the carboxyl Oxygen atom (O3, see Figure 2). In addition, the narrower spreading of $\beta$ as compared to $\gamma$ can be attributed to the highest stability of the six-term ring with respect to the five-term ring formed for the two angles, respectively. Similarly to $\alpha$, the distributions of both $\beta$ and $\gamma$ angles are not affected by the different number of OH groups in the phenyl moiety (see Figures S1–S3 in the SM). As a final comment on $\alpha$, $\beta$, and $\gamma$, we note that a

qualitatively analog conformational analysis can be obtained by using both $MD_{noVS}$ and $MD_{VS}$ (left and right panels of Figure 3).

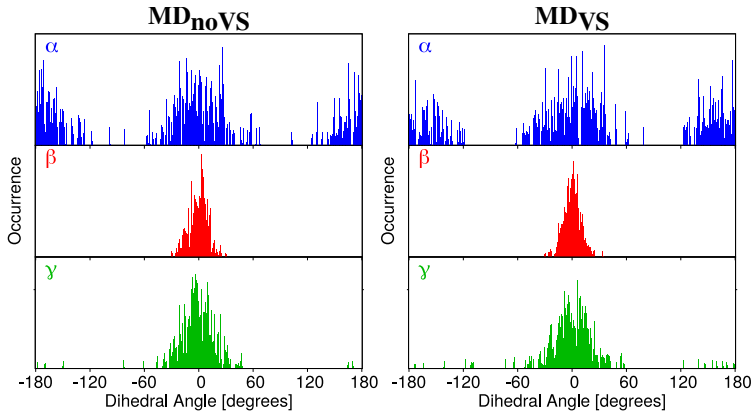


**Figure 3.** DDF of $\alpha$ (top,blue), $\beta$ (middle,red) and $\gamma$ (bottom,green) dihedral angles of Myricetin (**M**) as obtained from $MD_{noVS}$ (**left**) and $MD_{VS}$ (**right**).

In Figure 4, $\delta$ DDFs for all studied molecules are graphically depicted. The distribution of $\delta$ dihedral angle gives insight on the planarity of the molecules because it represents the relative orientation of the two main portions of the system. We first note that $\delta$ DDFs for **K**, **Q**, and **M** are not characterized by a main preferential angle, and two different configurations can be identified, centered at $\pm$60 and $\pm$120 degrees. Therefore, for such systems, the two main portions never lie on the same plane. Such a consideration is valid for both $MD_{noVS}$ and $MD_{VS}$. A different picture arises for **L** $\delta$ DDF. In particular, in case of $MD_{noVS}$, the same preferential angles reported for the other molecules can be identified; however, the planar configuration is also sampled. When a more accurate description of the directionality of molecule–water interactions is taken into account by including virtual sites in the MD ($MD_{VS}$), the $\delta$ DDF has two main peaks centered at about $\pm$60, thus showing largest molecular stiffness. Therefore, the absence of the OH group involved in the definition of $\gamma$ dihedral angle significantly affects the rigidity of the molecule.

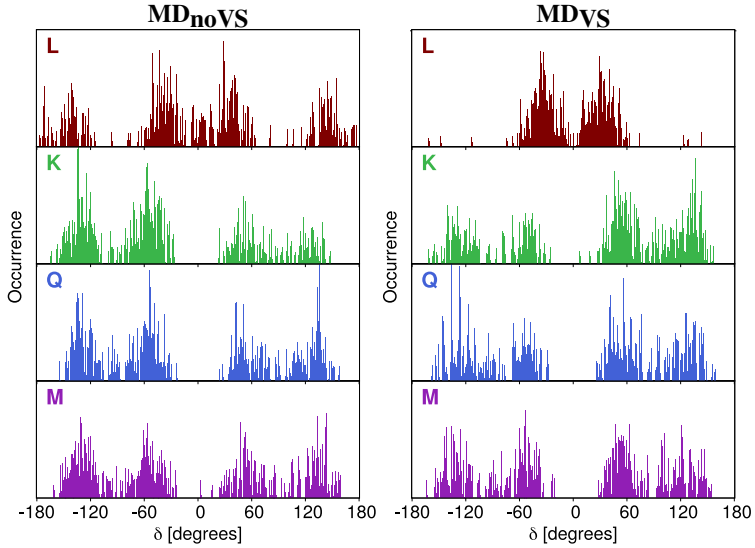


**Figure 4.** DDF of $\delta$ dihedral angle of **L** (brown), **K** (green), **Q** (blue) and **M** (purple) as obtained from $MD_{noVS}$ (**left**) and $MD_{VS}$ (**right**).

### 2.2.2. Hydration Pattern

All studied flavonoids are characterized by several hydroxyl groups, which can strongly interact with the surrounding water molecules via HBs. In order to study hydration patterns in aqueous solutions, both $MD_{noVS}$ and $MD_{VS}$ were analyzed by extracting RDFs between flavonoids' Oxygen atoms and water Hydrogen atoms (Hw). Myricetin RDFs for all interacting sites are depicted in Figure 5. We focus on this system because it is characterized by the largest number of hydroxyl groups; similar data for Luteolin, Kaempferol, and Quercetin are collected in Figures S4–S6 in the SM.

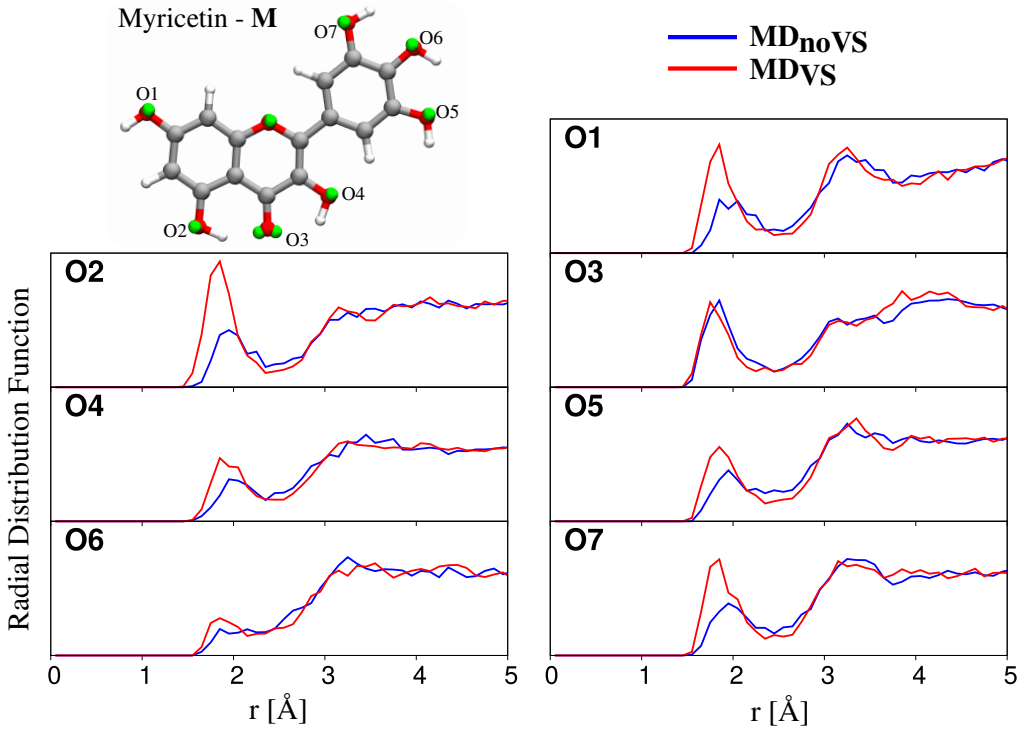


**Figure 5.** Radial distribution functions (RDFs) between Oxygen atoms of Myricetin and water Hydrogen atoms, as obtained from $MD_{noVS}$ (blue) and $MD_{VS}$ (red) runs.

All RDFs reported in Figure 5 show a peak at about 1.8 Å, of which the intensity varies for the different oxygen atoms. In particular, in most cases, a strong HB interaction is present (high intensity peak), whereas, for O6, a weaker interaction is reported in both $MD_{noVS}$ and $MD_{VS}$. Such a behavior can be explained by considering that the O6 hydroxyl group is involved in HB interactions with both O5 and O7 hydroxyl groups. This is confirmed by the fact that O6 RDFs computed for the other flavonoids do not show any significantly lower intensity with respect to RDFs related to the other Oxygen atoms (see Figures S4–S6 in SM).

The inclusion of off-site VSs has two main effects: the intensities of the RDF first peaks increase and their maxima are located at shorter *r* distances, thus indicating that a stronger solute–solvent HB interaction is described. The only notable exception is O3; however, such a behavior is not unexpected because O3 is involved in intramolecular HB between O2 and O4 hydroxyl groups. The inclusion of VSs better describes such an interaction, without affecting solute–solvent HBs.

To further analyze hydration patterns, we also computed the number of water molecules interacting with each flavonoid molecule, by extracting from MD runs the running coordinating number (RCN), see Table 1. The latter is the integral of the RDF first peak, and is related to the average number of water molecules in the first solvation shell interacting with the selected oxygen site. We first notice that, for all molecules, each oxygen site is bonded to water by at least one HB interaction;

the only notable exception is O6 of myricetin, thus further confirming the comments above. Overall, the number of HBs is larger for $MD_{VS}$ than $MD_{noVS}$. This is again not surprising, and it is due to the fact that the inclusion of VSs allows for a refined, and more physically consistent, description of flavonoid–water HB interactions. In addition, a different picture arises for O3; in this case, a decrease in the number of hydrogen-bonded water molecules is reported for all the studied molecules. In fact, the inclusion of VSs leads to a stronger intramolecular HB interaction, with a consequent decrease of intermolecular HBs with water molecules.

**Table 1.** Running coordination number (RCN) of the studied Oxygen sites of the different flavonoids as obtained from $MD_{noVS}$ and $MD_{VS}$ (in parentheses). See Figure 2 for atom labeling.

| Site | L | K | Q | M |
|---|---|---|---|---|
| O1 | 1.1 (1.5) | 1.4 (1.6) | 1.0 (1.6) | 1.2 (1.5) |
| O2 | 1.3 (1.9) | 1.6 (1.7) | 1.2 (1.8) | 1.0 (1.6) |
| O3 | 1.8 (1.6) | 1.4 (1.1) | 1.4 (1.2) | 1.3 (1.2) |
| O4 | – (–) | 1.1 (1.3) | 1.1 (1.4) | 0.8 (1.1) |
| O5 | 1.0 (1.4) | – (–) | – (–) | 0.9 (1.2) |
| O6 | 0.9 (1.3) | 1.3 (1.7) | 0.9 (1.0) | 0.2 (0.5) |
| O7 | – (–) | – (–) | 1.0 (1.4) | 1.1 (1.3) |

### *2.3. Excitation Energies*

QM/FQ excitation energies were calculated on 300 uncorrelated snapshots extracted from MD trajectories; such a number was chosen to assure the convergence of the final spectra. All calculations were performed at the TD-B3LYP/6-311 + G(d,p) level, and the first 20 excited states were computed. QM/FQ raw data recovered from each set of snapshots are reported as stick spectra in Figure 6 for the case of $MD_{noVS}$runs. As it can be noticed, a large variability both in band intensities and energies is predicted for all flavonoids, similarly to what has already been reported for other systems dissolved in aqueous solution [77–79]. Similar stick spectra were obtained from snapshots extracted from $MD_{VS}$ (see Figure S7 in the SM). Stick data were then convoluted by using a Gaussian function (with FWHM = 0.37 eV), and averaged to obtained the final computed UV/Vis spectra, which are also depicted in Figure 6.

The convoluted spectrum of each flavonoid is characterized by two main bands. The first is placed at about 3.4 eV (364 nm) for **K**, **Q** and **M**, whereas for **L** it is blueshifted by about 0.15 eV (349 nm); the second band is centered in the region 4.7–5 eV (264–248 nm) for all systems. For **K**, **Q**, and **M**, the spectrum is dominated by the second peak, whose intensity is almost twice that of the first band. A different situation is reported for **L**, for which the two bands have almost equal intensities. The first band at about 3.4–3.6 eV (364–344 nm) is due to a pure HOMO–LUMO transition, whereas the second band results from a combination of several excitations. In order to investigate the nature of the first electronic transition, the involved molecular orbitals (MOs) are plotted in Figure 7. We see that the first excitation can easily be identified as a $\pi - \pi^*$ transition. In particular, we note that the carbonyl Oxygen atom (O4) takes part into the electronic excitation. Therefore, the differences between **L** and the other flavonoids reported for the first transition can be ascribed to the fact that in **K**, **Q**, and **M**, O3 is hydrogen bonded to the O4 hydroxyl group (see Figure 7, right), whereas in **L** O3 is free to form a (weak) HB interaction with the surrounding water molecules. As a consequence, the $\pi - \pi^*$ excitation is redshifted by about 0.15 eV for **K**, **Q**, and **M**. Figure 7 also reports excitation energies of the first electronic transition for both $MD_{noVS}$ and $MD_{VS}$. Moving from **K** to **Q** and **M**, a redshift is described by both MDs. This behavior can be explained by considering that the number of hydroxyl groups increases moving from **K** to **M**. As a consequence, a larger number of HB sites with the surrounding water molecules are involved, yielding a redshift which is typically observed for $\pi - \pi^*$ transitions [38,80–83]. Such a redshift is not present in **Q** and **M** because the bridge OH group in M is only weakly involved in HB interactions with the solvent (see Table 1). We also note that

$MD_{VS}$ always predicts higher excitation energies than $MD_{noVS}$. This is not surprising and it is once again related to the reduced number of water molecules hydrogen bonded to O3 (see Table 1).

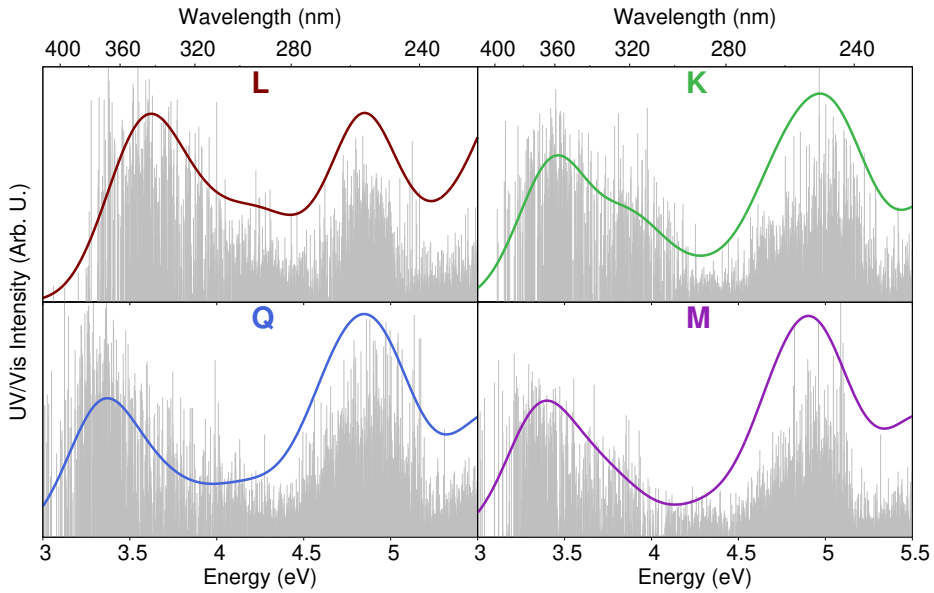


**Figure 6.** QM/FQ UV/Vis stick spectra of each studied flavonoid computed on 300 snapshots extracted from $MD_{noVS}$. Convoluted QM/FQ spectra are also plotted in color.

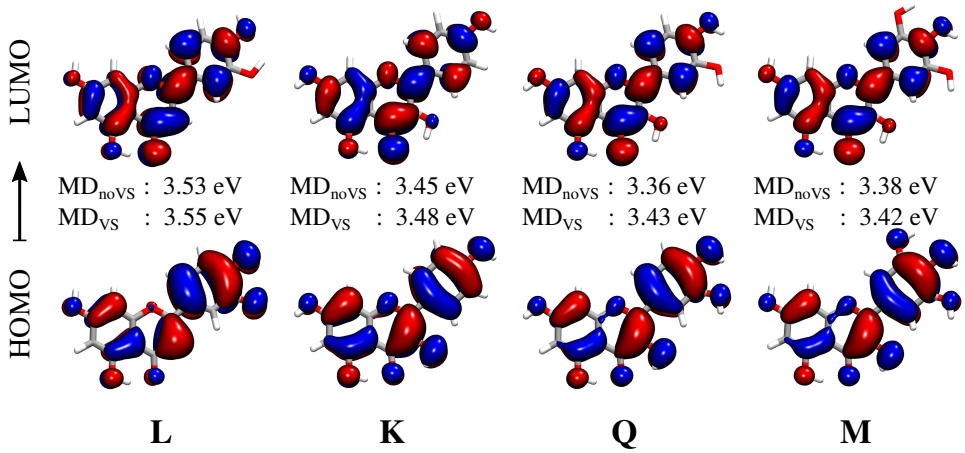


**Figure 7.** Molecular Orbitals (MOs) involved in the first electronic transition of each flavonoid. The corresponding excitation energies are also given for both $MD_{VS}$ and $MD_{noVS}$. Isovalue: 0.02.

As mentioned above, a large spreading in both energies and intensities is reported in stick spectra depicted in Figure 6. In order to investigate the origin of such a variability, we studied how the excitation energy depends on the dihedral angles previously analyzed (see Section 2.2.1). In particular, Figure 8 reports computed excitation energies of the first transition as a function of the $\delta$ dihedral angle (see Figure 2 for its definition). Similar plots for $\alpha$, $\beta$, and $\gamma$ are given in Figures S8–S10 in the SM. We see that the computed values are clusterized around the most populated dihedral angles for both MD runs (see Figure 4). In addition, independently from the value of the dihedral angle, computed energies span the region between 2.9 and 3.9 eV. This demonstrates that the origin of the

large variability reported in the stick spectra is the spatial arrangement of water molecules around the solutes.

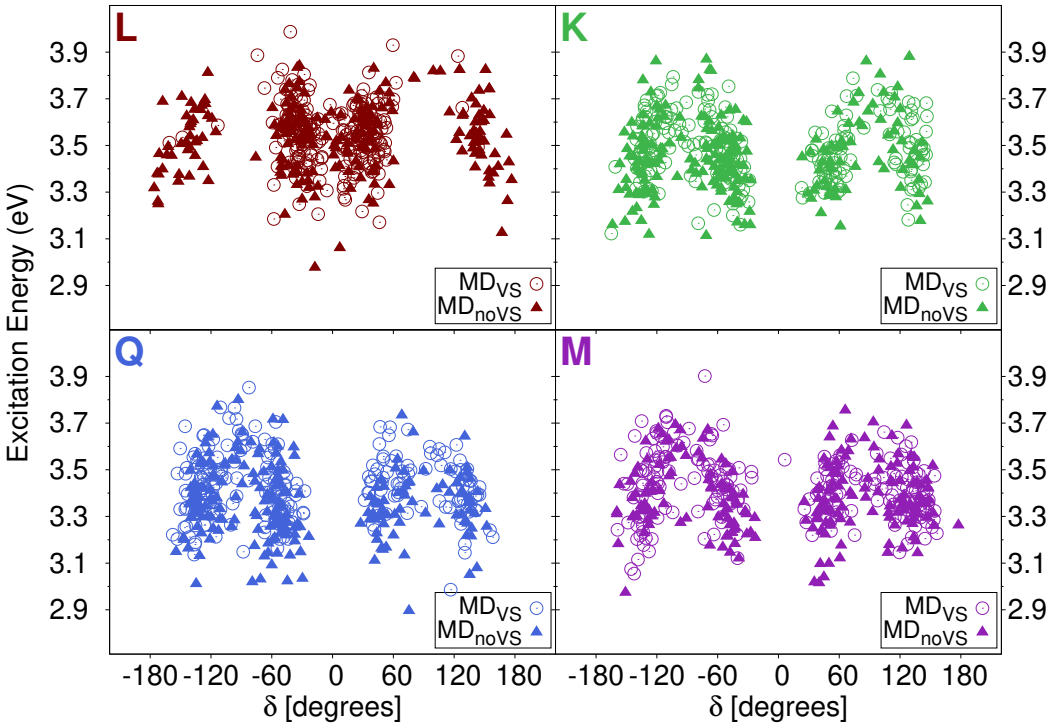


**Figure 8.** QM/FQ Excitation Energies of the first electronic transition of each studied flavonoid as a function of $\delta$ dihedral angle.

We finally move to the comparison between computed and experimental spectra, the latter reproduced from Refs. [28,67]. Such a comparison is shown in Figure 9. The experimental absorption spectrum of each molecule is characterized by two main peaks, the first lying at about 3.4 eV (365 nm) for **K**, **Q**, and **M** and 3.6 eV (345 nm) for **L**. The second peak is placed in the region 4.7–5 eV, and has a different shape for each flavonoid. In particular, for **L** and **M**, two peaks are present, probably due to vibronic coupling [84–86]. In addition, for **L** and **Q**, the first peak is the most intense one, whereas the opposite holds for **K**. For **M**, the intensities of the two bands almost coincide.

The agreement between QM/FQ and experimental spectra is excellent for all flavonoids, especially if QM/FQ is combined with $MD_{VS}$runs. In fact, the main difference between $MD_{VS}$ and $MD_{noVS}$ results is the relative intensity of the two band. For **K**, **Q**, and **M**, $MD_{noVS}$ underestimates the intensity of the first transition with respect to the experimental findings. Therefore, a refined modeling of intermolecular interactions by means of off-site VSs seems to be crucial to achieve an accurate reproduction of the general shape of the experimental spectra. The only notable exception is **L**, for which the experimental second band lies in between $MD_{noVS}$ and $MD_{VS}$. However, the overall agreement between the experimental and computed spectra is not compromised.

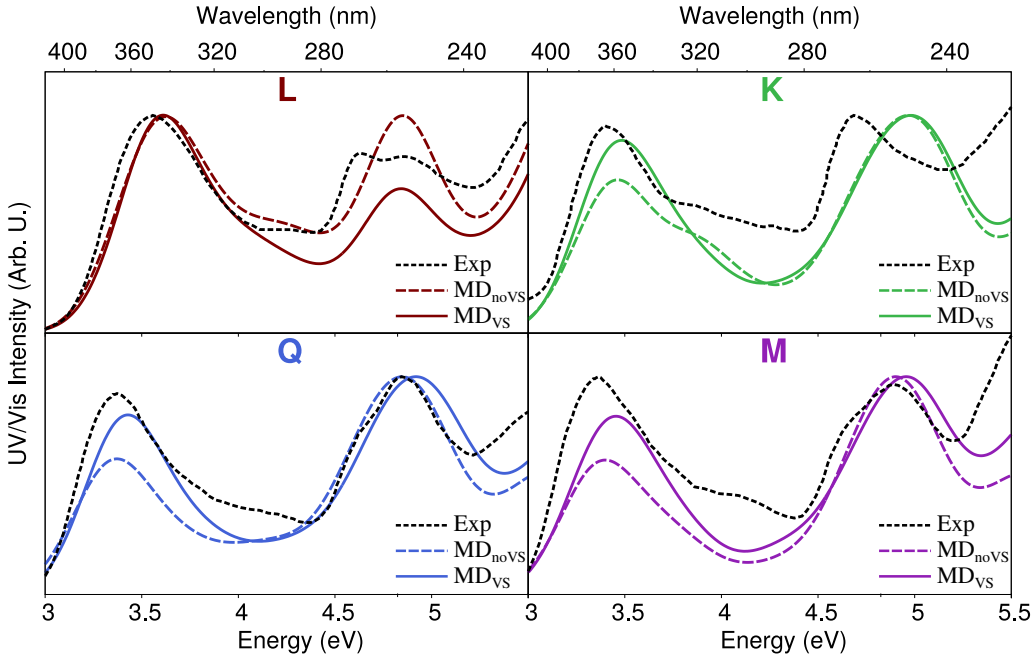


**Figure 9.** Computed absorption spectra of each studied flavonoid in aqueous solution obtained by using QM/FQ coupled with both $MD_{VS}$ and $MD_{noVS}$. Experimental UV/Vis spectra reproduced from Refs. [28,67] are also reported.

## 3. Summary and Conclusions

In this work, UV-Vis absorption spectra of four flavonoids, namely luteolin, kaempferol, quercetin, and myricetin, dissolved in aqueous solution have been simulated by exploiting a fully polarizable QM/FQ approach combined with MD simulations, performed by either including or discarding off-site VSs. For all investigated molecules, $MD_{noVS}$ and $MD_{VS}$ sample the configurational space in a similar way, whereas a different description of solute–solvent HB interactions arises. This behavior is not unexpected and it is due to a refined description of HB interactions obtained by including VSs in MD runs.

The QM/FQ spectrum of each flavonoid has been computed on a set of uncorrelated snapshots extracted from both MD trajectories. The observed differences between the various systems have been discussed in light of solute–solvent HB interactions arising from MD runs, showing that they significantly affect computed spectra. In particular, the presence of a larger number of potential HB sites, as in case of **Q** and **M** as compared to **L** and **K**, produces a redshift of the first electronic excitation, which has a $\pi - \pi^*$ nature. Finally, the comparison between computed and experimental spectra shows that $MD_{VS}$ provides the best agreement, probably due to better configurational sampling and HB description.

The agreement with experiments, in particular for luteolin, might be increased by exploiting polarizable force fields (instead of a standard fixed-charges one) in MD simulations, i.e., by performing a so-called polarizable MD simulation [87,88]. In this way, a more physically consistent way of describing the evolution of solute–solvent interactions could be obtained. In addition, off-site charges introduced in $MD_{VS}$ runs might be included in polarizable QM/MM calculations by resorting to polarizable force fields defined in terms of both fluctuating charges and fluctuating dipoles, similarly to what has recently been developed by some of the present authors [58,89,90]. Finally, in this work, the QM–MM coupling has been limited to the account of electrostatic solute–water interactions. The inclusion of non-electrostatic terms, i.e., Pauli repulsion and dispersion, might improve the

agreement between computed and experimental data, in light of similar studies recently reported by some of us [91,92].

**Supplementary Materials:** The following are available online. Figures S1–S3: $\alpha$, $\beta$ and $\gamma$ DDFs for L, K, and M; Figures S4–S6: RDFs between flavonoids' Oxygen atoms and water Hydrogen atoms for L, K, and M; Figure S7: UV/Vis QM/FQ stick spectra computed on the various snapshots extracted from $MD_{VS}$; Figures S8–S10: excitation energies of the first excitation for each flavonoid as a function of $\alpha$, $\beta$, and $\gamma$ dihedral angles.

**Author Contributions:** Conceptualization, C.C.; methodology, S.S., M.A.; software, T.G.; validation, S.S., M.A., and T.G.; formal analysis, S.S.; investigation, S.S.; resources, C.C.; data creation, S.S.; writing—original draft preparation, S.S., M.A.; writing—review and editing, T.G., C.C.; visualization, S.S., T.G.; supervision, M.A., T.G., C.C.; project administration, C.C.; funding acquisition, C.C. All authors have read and agreed to the published version of the manuscript.

**Funding:** This research was funded by the H2020-MSCA-ITN-2017 European Training Network "Computational Spectroscopy in Natural sciences and Engineering" (COSINE), Grant No. 765739, and by the Research Council of Norway through the grant TheoLight (Grant No. 275506).

**Conflicts of Interest:** The authors declare no conflict of interest.

## References

1. Harborne, J.B.; Marby, H.; Marby, T. *The Flavonoids*; Springer: Boston, MA, USA, 1988.
2. Kapešová, J.; Petrásková, L.; Markošová, K.; Rebroš, M.; Kotik, M.; Bojarová, P.; Křen, V. Bioproduction of quercetin and rutinose catalyzed by rutinosidase: novel concept of "solid state biocatalysis". *Int. J. Mol. Sci.* **2019**, *20*, 1112. [CrossRef]
3. Burak, M.; Imen, Y. Flavonoids and their antioxidant properties. *Turkiye Klin. Tip Bil. Derg.* **1999**, *19*, 296–304.
4. Casta eda Ovando, A.; de Lourdes Pacheco-Hernández, M.; Pez-Hern ndez, M.E.; Gal n Vidal, C.A.S. Chemical studies of anthocyanins: A review. *Food Chem.* **2009**, *113*, 859–871. [CrossRef]
5. Lee, Y.K.; Yuk, D.Y.; Lee, J.W.; Lee, S.Y.; Ha, T.Y.; Oh, K.W.; Yun, Y.P.; Hong, J.T. (-)-Epigallocatechin-3-gallate prevents lipopolysaccharide-induced elevation of beta-amyloid generation and memory deficiency. *Brain Res.* **2009**, *1250*, 164–174. [CrossRef] [PubMed]
6. Panche, A.; Diwan, A.; Chandra, S. Flavonoids: An overview. *J. Nutr. Sci.* **2016**, *5*, e47. [CrossRef]
7. Metodiewa, D.; Kochman, A.; Karolczak, S. Evidence for antiradical and antioxidant properties of four biologically active N, N-Diethylaminoethyl ethers of flavaone oximes: A comparison with natural polyphenolic flavonoid rutin action. *IUBMB Life* **1997**, *41*, 1067–1075. [CrossRef]
8. Hayashi, T.; Sawa, K.; Kawasaki, M.; Arisawa, M.; Shimizu, M.; Morita, N. Inhibition of cow's milk xanthine oxidase by flavonoids. *J. Nat. Prod.* **1988**, *51*, 345–348. [CrossRef]
9. Ngwa, W.; Kumar, R.; Thompson, D.; Lyerly, W.; Moore, R.; Reid, T.E.; Lowe, H.; Toyang, N. Potential of Flavonoid-Inspired Phytomedicines against COVID-19. *Molecules* **2020**, *25*, 2707. [CrossRef] [PubMed]
10. Das, P.; Majumder, R.; Mandal, M.; Basak, P. In-Silico approach for identification of effective and stable inhibitors for COVID-19 main protease (Mpro) from flavonoid based phytochemical constituents of Calendula officinalis. *J. Biomol. Struct. Dyn.* **2020**, 1–16. [CrossRef]
11. Solnier, J.; Fladerer, J.P. Flavonoids: A complementary approach to conventional therapy of COVID-19? *Phytochem. Rev.* **2020**, 1–23. [CrossRef]
12. Robak, J.; Gryglewski, R. Bioactivity of flavonoids. *Pol. J. Pharmacol.* **1996**, *48*, 555–564. [PubMed]
13. Rice-Evans, C.; Miller, N. Antioxidant activities of flavonoids as bioactive components of food. *Biochem. Soc. Trans.* **1996**, *24*, 790–795. [CrossRef] [PubMed]
14. Spencer, J.P.; Abd El Mohsen, M.M.; Rice-Evans, C. Cellular uptake and metabolism of flavonoids and their metabolites: Implications for their bioactivity. *Arch. Biochem. Biophys.* **2004**, *423*, 148–161. [CrossRef] [PubMed]
15. Pinent, M.; Castell, A.; Baiges, I.; Montagut, G.; Arola, L.; Ardévol, A. Bioactivity of flavonoids on insulin-secreting cells. *Compr. Rev. Food Sci.* **2008**, *7*, 299–308. [CrossRef]
16. Erlund, I. Review of the flavonoids quercetin, hesperetin, and naringenin. Dietary sources, bioactivities, bioavailability, and epidemiology. *Nutr. Res.* **2004**, *24*, 851–874. [CrossRef]
17. Rohan, T.; Connell, M. The precursors of chocolate aroma: a study of the flavonoids and phenolic acids. *J. Food Sci.* **1964**, *29*, 460–463. [CrossRef]

18. Samanta, A.; Das, G.; Das, S.K. Roles of flavonoids in plants. *Carbon* **2011**, *100*, 12–35.
19. Sadighara, P.; Gharibi, S.; Jafari, A.M.; Khaniki, G.J.; Salari, S. The antioxidant and Flavonoids contents of Althaea officinalis L. flowers based on their color. *Avicenna J. Phytomed.* **2012**, *2*, 113.
20. Yoshida, K.; Oyama, K.; Kondo, T. Chemistry of flavonoids in color development. *Rec. Adv. Polyphen. Res.* **2012**, *3*, 99–129.
21. Kennedy, J.A.; Matthews, M.A.; Waterhouse, A.L. Effect of maturity and vine water status on grape skin and wine flavonoids. *Am. J. Enol. Viticult.* **2002**, *53*, 268–274.
22. Waterhouse, A.L. Wine phenolics. *Ann. N. Y. Acad. Sci.* **2002**, *957*, 21–36. [CrossRef] [PubMed]
23. Lairon, D.; Amiot, M.J. Flavonoids in food and natural antioxidants in wine. *Curr. Opin. Lipidol.* **1999**, *10*, 23–28. [CrossRef] [PubMed]
24. Fernandes, I.; Pérez-Gregorio, R.; Soares, S.; Mateus, N.; De Freitas, V. Wine flavonoids in health and disease prevention. *Molecules* **2017**, *22*, 292. [CrossRef] [PubMed]
25. Miyagi, Y.; Miwa, K.; Inoue, H. Inhibition of human low-density lipoprotein oxidation by flavonoids in red wine and grape juice. *Am. J. Cardiol.* **1997**, *80*, 1627–1631. [CrossRef]
26. Tapas, A.R.; Sakarkar, D.; Kakde, R. Flavonoids as nutraceuticals: A review. *Trop. J. Pharm. Res.* **2008**, *7*, 1089–1099. [CrossRef]
27. Takahashi, A.; Ohnishi, T. The significance of the study about the biological effects of solar ultraviolet radiation using the Exposed Facility on the International Space Station. *Biol. Sci. Space* **2004**, *18*, 255–260. [CrossRef]
28. Biler, M.; Biedermann, D.; Valentová, K.; Křen, V.; Kubala, M. Quercetin and its analogues: Optical and acido–basic properties. *Phys. Chem. Chem. Phys.* **2017**, *19*, 26870–26879. [CrossRef]
29. Duan, Y. Ultraviolet-visible spectrum characterizations of quercetin in aqueous ethanol solution with different pH values. *J. Chem. Pharm. Res.* **2014**, *6*, 236–240.
30. Dall'Acqua, S.; Miolo, G.; Innocenti, G.; Caffieri, S. The photodegradation of quercetin: relation to oxidation. *Molecules* **2012**, *17*, 8898–8907. [CrossRef]
31. Cerrato, A.; De Santis, D.; Moresi, M. Production of luteolin extracts from Reseda luteola and assessment of their dyeing properties. *J. Sci. Food Agric.* **2002**, *82*, 1189–1199. [CrossRef]
32. M Calderon-Montano, J.; Burgos-Morón, E.; Pérez-Guerrero, C.; López-Lázaro, M. A review on the dietary flavonoid kaempferol. *Mini-Rev. Med. Chem.* **2011**, *11*, 298–344. [CrossRef] [PubMed]
33. McDonald, M.S.; Hughes, M.; Burns, J.; Lean, M.E.; Matthews, D.; Crozier, A. Survey of the free and conjugated myricetin and quercetin content of red wines of different geographical origins. *J. Agric. Food Chem.* **1998**, *46*, 368–375. [CrossRef] [PubMed]
34. Fang, F.; Li, J.M.; Pan, Q.H.; Huang, W.D. Determination of red wine flavonoids by HPLC and effect of aging. *Food Chem.* **2007**, *101*, 428–433. [CrossRef]
35. Giovannini, T.; Egidi, F.; Cappelli, C. Molecular spectroscopy of aqueous solutions: A theoretical perspective. *Chem. Soc. Rev.* **2020**, *49*, 5664–5677. [CrossRef] [PubMed]
36. Giovannini, T.; Egidi, F.; Cappelli, C. Theory and algorithms for chiroptical properties and spectroscopies of aqueous systems. *Phys. Chem. Chem. Phys.* **2020**, *22*, 22864–22879. [CrossRef] [PubMed]
37. Loco, D.; Polack, É.; Caprasecca, S.; Lagardere, L.; Lipparini, F.; Piquemal, J.P.; Mennucci, B. A QM/MM approach using the AMOEBA polarizable embedding: from ground state energies to electronic excitations. *J. Chem. Theory Comput.* **2016**, *12*, 3654–3661. [CrossRef]
38. Aidas, K.; Møgelhøj, A.; Nilsson, E.J.; Johnson, M.S.; Mikkelsen, K.V.; Christiansen, O.; Söderhjelm, P.; Kongsted, J. On the performance of quantum chemical methods to predict solvatochromic effects: The case of acrolein in aqueous solution. *J. Chem. Phys.* **2008**, *128*, 194503. [CrossRef]
39. Tomasi, J.; Persico, M. Molecular interactions in solution: an overview of methods based on continuous distributions of the solvent. *Chem. Rev.* **1994**, *94*, 2027–2094. [CrossRef]
40. Tomasi, J.; Mennucci, B.; Cammi, R. Quantum mechanical continuum solvation models. *Chem. Rev.* **2005**, *105*, 2999–3094. [CrossRef]
41. Tomasi, J.; Cammi, R.; Mennucci, B.; Cappelli, C.; Corni, S. Molecular properties in solution described with a continuum solvation model. *Phys. Chem. Chem. Phys.* **2002**, *4*, 5697–5712. [CrossRef]
42. Cappelli, C. Integrated QM/Polarizable MM/Continuum Approaches to Model Chiroptical Properties of Strongly Interacting Solute-Solvent Systems. *Int. J. Quantum Chem.* **2016**, *116*, 1532–1542. [CrossRef]
43. Mennucci, B. Polarizable Continuum Model. *WIREs Comput. Mol. Sci.* **2012**, *2*, 386–404. [CrossRef]

44. Giovannini, T.; Ambrosetti, M.; Cappelli, C. A polarizable embedding approach to second harmonic generation (SHG) of molecular systems in aqueous solutions. *Theor. Chem. Acc.* **2018**, *137*, 74. [CrossRef]
45. Egidi, F.; Russo, R.; Carnimeo, I.; D'Urso, A.; Mancini, G.; Cappelli, C. The Electronic Circular Dichroism of Nicotine in Aqueous Solution: A Test Case for Continuum and Mixed Explicit-Continuum Solvation Approaches. *J. Phys. Chem. A* **2015**, *119*, 5396–5404. [CrossRef] [PubMed]
46. Lipparini, F.; Egidi, F.; Cappelli, C.; Barone, V. The optical rotation of methyloxirane in aqueous solution: A never ending story? *J. Chem. Theory Comput.* **2013**, *9*, 1880–1884. [CrossRef] [PubMed]
47. Cappelli, C.; Mennucci, B.; Monti, S. Environmental effects on the spectroscopic properties of gallic acid: A combined classical and quantum mechanical study. *J. Phys. Chem. A* **2005**, *109*, 1933–1943. [CrossRef]
48. Warshel, A.; Karplus, M. Calculation of ground and excited state potential surfaces of conjugated molecules. I. Formulation and parametrization. *J. Am. Chem. Soc.* **1972**, *94*, 5612–5625. [CrossRef]
49. Warshel, A.; Levitt, M. Theoretical studies of enzymic reactions: dielectric, electrostatic and steric stabilization of the carbonium ion in the reaction of lysozyme. *J. Mol. Biol.* **1976**, *103*, 227–249. [CrossRef]
50. Senn, H.M.; Thiel, W. QM/MM methods for biomolecular systems. *Angew. Chem. Int. Ed.* **2009**, *48*, 1198–1229. [CrossRef]
51. Lin, H.; Truhlar, D.G. QM/MM: What have we learned, where are we, and where do we go from here? *Theor. Chem. Acc.* **2007**, *117*, 185–199. [CrossRef]
52. Curutchet, C.; Muñoz-Losa, A.; Monti, S.; Kongsted, J.; Scholes, G.D.; Mennucci, B. Electronic energy transfer in condensed phase studied by a polarizable QM/MM model. *J. Chem. Theory Comput.* **2009**, *5*, 1838–1848. [CrossRef] [PubMed]
53. Lipparini, F.; Cappelli, C.; Scalmani, G.; De Mitri, N.; Barone, V. Analytical first and second derivatives for a fully polarizable QM/classical hamiltonian. *J. Chem. Theory Comput.* **2012**, *8*, 4270–4278. [CrossRef]
54. Lipparini, F.; Cappelli, C.; Barone, V. Linear response theory and electronic transition energies for a fully polarizable QM/classical hamiltonian. *J. Chem. Theory Comput.* **2012**, *8*, 4153–4165. [CrossRef]
55. Olsen, J.M.H.; Kongsted, J. Molecular properties through polarizable embedding. *Adv. Quantum Chem.* **2011**, *61*, 107–143.
56. Olsen, J.M.H.; Steinmann, C.; Ruud, K.; Kongsted, J. Polarizable density embedding: A new QM/QM/MM-based computational strategy. *J. Phys. Chem. A* **2015**, *119*, 5344–5355. [CrossRef] [PubMed]
57. Boulanger, E.; Thiel, W. Solvent boundary potentials for hybrid QM/MM computations using classical drude oscillators: A fully polarizable model. *J. Chem. Theory Comput.* **2012**, *8*, 4527–4538. [CrossRef]
58. Giovannini, T.; Puglisi, A.; Ambrosetti, M.; Cappelli, C. Polarizable QM/MM approach with fluctuating charges and fluctuating dipoles: The QM/FQFμ model. *J. Chem. Theory Comput.* **2019**, *15*, 2233–2245. [CrossRef]
59. Rick, S.W.; Stuart, S.J.; Berne, B.J. Dynamical fluctuating charge force fields: Application to liquid water. *J. Chem. Phys.* **1994**, *101*, 6141–6156. [CrossRef]
60. Rick, S.W.; Stuart, S.J.; Bader, J.S.; Berne, B. Fluctuating charge force fields for aqueous solutions. *J. Mol. Liq.* **1995**, *65*, 31–40. [CrossRef]
61. Rick, S.W.; Berne, B.J. Dynamical Fluctuating Charge Force Fields: The Aqueous Solvation of Amides. *J. Am. Chem. Soc.* **1996**, *118*, 672–679, [CrossRef]
62. Giovannini, T.; Olszowka, M.; Cappelli, C. Effective Fully Polarizable QM/MM Approach To Model Vibrational Circular Dichroism Spectra of Systems in Aqueous Solution. *J. Chem. Theory Comput.* **2016**, *12*, 5483–5492. [CrossRef]
63. Egidi, F.; Giovannini, T.; Del Frate, G.; Lemler, P.M.; Vaccaro, P.H.; Cappelli, C. A combined experimental and theoretical study of optical rotatory dispersion for (R)-glycidyl methyl ether in aqueous solution. *Phys. Chem. Chem. Phys.* **2019**, *21*, 3644–3655. [CrossRef] [PubMed]
64. Giovannini, T.; Macchiagodena, M.; Ambrosetti, M.; Puglisi, A.; Lafiosca, P.; Lo Gerfo, G.; Egidi, F.; Cappelli, C. Simulating vertical excitation energies of solvated dyes: From continuum to polarizable discrete modeling. *Int. J. Quantum Chem.* **2019**, *119*, e25684. [CrossRef]
65. Macchiagodena, M.; Mancini, G.; Pagliai, M.; Barone, V. Accurate prediction of bulk properties in hydrogen bonded liquids: Amides as case studies. *Phys. Chem. Chem. Phys.* **2016**, *18*, 25342–25354. [CrossRef] [PubMed]
66. Macchiagodena, M.; Mancini, G.; Pagliai, M.; Cardini, G.; Barone, V. New atomistic model of pyrrole with improved liquid state properties and structure. *Int. J. Quantum Chem.* **2017**. [CrossRef]

67. Naseem, B.; Sabri, A.; Hasan, A.; Shah, S.S. Interaction of flavonoids within organized molecular assemblies of anionic surfactant. *Colloids Surfaces B Biointerfaces* **2004**, *35*, 7–13. [CrossRef]
68. Frisch, M.J.; Trucks, G.W.; Schlegel, H.B.; Scuseria, G.E.; Robb, M.A.; Cheeseman, J.R.; Scalmani, G.; Barone, V.; Petersson, G.A.; Nakatsuji, H.; et al. *Gaussian 16 Revision A.03*; Gaussian Inc.: Wallingford, CT, USA, 2016.
69. Abrahama, M.J.; Murtola, T.; Schulz, R.; Pálla, S.; Smith, J.C.; Hess, B.; Lindahl, E. GROMACS: High Performance Molecular Simulations through Multi-Level Parallelism from Laptops to Supercomputers. *SoftwareX* **2015**, *1*, 19–25. [CrossRef]
70. Wang, J.; Wolf, R.M.; Caldwell, J.W.; Kollman, P.A.; Case, D.A. Development and testing of a general amber force field. *J. Comput. Chem.* **2004**, *25*, 1157–1174, [CrossRef]
71. Mark, P.; Nilsson, L. Structure and dynamics of the TIP3P, SPC, and SPC/E water models at 298 K. *J. Phys. Chem. A* **2001**, *105*, 9954–9960. [CrossRef]
72. Bayly, C.I.; Cieplak, P.; Cornell, W.; Kollman, P.A. A well-behaved electrostatic potential based method using charge restraints for deriving atomic charges: The RESP model. *J. Phys. Chem.* **1993**, *97*, 10269–10280, [CrossRef]
73. Darden, T.; York, D.; Pedersen, L. Particle mesh Ewald: An Nlog(N) method for Ewald sums in large systems. *J. Chem. Phys.* **1993**, *98*, 10089–10092. [CrossRef]
74. Boys, S. *Quantum Theory of Atoms, Molecules, and the Solid State*; Academic Press: New York, NY, USA, 1966; p. 253.
75. Bussi, G.; Donadio, D.; Parrinello, M. Canonical sampling through velocity rescaling. *J. Chem. Phys.* **2007**, *126*, 014101. [CrossRef] [PubMed]
76. Brehm, M.; Kirchner, B. TRAVIS-A Free Analyzer and Visualizer for Monte Carlo and Molecular Dynamics Trajectories. *J. Chem. Inf. Model.* **2011**, *51*, 2007–2023, [CrossRef] [PubMed]
77. Puglisi, A.; Giovannini, T.; Antonov, L.; Cappelli, C. Interplay between conformational and solvent effects in UV-visible absorption spectra: Curcumin tautomers as a case study. *Phys. Chem. Chem. Phys.* **2019**, *21*, 15504–15514. [CrossRef] [PubMed]
78. Gómez, S.; Giovannini, T.; Cappelli, C. Absorption spectra of xanthines in aqueous solution: A computational study. *Phys. Chem. Chem. Phys.* **2020**, *22*, 5929–5941. [CrossRef] [PubMed]
79. Di Remigio, R.; Giovannini, T.; Ambrosetti, M.; Cappelli, C.; Frediani, L. Fully polarizable QM/fluctuating charge approach to two-photon absorption of aqueous solutions. *J. Chem. Theory Comput.* **2019**, *15*, 4056–4068. [CrossRef] [PubMed]
80. Reichardt, C. Solvatochromism, thermochromism, piezochromism, halochromism, and chiro-solvatochromism of pyridinium N-phenoxide betaine dyes. *Chem. Soc. Rev.* **1992**, *21*, 147–153. [CrossRef]
81. Reichardt, C. Solvatochromic dyes as solvent polarity indicators. *Chem. Rev.* **1994**, *94*, 2319–2358. [CrossRef]
82. Marenich, A.V.; Cramer, C.J.; Truhlar, D.G.; Guido, C.A.; Mennucci, B.; Scalmani, G.; Frisch, M.J. Practical computation of electronic excitation in solution: Vertical excitation model. *Chem. Sci.* **2011**, *2*, 2143–2161. [CrossRef]
83. Duchemin, I.; Guido, C.A.; Jacquemin, D.; Blase, X. The Bethe–Salpeter formalism with polarisable continuum embedding: Reconciling linear-response and state-specific features. *Chem. Sci.* **2018**, *9*, 4430–4443. [CrossRef]
84. Biczysko, M.; Bloino, J.; Brancato, G.; Cacelli, I.; Cappelli, C.; Ferretti, A.; Lami, A.; Monti, S.; Pedone, A.; Prampolini, G.; et al. Integrated computational approaches for spectroscopic studies of molecular systems in the gas phase and in solution: pyrimidine as a test case. *Theor. Chem. Acc.* **2012**, *131*, 1201. [CrossRef]
85. Hodecker, M.; Biczysko, M.; Dreuw, A.; Barone, V. Simulation of Vacuum UV Absorption and Electronic Circular Dichroism Spectra of Methyl Oxirane: The Role of Vibrational Effects. *J. Chem. Theory Comput.* **2016**, *12*, 2820–2833. [CrossRef] [PubMed]
86. Improta, R.; Santoro, F.; Barone, V.; Lami, A. Vibronic model for the quantum dynamical study of the competition between bright and charge-transfer excited states in single-strand polynucleotides: The adenine dimer case. *J. Phys. Chem. A* **2009**, *113*, 15346–15354. [CrossRef] [PubMed]
87. Lamoureux, G.; Harder, E.; Vorobyov, I.V.; Roux, B.; MacKerell, A.D., Jr. A polarizable model of water for molecular dynamics simulations of biomolecules. *Chem. Phys. Lett.* **2006**, *418*, 245–249. [CrossRef]
88. Wu, J.C.; Piquemal, J.P.; Chaudret, R.; Reinhardt, P.; Ren, P. Polarizable molecular dynamics simulation of Zn (II) in water using the AMOEBA force field. *J. Chem. Theory Comput.* **2010**, *6*, 2059–2070. [CrossRef]

89. Giovannini, T.; Riso, R.R.; Ambrosetti, M.; Puglisi, A.; Cappelli, C. Electronic transitions for a fully polarizable qm/mm approach based on fluctuating charges and fluctuating dipoles: Linear and corrected linear response regimes. *J. Chem. Phys.* **2019**, *151*, 174104. [CrossRef]
90. Giovannini, T.; Grazioli, L.; Ambrosetti, M.; Cappelli, C. Calculation of ir spectra with a fully polarizable qm/mm approach based on fluctuating charges and fluctuating dipoles. *J. Chem. Theory Comput.* **2019**, *15*, 5495–5507. [CrossRef]
91. Giovannini, T.; Lafiosca, P.; Cappelli, C. A General Route to Include Pauli Repulsion and Quantum Dispersion Effects in QM/MM Approaches. *J. Chem. Theory Comput.* **2017**, *13*, 4854–4870. [CrossRef]
92. Giovannini, T.; Ambrosetti, M.; Cappelli, C. Quantum Confinement Effects on Solvatochromic Shifts of Molecular Solutes. *J. Phys. Chem. Lett.* **2019**, *10*, 5823–5829. [CrossRef]

# Supplementary Materials for: Simulating Absorption Spectra of Flavonoids in Aqueous Solution: a Polarizable QM/MM Study

Sulejman Skoko,[†] Matteo Ambrosetti,[†] Tommaso Giovannini,[‡] and Chiara Cappelli[*,†]

†*Scuola Normale Superiore, Piazza dei Cavalieri 7, 56126 Pisa, Italy.*

‡*Department of Chemistry, Norwegian University of Science and Technology, 7491 Trondheim, Norway*

E-mail: chiara.cappelli@sns.it

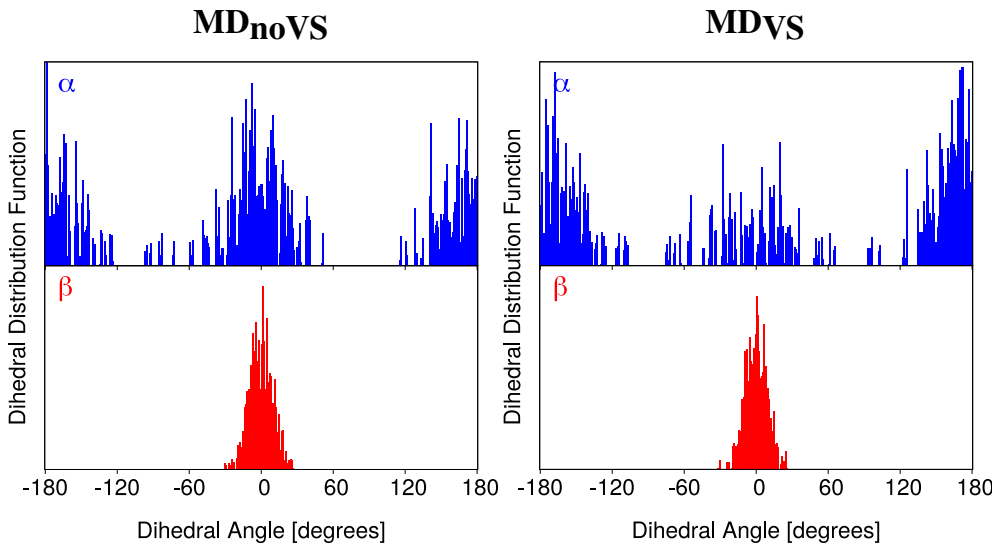


Figure S1: Dihedral distribution functions of $\alpha$ (top,blue), $\beta$ (bottom,red) dihedral angles of Luteolin (**L**) as obtained from $MD_{noVS}$ (left) and $MD_{VS}$ (right).

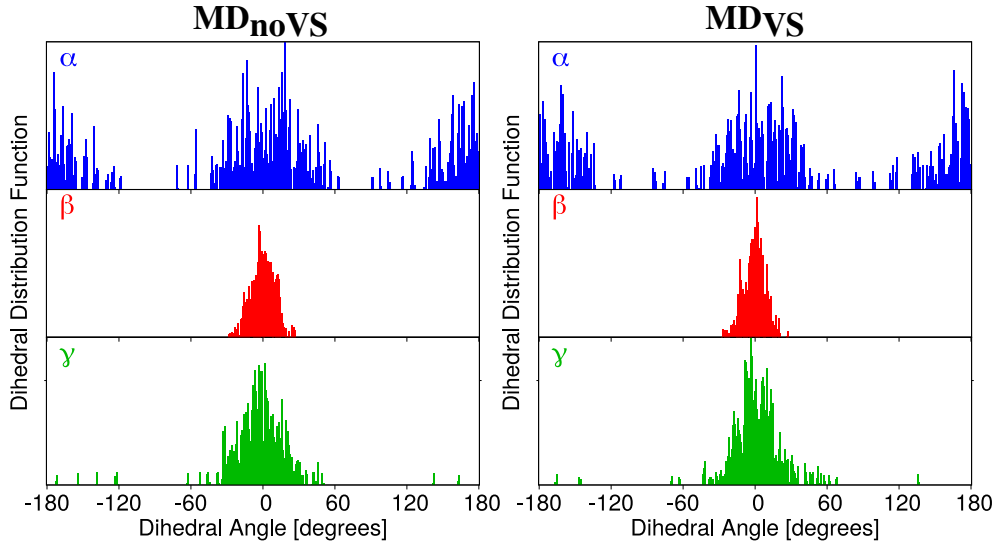


Figure S2: Dihedral distribution functions of $\alpha$ (top,blue), $\beta$ (middle,red) and $\gamma$ (bottom,green) dihedral angles of Kaempferol (**K**) as obtained from $MD_{noVS}$ (left) and $MD_{VS}$ (right).

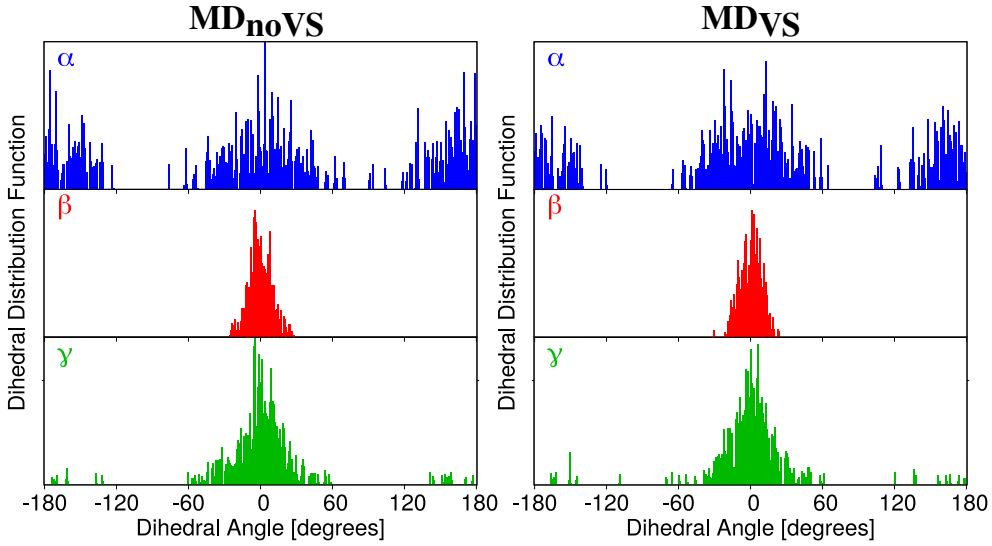


Figure S3: Dihedral distribution functions of $\alpha$ (top,blue), $\beta$ (middle,red) and $\gamma$ (bottom,green) dihedral angles of Quercetin (**Q**) as obtained from $MD_{noVS}$ (left) and $MD_{VS}$ (right).

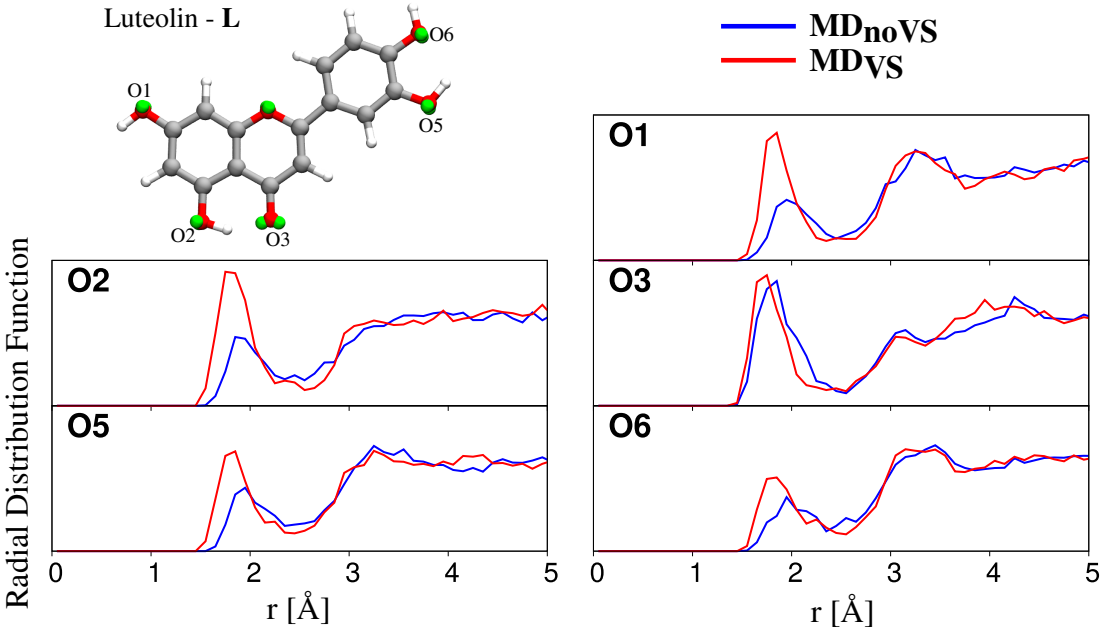


Figure S4: Radial distribution functions between selected Oxygen atoms of Luteolin and water Hydrogen atoms as obtained from $MD_{noVS}$ (blue) and $MD_{VS}$ (red).

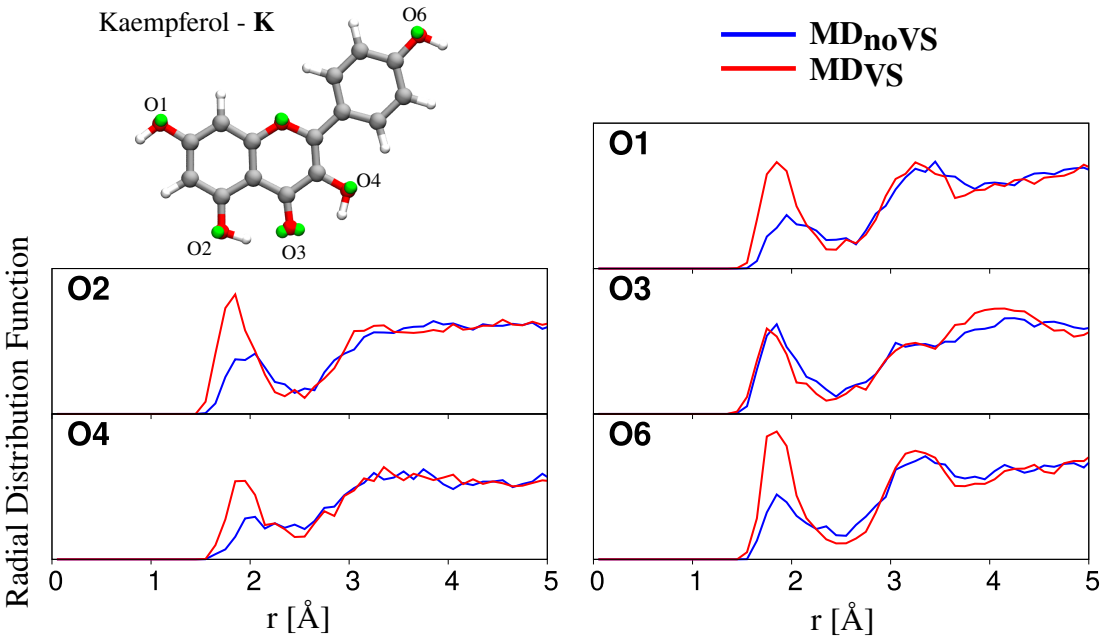


Figure S5: Radial distribution functions between selected Oxygen atoms of Kaempferol and water Hydrogen atoms as obtained from $MD_{noVS}$ (blue) and $MD_{VS}$ (red).

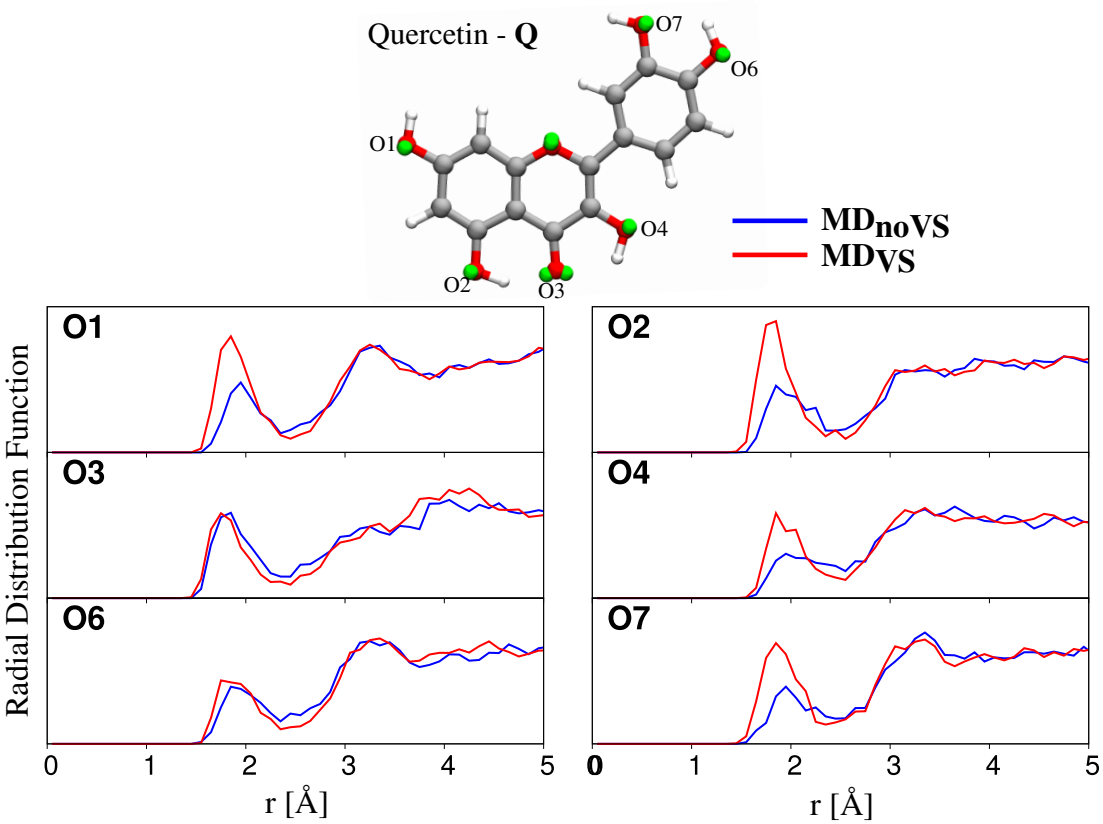


Figure S6: Radial distribution functions between selected Oxygen atoms of Quercetin and water Hydrogen atoms as obtained from $MD_{noVS}$ (blue) and $MD_{VS}$ (red).

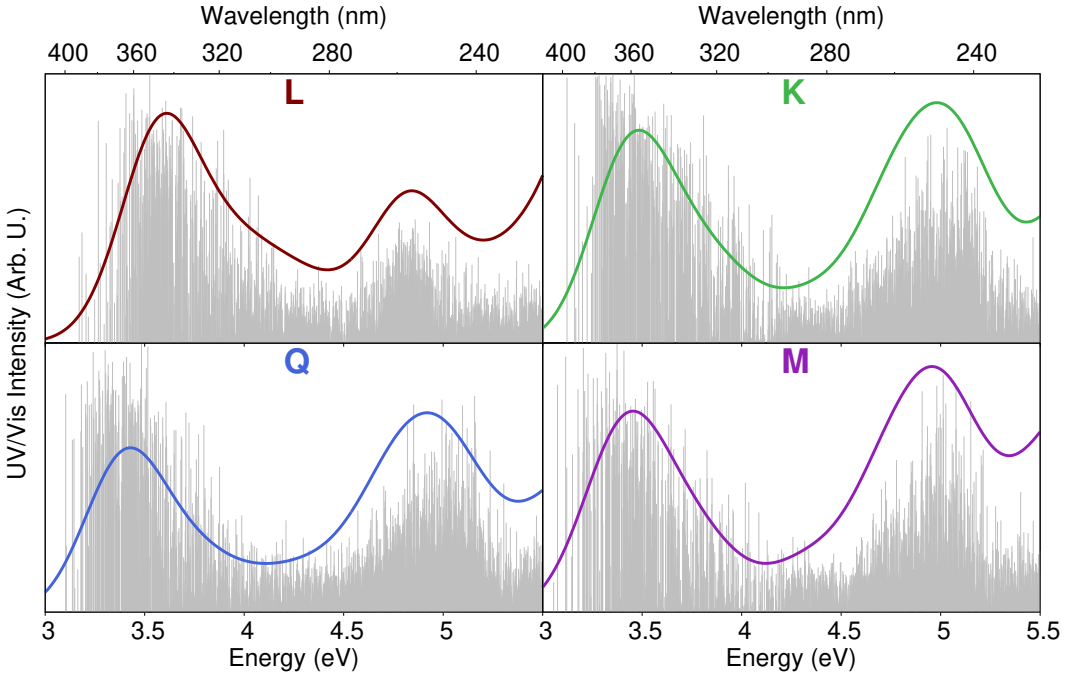


Figure S7: QM/FQ UV/Vis stick spectra computed on the snapshots extracted from $MD_{VS}$. The convoluted QM/FQ spectra are also plotted.

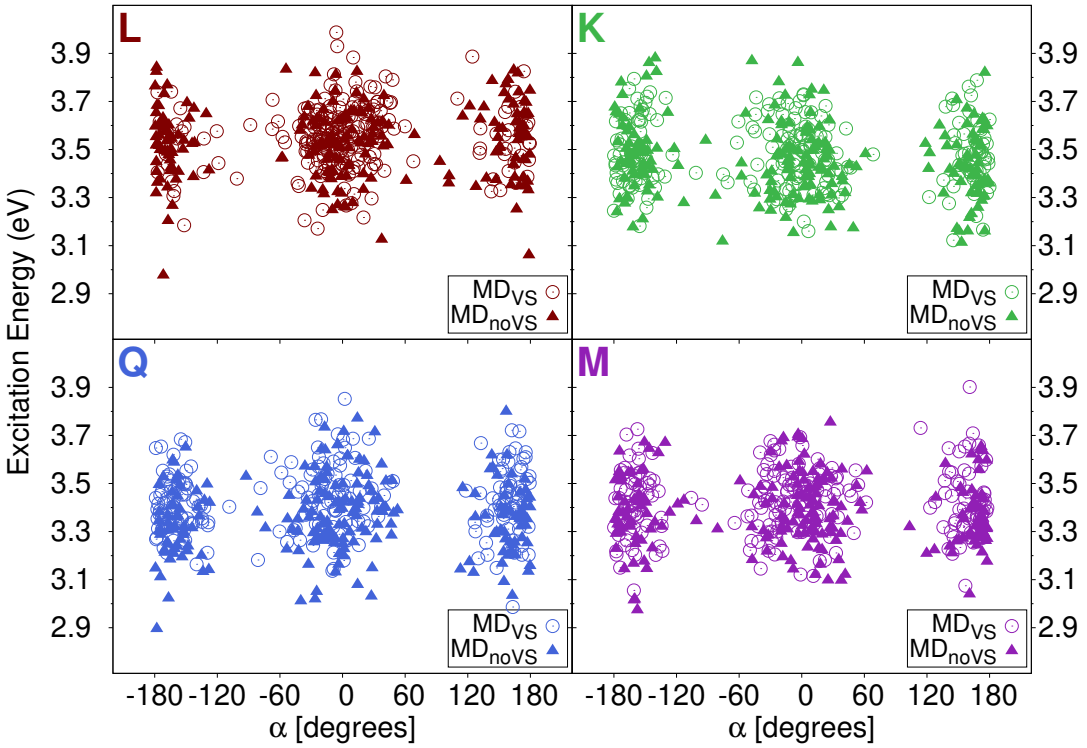


Figure S8: QM/FQ Excitation Energies of the first electronic transition as a function of $\alpha$ dihedral angle.

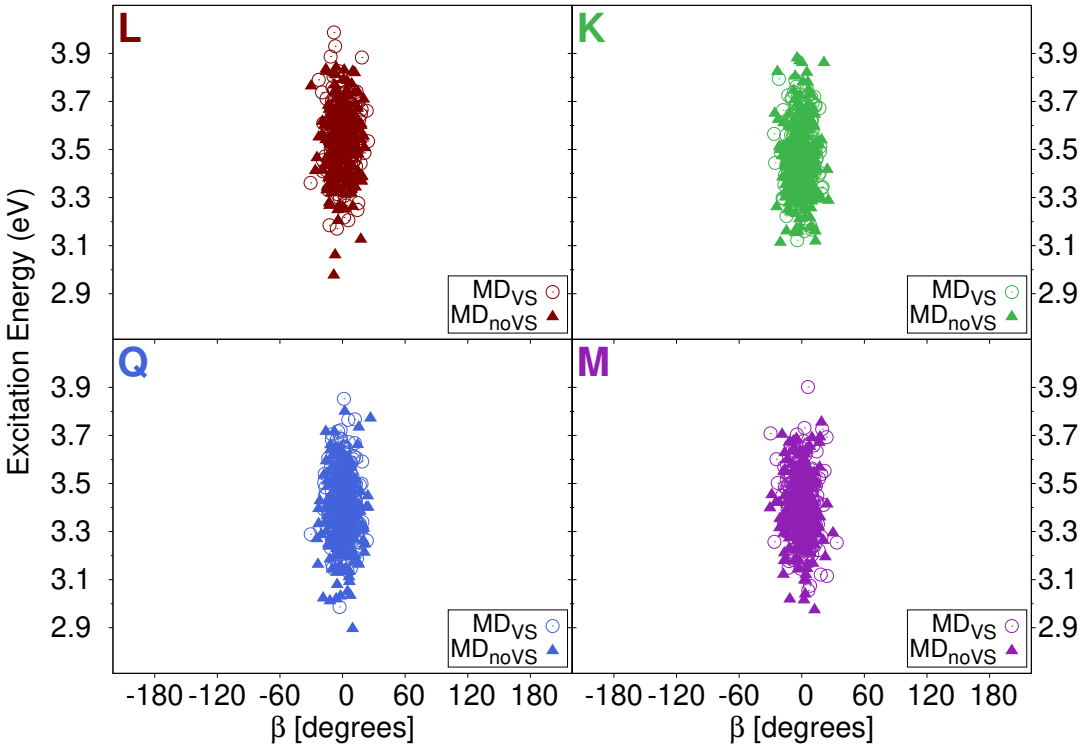


Figure S9: QM/FQ Excitation Energies of the first electronic transition as a function of $\beta$ dihedral angle.

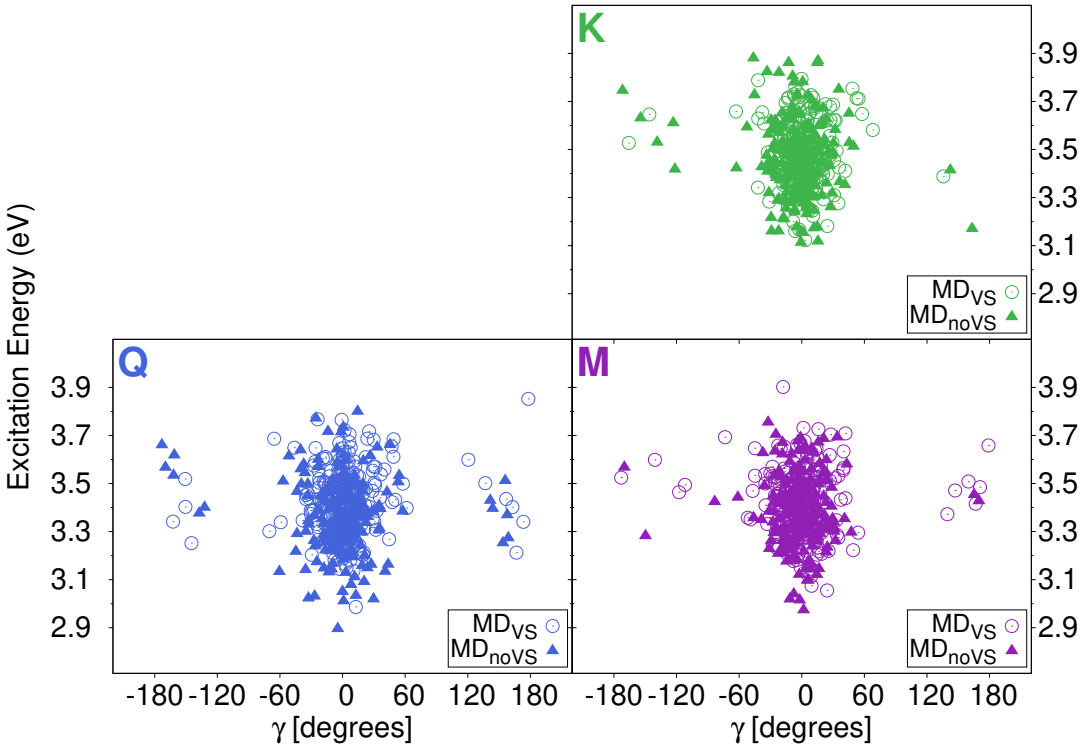


Figure S10: QM/FQ Excitation Energies of the first electronic transition as a function of $\gamma$ dihedral angle.

# CHAPTER 4

# Quantum Mechanics/Fluctuating Charge Protocol to Compute Solvatochromic Shifts

JCTC Journal of Chemical Theory and Computation

pubs.acs.org/JCTC

Article

# Quantum Mechanics/Fluctuating Charge Protocol to Compute Solvatochromic Shifts

Matteo Ambrosetti, Sulejman Skoko, Tommaso Giovannini,* and Chiara Cappelli*

Cite This: *J. Chem. Theory Comput.* 2021, 17, 7146–7156

Read Online

ACCESS | Metrics & More | Article Recommendations | Supporting Information

**ABSTRACT:** Despite the potentialities of the quantum mechanics (QM)/fluctuating charge (FQ) approach to model the spectral properties of solvated systems, its extensive use has been hampered by the lack of reliable parametrizations of solvents other than water. In this paper, we substantially extend the applicability of QM/FQ to solvating environments of different polarities and hydrogen-bonding capabilities. The reliability and robustness of the approach are demonstrated by challenging the model to simulate solvatochromic shifts of four organic chromophores, which display large shifts when dissolved in apolar, aprotic or polar, protic solvents.

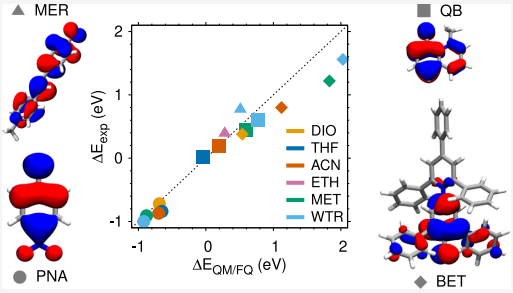




## 1. INTRODUCTION

The study of electronic and optical properties of chromophores is of particular interest for many different applications, ranging from photochemistry to technology.[1] In most cases, such optical properties are tuned by dissolving the selected dye in different solvents, which can yield to substantial changes in the solute's properties.[2] When dealing with electronic excitations, solvent effects mainly manifest in a shift of the solute's absorption band,[3] which is usually referred to as solvatochromism, or a solvatochromic shift.[2,4−10] Depending on the nature of the transition, blue or red shifts are observed;[2] therefore, reliable computational approaches are needed to correctly reproduce both the "sign" of the solvatochromic shift and its magnitude as a function of the nature of the solvent.[9]

To this end, different methods have been proposed, generally focusing the attention on the solute, which is responsible for the spectral signal and is accurately described at the quantum-mechanics (QM) level. The solvent, which modifies but does not determine the spectral properties, is instead treated at a lower level of sophistication.[11,12] Various approaches differ in the way they describe the solvent, which can be treated implicitly, as a continuum, or atomistically.[12,13] In the latter case, QM/molecular mechanics (MM)[14,15] or quantum embedding approaches[16,17] may be used, where solvent molecules are described by a classical force field or a QM wavefunction, respectively. Another remarkable difference between the three aforementioned approaches is the way they model solute−solvent interactions. Continuum solvation is a "mean-field" approach, where specific, directional interactions (e.g., hydrogen bonding) are neglected.[11] The latter are instead considered in explicit, atomistic approaches, which are specified by the quality of the description of solvent molecules and their interaction with the QM solute.[14,18−21] In most quantum embedding methods, electrostatic, polarization, and Pauli repulsion solute−solvent interactions are accurately treated,[19,22] whereas QM/MM approaches generally discard quantum repulsion,[23,24] and sometimes also polarization effects.[25] However, the computational cost of QM/MM methods being much lower than those of most quantum embedding methods, the former are rapidly becoming the golden standard for many applications,[18,25,26] especially those refined approaches, which are able to correctly take into account solute−solvent mutual polarization effects (i.e., in the so-called polarizable QM/MM embedding methods).[3,18,26−29]

Polarizable QM/MM embedding approaches can be based on distributed multipoles,[30] induced dipoles,[3,25,27,29] Drude oscillators,[31,32] fluctuating charges (FQ),[33,34] and possibly dipoles,[35−37] or Amoeba.[38−40] In particular, the QM/FQ approach has been specifically developed to model spectral properties.[18] There, MM atoms are endowed with a charge that can vary as a function of differences in MM electronegativity or as a response to the electric potential generated by the QM density.[33]

Despite the excellent performance of QM/FQ to describe aqueous solutions, mainly due to a reliable parametrization of the force field and the extension up to analytical energy third derivatives,[41−47] its application to non-aqueous solutions has

Received: July 30, 2021
Published: October 7, 2021

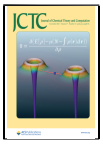





https://doi.org/10.1021/acs.jctc.1c00763
*J. Chem. Theory Comput.* 2021, 17, 7146−7156

been severely hampered by the lack of reliable parametrizations. In fact, QM/FQ is a completely general approach, which can be applied to any embedded system, pending a reliable parametrization of the classical layer.[18] In this work, we extend for the first time the FQ force field to six solvents of different polarities and hydrogen-bonding capabilities, thus substantially increasing the applicability of QM/FQ beyond aqueous systems. The method is tested to reproduce solvatochromic shifts of four chromophores, which exhibit large solvatochromic shifts when dissolved in polar, protic and apolar, aprotic solvents, namely, *para*-nitroaniline (PNA), 1-methyl-8-oxyquinolinium betaine (QB), 1-methyl-4-[(oxocyclohexadienylidene)ethylidene]-1,4-dihydropyridine (MER), and 2,6-diphenyl-4-(2,4,6-triphenylpyridin-1-ium-1-yl)phenolate (BET). The molecular structures of the dyes are shown in Figure 1.

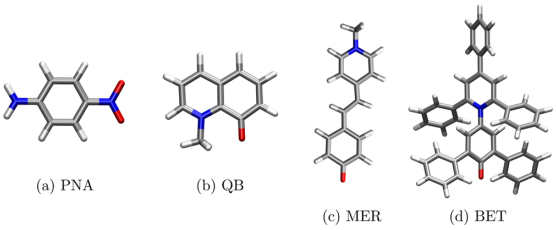


**Figure 1.** Molecular structures of the studied dyes.

The paper is organized as follows. The next section reports on the computational methods, which have been used to parametrize the FQ force field for six selected solvents. The novel FQ parameters are then exploited to predict solvatochromic shifts of the four chromophores in the selected solvents. A summary and a discussion on the future perspectives of the method end the paper.

## 2. METHODS

In QM/FQ, each solvent atom is endowed with a FQ, whose value can vary as a response to the QM electronic density. FQs are defined by solving a linear equation, which is written in terms of atomic electronegativities ($\chi$) and chemical hardnesses ($\eta$), which constitute the parameters of the FQ force field. In this paper, we propose a novel parametrization for 1,4-dioxane (DIO), tetrahydrofuran (THF), acetonitrile (ACN), ethanol (ETH), methanol (MET), and water (WTR), see Figure 2, where also polarity ($\phi$) and dielectric constant ($\epsilon$) of each solvent values are reported. Notice that $\phi$ is equivalent to the normalized $E_N^T$ value usually exploited in Reichardt's scale.[9]

**2.1. Parameterization Procedure.** As already mentioned above, the application of QM/FQ to different environments needs appropriate specification of atomic electronegativities and chemical hardnesses.[48−50] In this work, we have decided to exploit atomic parameters independently of chemical makeups. For instance, in MET, the two hydrogen atoms in C−H and O−H groups are characterized by the same atomic parameters. Notice, however, that our procedure is general and specific atom types, defined similar to other force fields, can also be considered. The parameterization workflow is sketched in Figure 3.

*2.1.1. Reference Dataset.* The first step of the parametrization procedure involves the definition of a reliable

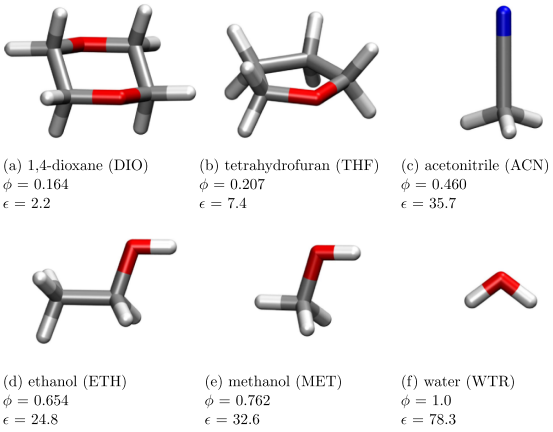


**Figure 2.** Geometries of the solvents studied in the present work ordered based on their polarity. Relative polarity ($\phi$) as reported in ref 2 and the dielectric constant ($\epsilon$) used in QM/PCM calculations are also given.

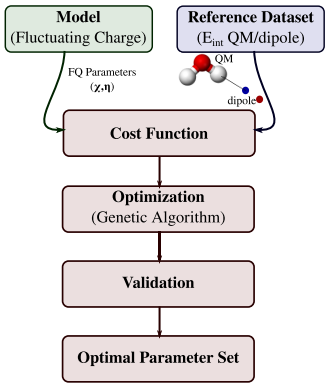


**Figure 3.** Graphical representation of the parameterization workflow.

reference data set, which we built for the following four solvents of increasing polarity:[2] DIO, ACN, MET, and WTR. Notice that, although the parameterization procedure is solvent specific, the final parameters can be transferred to similar solvents, that is, those that are constituted of similar geometrical structures or have similar physicochemical properties. This is indeed the case of THF and ETH, for which the parameters were specified by transferring those obtained for DIO and MET, respectively (vide infra). The reference data set was assembled by using solvent geometries optimized at the CCSD/aug-cc-pVTZ level of theory.

For all structures in the data set, the interaction energy ($E_{int}^{REF}$) between each solvent molecule (treated at the QM level) and a dipolar probe was calculated. All QM/dipole reference calculations were performed at the Hartree−Fock/6-311++G** level, by using the electronic structure program e$^{\mathcal{T}}$.[51] In particular, we followed the strategy first proposed by Stern et al.[52] and recently exploited in ref 53. In this approach, the dipolar probe is constituted by a pair of ±1 a.u. point charges separated by 1 Å. The solvent−dipole interaction energy is then sampled along different symmetry axes and solvent−dipole distances. Depending on the solvent, a



https://doi.org/10.1021/acs.jctc.1c00763
J. Chem. Theory Comput. 2021, 17, 7146−7156

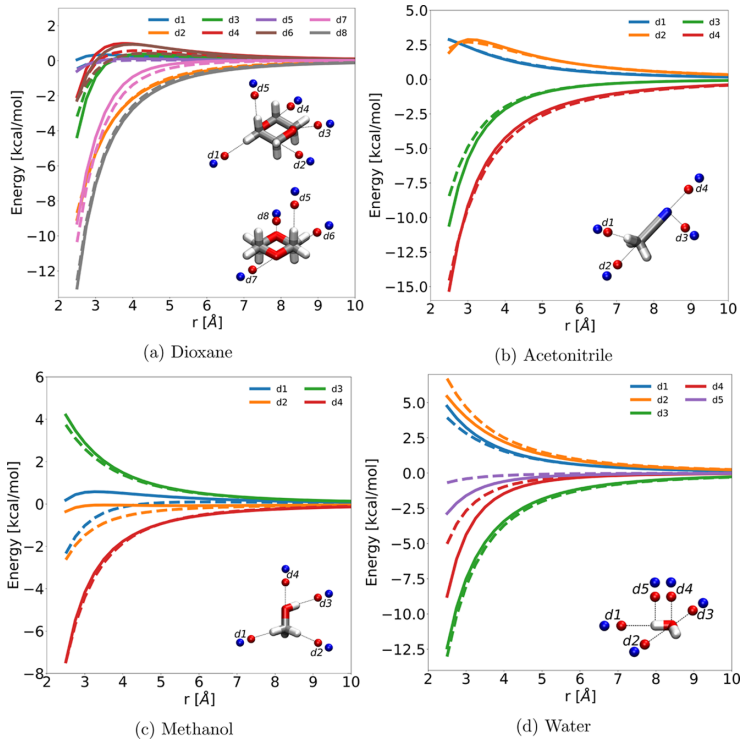


**Figure 4.** Reference QM/dipole (solid lines) and FQ/dipole (dashed lines) interaction energies (in kcal/mol) as a function of the solvent−dipole distance for all the parametrized solvents (DIO, ACN, MET, and WTR).

different number of points, ranging between 150 and 250, were exploited. The minimum/maximum distance between the probe and the solvent molecule is 2.5/10.0 Å, with a constant step of 0.25 Å. The results of the calculations for the reference data set obtained for the four solvents are plotted as a solid line in Figure 4.

*2.1.2. Cost Function.* The loss function ($\xi^2$) used to train the model was defined as

$$\xi^2 = \frac{1}{N}\sum_{i=1}^{N} w_i (E_{\mathrm{int},i}^{\mathrm{REF}} - E_{\mathrm{int},i}^{\mathrm{FQ}}(\chi, \eta))^2 \quad (1)$$

It is a weighted mean squared error loss function, where $N$ represents the number of points used in the fitting, that is, the solvent−dipole scan configurations obtained at the previous step. $E_{\mathrm{int},i}^{\mathrm{REF}}$ is the QM/dipole reference interaction energy of the $i$-th geometry. On the same geometry, the FQ−dipole interaction energy ($E_{\mathrm{int},i}^{\mathrm{FQ}}(\chi,\eta)$) is computed by treating the solvent molecule at the FQ level. The FQ energy depends on $\chi$ and $\eta$, which are the adjustable parameters of the optimization. In eq 1, $w_i$ is a weighting factor, which was set to the inverse of the solvent−dipole distance.

*2.1.3. Optimization.* FQ parametrization is a non-convex optimization problem, because the two parameter sets $\chi$ and $\eta$ are not linearly related to the interaction energy $E_{\mathrm{int},i}^{\mathrm{FQ}}(\chi,\eta)$. As a consequence, the function is characterized by several local minima, thus a gradient-based algorithm (e.g., steepest descent, conjugate gradient method) would not be effective. For this reason, we exploited a genetic algorithm (GA), which is an evolutionary algorithm that mimics the process of natural selection.[54,55] In particular, we used the Python module inspyred,[56,57] where the parameter space ($\{\chi, \eta\}$) was restrained to the [0,1] interval.

For each solvent molecule, a minimum of 20 parameter optimizations were performed, each constituted by a population of 100 individuals, corresponding to a randomly generated parameter set ($\chi$, $\eta$). Therefore, for each molecule, 2000 different starting points in the parameter space were considered.

*2.1.4. Validation.* GA is a stochastic optimization technique. At the end of the previous step, multiple sets of suboptimal parameters, that is, characterized by similar values of the loss function $\xi^2$, were obtained. In order to select the best parameter set, we performed an additional validation step, which is based on two physical observations.

First, the parameter sets have to follow the electronegativity scale, that is, atomic electronegativity needs to increase as moving right along a row of the periodic table. Therefore, all suboptimal parameter sets that do not follow this criterion were rejected.

Second, we imposed the parameter sets to correctly reproduce the molecular static isotropic polarizability $\alpha_{\mathrm{mol}}$, computed at the CCSD/aug-cc-pVTZ level, and the static isotropic bulk polarizability $\alpha_{\mathrm{bulk}}$, computed at the CAM-B3LYP/6-311++G** level, of the selected solvent. Note in fact that in the FQ formalism, $\eta$ and $\alpha$ are strictly related.[58]

Note that, although the aforementioned validation criteria could have been included in the loss function, we preferred to keep the loss function independent of model specific features. It is worth remarking that the procedure may provide different



https://doi.org/10.1021/acs.jctc.1c00763
J. Chem. Theory Comput. 2021, 17, 7146−7156

optimal parameter sets, also in case the constraints mentioned above are incorporated in the loss function.

*2.1.5. Optimal Parameter Set.* The optimal parameter set, that is, that associated with the lowest value of the loss function and the lowest error for both $\alpha_{mol}$ and $\alpha_{bulk}$, was selected. The values obtained for each solvent molecule are reported in Table S1 given in the Supporting Information.

In Figure 4, FQ solvent−dipole interaction energies as a function of the solvent−dipole distance are reported. Reference QM/dipole values are also plotted for the sake of comparison. The FQ optimal parameter sets correctly reproduce reference curves, although with some discrepancies, essentially due to the lack of out-of-plane polarization in the FQ model (see, for instance, $d_4$ and $d_5$ in Figure 4d). This limitation of FQ may be overcome by adding terms depending on atomic dipoles, as it has been recently shown by some of us.[35] Finally notice that our procedure permits to select the best parameters to reproduce the most relevant interactions of a specific solvent (see for instance $d_3-d_4$ vs $d_1-d_2$ in Figure 4c).

**2.2. Computational Protocol.** In order to compute the QM/FQ UV−vis absorption spectra of the selected dyes in the aforementioned solvents, dynamical aspects of the solvation phenomenon were considered by resorting to classical MD simulations. PNA, QB, and MER geometries were optimized at the CAM-B3LYP/aug-cc-pVDZ level, whereas we adopted the CAM-B3LYP/6-31+G(d,p) level for BET, according to ref 38. Solvent effects on molecular geometries were modeled by using the PCM.[11] All MD runs were performed by using GROMACS.[59] The general AMBER force field (GAFF) was exploited to describe both intramolecular and intermolecular interactions.[60,61] Solute- and solvent-bonded and non-bonded parameters were generated by means of the Antechamber package[62,63] with the only exception of WTR for which the standard TIP3P force field was used.[64] Atomic charges of both the solute and solvent molecules were calculated by using the RESP charge-fitting method.[65] During each MD run, solutes were constrained in their minimum energy structure.

The size of the simulation boxes ranged from 7 nm (PNA) to approximately 10 nm (BET). An integration time step of 1 fs was adopted for all MD runs. The temperature was kept constant to 300 K by adopting the velocity-rescaling method[66] with a coupling constant of 0.1 ps. Electrostatic interactions were taken into account by means of the particle mesh Ewald method[67] using a cut-off radius of 1.4 nm in real space. The same cutoff was also used for van der Waals interactions.

An NPT simulation of 1 ns (using the Berendsen barostat[68] and a coupling constant of 2.0 ps) was performed on each system for equilibration purposes. Then, a 2.5 ns *NVT* production run was performed in order to sample the system's configuration space. A total of 100 uncorrelated snapshots were extracted from the last 2 ns of the MD (one snapshot every 20 ps). For each snapshot, a sphere of variable radius (20−25 Å), depending on the solute size, centered at the solute center of mass, was cut and used in the following QM/FQ UV−vis calculations.

QM/PCM and QM/FQ vertical excitation energies were calculated at the TD-DFT level by exploiting the linear response (LR) and corrected LR (cLR) regimes, which is a first-order state-specific approximation.[36,46] For all the transitions, both LR and cLR shifts with respect to the frozen density approximation ($\omega_0$) were summed, in agreement to refs 69 and 70. Such an approach has been recently proposed in the literature and named cLR$^2$.[71] All QM/PCM and QM/FQ $\omega_0$, LR, cLR, and cLR$^2$ energies are reported in Tables S2 and S3 in the Supporting Information. All TD-DFT calculations were performed by using the CAM-B3LYP functional in combination with the aug-cc-pVDZ as basis set (PNA, QB, and MER) or 6-31+G(d,p) (BET), the latter according to ref 38. All QM/FQ calculations were performed by using a locally modified version of the Gaussian 16 package.[72] Non-polarizable QM/electrostatic embedding (QM/EE) was also performed by exploiting TIP3P and GAFF charges, for WTR and the other solvents, respectively (see Table S4 in the Supporting Information for QM/EE vertical excitation energies).

## 3. NUMERICAL RESULTS

In this section, we apply the parameters obtained above to describe the absorption spectra and solvatochromic shifts of the dyes in Figure 1. For each molecule, we analyze the transition involved in the spectral signal, and we compare the QM/FQ values with EE (QM/EE) and continuum solvation approaches (QM/PCM), so as to disentangle the role of explicit solute−solvent interactions (when relevant) and polarization effects. Finally, the computed data are compared with the experimental values (see Tables S5 in the Supporting Information) and the general trends are commented.

**3.1. *para*-Nitroaniline.** PNA belongs to the family of "push−pull" organic compounds, being characterized by an electron-donor amino group ($NH_2$) and a para electron-acceptor nitro group ($NO_2$), which are connected by a $\pi$-conjugated phenyl ring (see Figure 1a). Different theoretical approaches (continuum and atomistic) have already been challenged to reproduce PNA solvatochromic shifts, by also exploiting correlated wavefunctions.[73−75] The absorption spectrum of PNA is characterized by a bright band, which is due to a charge transfer (CT) transition from the donor to the acceptor moieties.[73−80] Similar to most CT transitions, the PNA absorption maximum exhibits a large red solvatochromic shift as the polarity of the solvent increases. Therefore, PNA represents an ideal candidate to test the quality of the FQ parametrization discussed above. Here, we discuss the PNA absorption spectra in DIO, THF, ACN, MET, and WTR. For all methods (QM/FQ, QM/EE, and QM/PCM), the lowest bright excitation is predicted to be the highest occupied molecular orbital (HOMO)−lowest unoccupied molecular orbital (LUMO) $\pi \rightarrow \pi^*$ transition, with a clear CT character (see Figure 5a).

In Figure 5b, QM/FQ, QM/EE, and QM/PCM excitation energies are compared as a function of the solvent polarity ($\phi$). We first notice that, as expected, QM/PCM absorption energies remain almost constant when $\phi$ is larger than 0.4. This is not surprising, due to the well-known asymptotic behavior of PCM contributions for solvents' permittivity constants larger than 20.[11] Similar results are given by QM/EE, whereas QM/FQ excitation energies decrease when $\phi$ increases, thus matching the experimental trends (see 5).[76,79] For THF and DIO, the experimental trend is generally better reproduced by QM/PCM as compared to QM/FQ. This may be due to inaccurate calculation of the QM/FQ excitation energy of PNA dissolved in THF, because for THF the same FQ atomic parameters obtained for DIO are used (see above).

In Figure 5c, QM/FQ, QM/EE, and QM/PCM solvatochromic shifts ($\Delta E$) computed as



https://doi.org/10.1021/acs.jctc.1c00763
J. Chem. Theory Comput. 2021, 17, 7146−7156

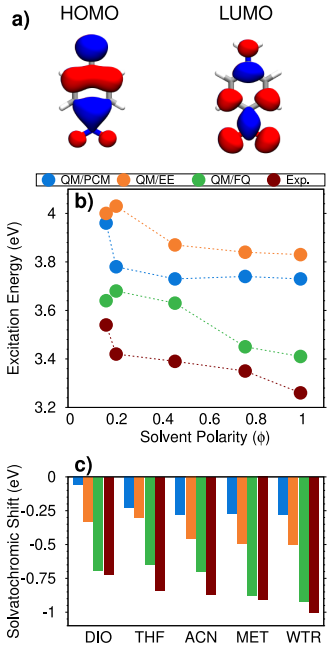


**Figure 5.** (a) PNA HOMO and LUMO involved in the studied electronic transition. (b) QM/PCM, QM/EE, QM/FQ, and experimental PNA excitation energies as a function of the solvent polarity ($\phi$). (c) QM/PCM, QM/EE, QM/FQ, and experimental PNA solvatochromic shifts computed with respect to gas-phase excitation energy.

$$\Delta E = E^{solv} - E^{vac} \tag{2}$$

are compared with the experimental values. Notice that eq 2 refers to vacuo-to-solvent solvatochromic shifts, defined according to ref 38. In eq 2, $E^{vac}$ and $E^{solv}$ are excitation energies in vacuo and in solution, respectively. Figure 5c clearly shows that both QM/PCM and QM/EE strongly underestimate experimentally measured shifts, whereas QM/FQ gives very good values, in some cases in perfect agreement with experiments. In more detail, QM/FQ gives errors for VAC → DIO, VAC → THF, VAC → ACN, VAC → MET, and VAC → WTR shifts of 0.03, 0.19, 0.17, 0.03, and 0.08 eV, respectively, thus confirming the reliability of both the method and its parametrization for the different solvating environments. As expected, the largest error occurs for VAC → THF, because, as already commented, for THF the same parameters as DIO are exploited.

It is worth noticing that our simulations disregard solute−solvent Pauli repulsion, dispersion effects, dynamical changes in solute configurations, and vibronic effects; therefore, a perfect agreement with experimental values is not expected.[81,82] However, the exploited computational protocol permits us to disentangle electrostatic/polarization effects on the solute response. The reduced error obtained by exploiting QM/EE and QM/FQ approaches as compared to the implicit (QM/PCM) method shows that an accurate, dynamic description of the solute−solvent interactions is needed, for both apolar (DIO) and polar solvents. Also, the polarizable QM/FQ outperforms the non-polarizable QM/EE when compared to the experimental data, thus showing that solute−solvent polarization plays a crucial role in determining the electronic properties of PNA in solution. Finally, the almost perfect agreement between QM/FQ and the experimental data clearly demonstrates the reliability of the novel FQ parametrization.

**3.2. Quinolinium Betaine.** Quinolinium betaine (QB, see Figure 1) has a zwitterionic character, therefore it is strongly hydrophilic. Its absorption spectrum is dominated by the transition from the dipolar ground state (GS) to an excited state (ES) of considerably reduced polarity.[83] The GS is, therefore, stabilized in polar solvents, and this leads to an increase of the transition energy, that is, to a positive solvatochromism. In this work, we have investigated the solvatochromic shift of QB dissolved in DIO, THF, ACN, MET, and WTR.

For all solvents and embedding methods, the lowest bright excitation of QB corresponds to the HOMO−LUMO $\pi \rightarrow \pi^*$ transition, which has a partial CT character (see Figure 6a).

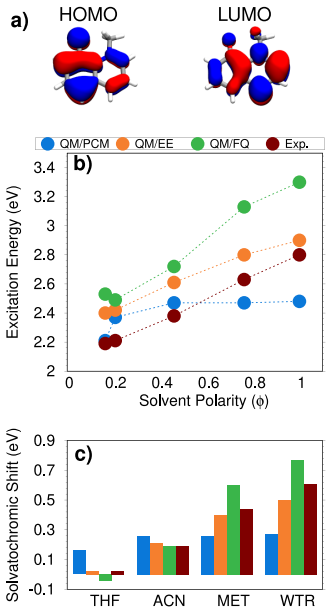


**Figure 6.** (a) QB HOMO and LUMO involved in the studied electronic transition. (b) QM/PCM, QM/EE, QM/FQ, and experimental QB excitation energies as a function of the solvent polarity ($\phi$). (c) QM/PCM, QM/EE, QM/FQ, and experimental QB solvatochromic shifts computed with respect to the excitation energy in dioxane.

Calculated QM/PCM, QM/EE, and QM/FQ excitation energies as a function of solvent polarity ($\phi$) are reported in Figure 6b, together with the experimental values taken from ref 83. Similar to PNA, QM/PCM is able to reproduce the experimental trend only for the less-polar solvents (DIO and THF), while, as expected, the curve is substantially flat for the most polar solvents (ACN, MET, and WTR). On the contrary, both QM/EE and QM/FQ well reproduce the experimental trend. Different from PNA, in this case, QM/EE excitation energies are closer to experiments than QM/FQ ones. Such a good agreement may be ascribed to systematic errors due to the selected level of theory;[38] therefore, in the following we will mainly focus on energy differences, that is, solvatochromic shifts, which are less affected by systematic errors.



https://doi.org/10.1021/acs.jctc.1c00763
J. Chem. Theory Comput. 2021, 17, 7146−7156

Finally, in Figure 6c, computed and experimental solvatochromic shifts are reported. Note that they are calculated with respect to DIO, due to the lack of experimental spectra of QB in the gas phase reported in literature. Figure 6c clearly shows that QM/PCM cannot reproduce the experimental trend for the most polar solvents, whereas both QM/EE and QM/FQ computed solvatochromic shifts increase as the solvent polarity increases. In particular, we notice that for ACN, the two atomistic approaches yield almost the same value (with QM/FQ being in almost perfect agreement with experiments). For MET and WTR, QM/FQ computed shifts are larger than their experimental counterparts, whereas the opposite occurs for QM/EE. This behavior can be due to the fact that Pauli repulsion effects, which might be large for MET and, especially, WTR,[81] are neglected in our calculations. The inclusion of such effects, which are always repulsive, would bring computed values toward the experimental findings because they act in the opposite direction with respect to QM/FQ electrostatic and polarization contributions.

To conclude this section on QB, it is worth noticing that the QM/FQ solvatochromic shift in THF is wrongly predicted in sign (negative instead of positive). However, the QM/FQ error is of about 0.06 eV (~1.3 kcal/mol), thus the absolute discrepancy can be considered satisfactory.

**3.3. Brooker's Merocyanine.** MER also known as Brooker's merocyanine[84] has been amply studied both experimentally and theoretically due to the sensitivity of its absorption spectrum on the solvent polarity.[85−88] Similar to PNA and QB, MER is characterized by two resonance structures, neutral (quinoid) and zwitterionic (benzenoid). The latter is stabilized by polar solvents, whereas the neutral form is predominant in apolar solvents. Also, the phenolate oxygen atom can form hydrogen bonds with protic solvents, thus further increasing the weight of the zwitterionic form.[88−90] For the aforementioned reasons, MER is used as an indicator to measure solvents' polarity and hydrogen bond donor capability.

In this work, we focus on the MER absorption spectra in THF, ACN, ETH, and WTR. MER lowest bright excitation corresponds to a HOMO−LUMO $\pi \rightarrow \pi^*$ transition, independent of the solvent and the solvation approach. Figure 7 reports the pictures of MOs involved in the transition, which clearly has CT character, as the density moves from nitrogen to oxygen. In Figure 7b, experimental[86,87] MER excitation energies as a function of the solvent polarity are compared with the computed results obtained at the QM/PCM, QM/EE, and QM/FQ levels. QM/PCM excitation energies are placed around 2.6 eV, in sharp contrast with experiments, which report an almost linear increase of transition energies by increasing the solvent polarity. Remarkably, this trend is reproduced by QM/FQ, whereas, similar to QM/PCM, QM/EE excitation energies are almost constant in all solvents, with a slight increase when MER is dissolved in WTR.

Computed and experimental solvatochromic shifts with respect to DIO are reported in Figure 7c. Although QM/FQ solvatochromic shifts are underestimated for ETH and WTR, the QM/FQ results directly follow the experimental trend, whereas both the QM/PCM and QM/EE solvatochromic shifts are almost unaffected by solvent polarity. Such a behavior demonstrates the important role of both the specific and polarization solute−solvent effects. To conclude the discussion on MER, we also computed MER gas-phase vertical excitation energy, which is reported in Tables S4 and S6, given as

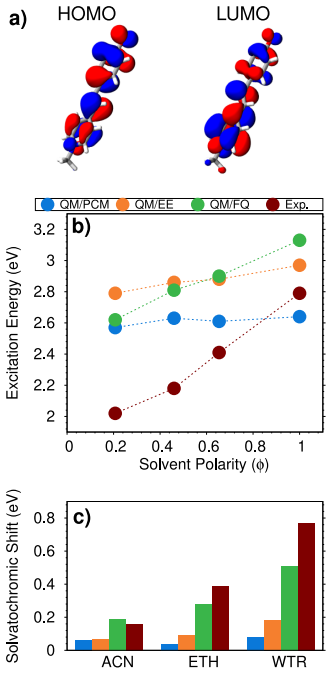


**Figure 7.** (a) MER HOMO and LUMO involved in the studied electronic transition. (b) QM/PCM, QM/EE, QM/FQ, and experimental MER excitation energies as a function of the solvent polarity ($\phi$). (c) QM/PCM, QM/EE, QM/FQ, and experimental MER solvatochromic shifts computed with respect to excitation energy in dioxane.

Supporting Information. QM/FQ is able to reproduce both the experimentally measured positive and negative solvatochromic shifts in highly polar (ETH and WTR) and medium-to-low polarity solvents, respectively;[89] remarkably, such a behavior cannot be described using QM/PCM.

**3.4. Reichardt's Betaine (BET).** Solvent effects induce dramatic shifts in the BET absorption spectrum, and for this reason BET has been used to develop the Reichardt's polarity index ET(30), which is probably the most popular solvent polarity scale.[2,9,91,92]

The absorption spectrum of BET as dissolved in DIO, ACN, MET, and WTR has been computed by modeling the solvent effects by means of the QM/PCM, QM/EE, or QM/FQ approaches. BET lowest excitation, of clear CT character (see 8a), corresponds to the HOMO−LUMO $\pi \rightarrow \pi^*$ transition for all considered solvents and solvation approaches. Experimental[86,87] excitation energies as a function of the solvent polarity are given in Figure 8b, together with the computed values. Clearly, the experimental data linearly depend on the solvent polarity, whereas both the QM/EE and QM/PCM values flatten out by increasing the solvent polarity. Remarkably, among the tested approaches, QM/FQ is the only one that is able to model the experimentally observed trend.

In Figure 8c, we finally report computed and experimental solvatochromic shifts. Reference excitation energies in vacuo are 1.66 (experimental) and 1.18 (calculated) eV. BET values confirm what has already been discussed for the previous molecules. QM/PCM cannot reproduce experimental solvatochromic shifts for the most polar and protic solvents, whereas


https://doi.org/10.1021/acs.jctc.1c00763
J. Chem. Theory Comput. 2021, 17, 7146−7156

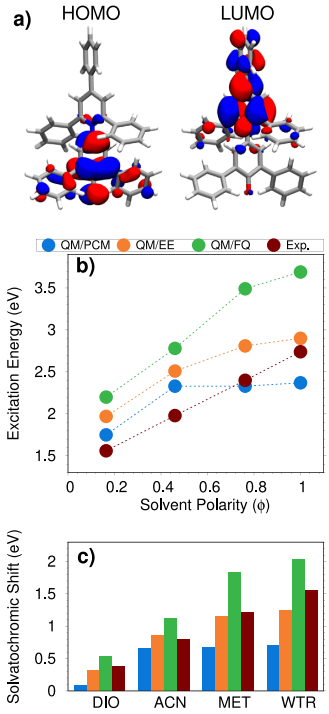


**Figure 8.** (a) BET HOMO and LUMO involved in the studied electronic transition. (b) QM/PCM, QM/EE, QM/FQ, and experimental BET excitation energies as a function of the solvent polarity ($\phi$). (c) QM/PCM, QM/EE, QM/FQ, and experimental BET solvatochromic shifts computed with respect to gas-phase excitation energy.

the QM/EE results are in good agreement with the experimental results, especially for DIO, ACN and MET. QM/FQ always overestimates the experimental values, similar to the case of QB (see above). However, also for BET the good performance of QM/EE can be ascribed to a fortunate error cancellation, due to the fact that both Pauli repulsion and solute−solvent polarization effects are neglected (the latter are instead considered by QM/FQ, and are large).

**3.5. Discussion.** In this section, we further study the quality of the computational approach, by focusing on general trends for all four molecules. First, we investigate band broadening by moving from apolar to polar protic solvents. To this end, the stick spectra, displayed as histograms, of the four chromophores in the different solvents are reported in Figure 9. Clearly, by moving from DIO to WTR, the absorption band broadens out. By fitting the different absorption spectra with Gaussian functions, we see that their full width at half-maximum (fwhm) values, which are a direct measure of band broadening, are substantially influenced by the solvent. The increase of band broadening is particularly evident for BET, for which the fwhm in WTR is 65% larger than that in DIO (0.71 vs 0.43 eV). Because BET is kept frozen during MD runs, broadening arises from fluctuations of solvent molecules around the solute. From the physicochemical point of view, this is not unexpected. In fact, for strongly interacting solvents, such as MET and WTR, which can interact with BET via HB interactions, such fluctuations yield to a larger scattering of absorption energies as compared to apolar non-protic solvents, such as DIO.

The reliability of the method can also be investigated by studying the dependence of GS and ES dipole moments (in debye) as a function of the solvent polarity $\phi$ (see Figure 10). We first notice that PNA differs from other solutes, because its GS dipole moment is lower than the ES one, independently of the solvent polarity. This is clearly reflected by the negative solvatochromic shifts reported for PNA only. However, for all studied systems, an almost linear dependence of both GS and ES dipole moments as a function of the solvent polarity is predicted. Remarkably, ETH, MET, and WTR values (see for instance MER, QB, and BET) deviate from linearity, being such a behaviour possibly explained by the fact that protic solvents may not be barely described by the solvent polarity index, which does not take into account strong, directional solute−solvent interactions.

Finally, in Figure 11, correlation maps between the experimental ($\Delta E_{exp}$) solvatochromic shifts and the calculated QM/PCM (left panel, $\Delta E_{QM/PCM}$), QM/EE (middle panel, $\Delta E_{QM/EE}$), and QM/FQ (right panel, $\Delta E_{QM/FQ}$) values are reported.

For PNA (circles), QM/FQ deviations with respect to experimental values oscillate from a minimum value of 0.03 eV for DIO and MET to a maximum value of 0.19 eV for THF. A similar behavior is observed for QB, where the largest discrepancy is observed for WTR (0.17 eV), whereas for MER, the largest error increases up to 0.26 eV (WTR). As already commented above, the largest deviations are observed for BET. However, we remark that such discrepancies can be attributed to the solute geometry being kept frozen during MD runs and also to the fact that solute−solvent interactions are limited to electrostatic (and polarization) contributions, and other quantum forces may be in place for some of the studied molecules. This is for instance the case of BET in WTR; in fact, if Pauli repulsion is included by resorting to the approach that we have presented in ref 23 and extended to TD-DFT in ref 81, for aqueous BET the error moves from 0.46 to 0.1 eV. We finally remark that vibronic effects may affect computed accurate solvatochromic shifts.[82] Gas-phase vibronic UV−vis spectra of the studied systems within the vertical gradient approximation[93] are reported in Table S6 in the Supporting Information, showing that such terms can be as large as 0.1 eV.

Finally, let us compare QM/FQ to QM/EE and QM/PCM. QM/FQ outperforms the other two approaches, resulting in mean error of about 0.18 eV with respect to 0.25 and 0.43 eV, as it is obtained by using QM/EE and QM/PCM, respectively. Not surprisingly, QM/PCM gives the worst values, thus showing the limitations of continuum solvation and the necessity of explicit treatment of protic, polar solvents. On the other hand, the reduced errors of QM/FQ compared to those of QM/EE demonstrate that polarization effects are relevant to the description of solvatochromic shifts.

## 4. SUMMARY AND CONCLUSIONS

In this work, we have extended the applicability of QM/FQ to different solvents of various polarities and hydrogen-bonding capabilities. QM/FQ has been challenged to reproduce solvatochromic shifts of four dyes dissolved in different solvents, giving a reliable description of the experimental trends. Remarkably, in most cases, the QM/FQ results are in much better agreement with the experimental values than other approaches, which lack the description of polarization



https://doi.org/10.1021/acs.jctc.1c00763
J. Chem. Theory Comput. 2021, 17, 7146−7156

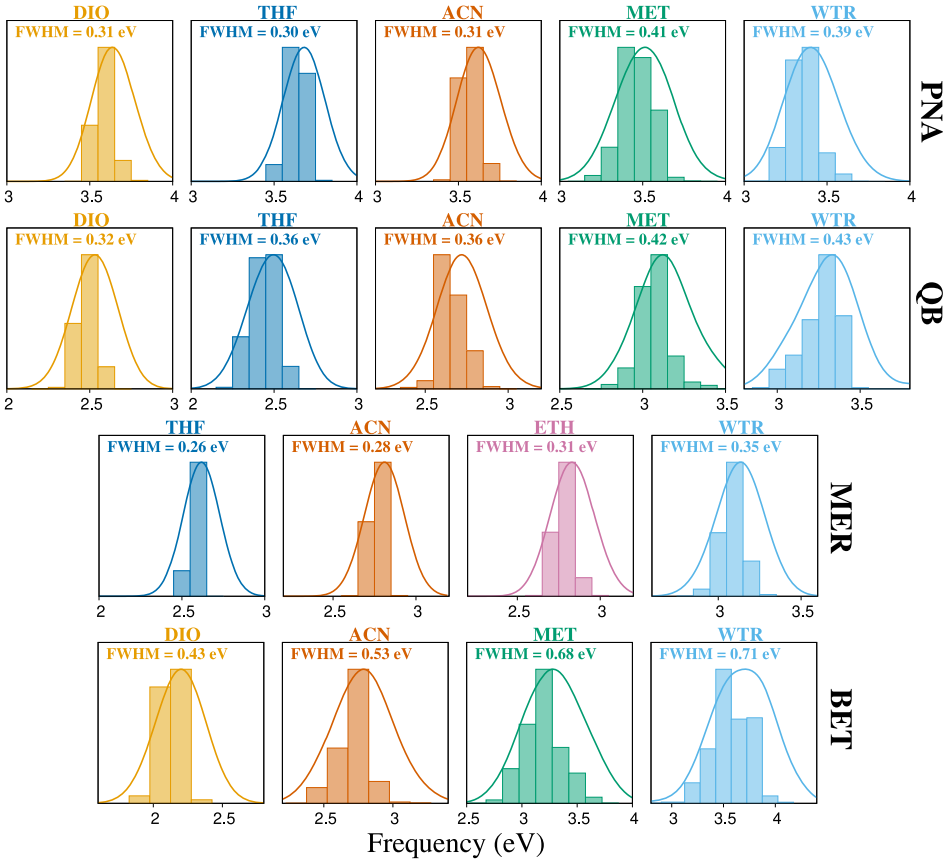


**Figure 9.** QM/FQ excitation energy distributions of PNA, QB, MER, and BET dissolved in different solvents of increasing polarity. The fwhm of each band is also reported (in eV).

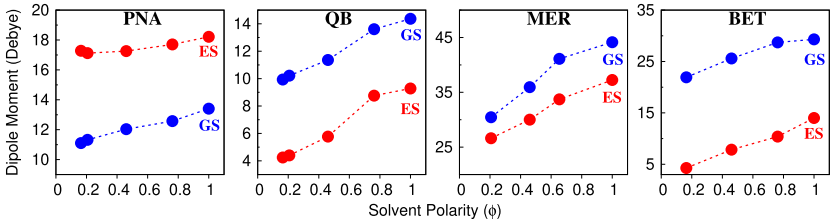


**Figure 10.** QM/FQ PNA, QB, MER, and BET ground (GS, blue) and excited (ES, red) dipole moments (in debye) as a function of the solvent polarity index, ($\phi$).

effects (QM/EE) or any atomistic description of the solvent molecules (QM/PCM), the latter being particularly relevant for protic solvents. Also, QM/FQ errors with respect to the experiments are larger when non-electrostatic interactions play a crucial role. Notably, neither THF nor ETH were specifically parameterized by means of the proposed parametrization procedure. In fact, in both cases, we exploited the optimized parameters for DIO and MET, respectively. This demonstrates a good level of transferability of the parameters to treat molecules with similar chemical structures.

The FQ force field lacks a multipolar expansion of electrostatic interactions, because it only uses electric charges; therefore, short-range electrostatics might be wrongly described. Such an approximation seems not to be particularly relevant for the studied cases; however, it can be solved by extending the electrostatic expansion, as it has been pragmatically proposed by some of us for the QM/FQF$\mu$ approach,[35] which can be parametrized for various solvents in a similar way to that studied in this work. This topic is currently under investigation in our group, and will be the topic of a forthcoming communication. Finally, geometrical effects are crucial to get a good reproduction of experimental excitation energies. Therefore, the QM/FQ results can be further improved by resorting to QM/MM simulations, possibly coupled to enhanced sampling techniques.[94] Investigation of these issues is underway and will be reported in future works.



https://doi.org/10.1021/acs.jctc.1c00763
J. Chem. Theory Comput. 2021, 17, 7146−7156

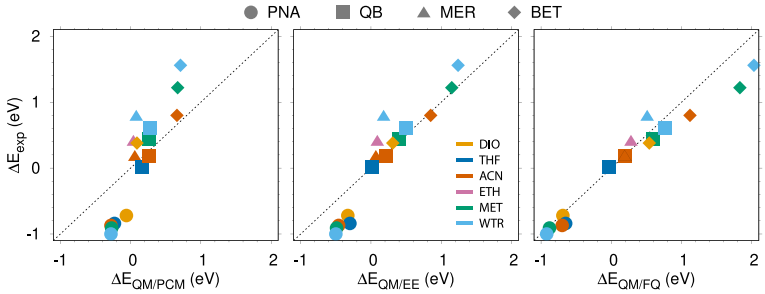


**Figure 11.** PNA, QB, MER and BET QM/PCM (left), QM/EE (middle), and QM/FQ (right) solvatochromic shifts ($\Delta E$) with respect to the experimental values ($\Delta E_{exp}$).

## ■ ASSOCIATED CONTENT

### Supporting Information

The Supporting Information is available free of charge at https://pubs.acs.org/doi/10.1021/acs.jctc.1c00763.

FQ parameters for the selected solvents and QM/FQ, QM/PCM, QM/EE, and experimental vertical excitation energies (PDF)

## ■ AUTHOR INFORMATION


### Corresponding Authors

**Tommaso Giovannini** − *Scuola Normale Superiore, 56126 Pisa, Italy*; orcid.org/0000-0002-5637-2853; Email: tommaso.giovannini@sns.it

**Chiara Cappelli** − *Scuola Normale Superiore, 56126 Pisa, Italy*; orcid.org/0000-0002-4872-4505; Email: chiara.cappelli@sns.it

### Authors

**Matteo Ambrosetti** − *Scuola Normale Superiore, 56126 Pisa, Italy*

**Sulejman Skoko** − *Scuola Normale Superiore, 56126 Pisa, Italy*

Complete contact information is available at: https://pubs.acs.org/10.1021/acs.jctc.1c00763


### Notes

The authors declare no competing financial interest.

## ■ ACKNOWLEDGMENTS

This work received funding from the European Research Council (ERC) under the European Union's Horizon 2020 research and innovation programme (grant agreement no. 818064). We gratefully acknowledge the Center for High Performance Computing (CHPC) at SNS for providing the computational infrastructure.

## ■ REFERENCES


(1) Murov, S. L.; Carmichael, I.; Hug, G. L. *Handbook of Photochemistry*; CRC Press, 1993.

(2) Reichardt, C.; Welton, T. *Solvents and Solvent Effects in Organic Chemistry*; John Wiley & Sons, 2011.

(3) Marini, A.; Muñoz-Losa, A.; Biancardi, A.; Mennucci, B. What is solvatochromism? *J. Phys. Chem. B* **2010**, *114*, 17128−17135.

(4) Kamlet, M. J.; Taft, R. W. The solvatochromic comparison method. I. The. beta.-scale of solvent hydrogen-bond acceptor (HBA) basicities. *J. Am. Chem. Soc.* **1976**, *98*, 377−383.

(5) Taft, R. W.; Kamlet, M. J. The solvatochromic comparison method. 2. The. alpha.-scale of solvent hydrogen-bond donor (HBD) acidities. *J. Am. Chem. Soc.* **1976**, *98*, 2886−2894.

(6) Kamlet, M. J.; Abboud, J. L.; Taft, R. W. The solvatochromic comparison method. 6. The. pi.* scale of solvent polarities. *J. Am. Chem. Soc.* **1977**, *99*, 6027−6038.

(7) Kamlet, M. J.; Abboud, J. L. M.; Abraham, M. H.; Taft, R. W. Linear solvation energy relationships. 23. A comprehensive collection of the solvatochromic parameters,. pi.*,. alpha., and. beta., and some methods for simplifying the generalized solvatochromic equation. *J. Org. Chem.* **1983**, *48*, 2877−2887.

(8) Marcus, Y. The properties of organic liquids that are relevant to their use as solvating solvents. *Chem. Soc. Rev.* **1993**, *22*, 409−416.

(9) Reichardt, C. Solvatochromic dyes as solvent polarity indicators. *Chem. Rev.* **1994**, *94*, 2319−2358.

(10) Nigam, S.; Rutan, S. Principles and applications of solvatochromism. *Appl. Spectrosc.* **2001**, *55*, 362A−370A.

(11) Tomasi, J.; Mennucci, B.; Cammi, R. Quantum mechanical continuum solvation models. *Chem. Rev.* **2005**, *105*, 2999−3094.

(12) Mennucci, B. Polarizable Continuum Model. *Wiley Interdiscip. Rev.: Comput. Mol. Sci.* **2012**, *2*, 386−404.

(13) Mennucci, B.; Corni, S. Multiscale modelling of photoinduced processes in composite systems. *Nat. Rev. Chem.* **2019**, *3*, 315−330.

(14) Senn, H. M.; Thiel, W. QM/MM methods for biomolecular systems. *Angew. Chem., Int. Ed.* **2009**, *48*, 1198−1229.

(15) Lin, H.; Truhlar, D. G. QM/MM: what have we learned, where are we, and where do we go from here? *Theor. Chem. Acc.* **2007**, *117*, 185−199.

(16) Sun, Q.; Chan, G. K.-L. Quantum embedding theories. *Acc. Chem. Res.* **2016**, *49*, 2705−2712.

(17) Manby, F. R.; Stella, M.; Goodpaster, J. D.; Miller, T. F., III A simple, exact density-functional-theory embedding scheme. *J. Chem. Theory Comput.* **2012**, *8*, 2564−2568.

(18) Giovannini, T.; Egidi, F.; Cappelli, C. Molecular spectroscopy of aqueous solutions: a theoretical perspective. *Chem. Soc. Rev.* **2020**, *49*, 5664−5677.

(19) Jacob, C. R.; Neugebauer, J.; Jensen, L.; Visscher, L. Comparison of frozen-density embedding and discrete reaction field solvent models for molecular properties. *Phys. Chem. Chem. Phys.* **2006**, *8*, 2349−2359.

(20) Goletto, L.; Giovannini, T.; Folkestad, S. D.; Koch, H. Combining multilevel Hartree−Fock and multilevel coupled cluster approaches with molecular mechanics: a study of electronic excitations in solutions. *Phys. Chem. Chem. Phys.* **2021**, *23*, 4413−4425.

(21) Egidi, F.; Angelico, S.; Lafiosca, P.; Giovannini, T.; Cappelli, C. A polarizable three-layer frozen density embedding/molecular mechanics approach. *J. Chem. Phys.* **2021**, *154*, 164107.

(22) Wesolowski, T. A.; Warshel, A. Frozen density functional approach for ab initio calculations of solvated molecules. *J. Phys. Chem.* **1993**, *97*, 8050−8053.

(23) Giovannini, T.; Lafiosca, P.; Cappelli, C. A General Route to Include Pauli Repulsion and Quantum Dispersion Effects in QM/MM Approaches. *J. Chem. Theory Comput.* **2017**, *13*, 4854−4870.
(24) Slipchenko, L. V. *Many-Body Effects and Electrostatics in Biomolecules*; Pan Stanford, 2016; pp 147−187.
(25) Bondanza, M.; Nottoli, M.; Cupellini, L.; Lipparini, F.; Mennucci, B. Polarizable embedding QM/MM: the future gold standard for complex (bio) systems? *Phys. Chem. Chem. Phys.* **2020**, *22*, 14433−14448.
(26) Giovannini, T.; Egidi, F.; Cappelli, C. Theory and algorithms for chiroptical properties and spectroscopies of aqueous systems. *Phys. Chem. Chem. Phys.* **2020**, *22*, 22864−22879.
(27) Olsen, J. M.; Aidas, K.; Kongsted, J. Excited states in solution through polarizable embedding. *J. Chem. Theory Comput.* **2010**, *6*, 3721−3734.
(28) Olsen, J. M. H.; Kongsted, J. Molecular properties through polarizable embedding. *Adv. Quantum Chem.* **2011**, *61*, 107−143.
(29) Olsen, J. M. H.; Steinmann, C.; Ruud, K.; Kongsted, J. Polarizable density embedding: A new QM/QM/MM-based computational strategy. *J. Phys. Chem. A* **2015**, *119*, 5344−5355.
(30) Ponder, J. W.; Wu, C.; Ren, P.; Pande, V. S.; Chodera, J. D.; Schnieders, M. J.; Haque, I.; Mobley, D. L.; Lambrecht, D. S.; DiStasio, R. A.; Head-Gordon, M.; Clark, G. N. I.; Johnson, M. E.; Head-Gordon, T. Current status of the AMOEBA polarizable force field. *J. Phys. Chem. B* **2010**, *114*, 2549−2564.
(31) Boulanger, E.; Thiel, W. Solvent boundary potentials for hybrid QM/MM computations using classical drude oscillators: a fully polarizable model. *J. Chem. Theory Comput.* **2012**, *8*, 4527−4538.
(32) Boulanger, E.; Thiel, W. Toward QM/MM simulation of enzymatic reactions with the drude oscillator polarizable force field. *J. Chem. Theory Comput.* **2014**, *10*, 1795−1809.
(33) Lipparini, F.; Cappelli, C.; Barone, V. Linear response theory and electronic transition energies for a fully polarizable QM/classical hamiltonian. *J. Chem. Theory Comput.* **2012**, *8*, 4153−4165.
(34) Cappelli, C. Integrated QM/Polarizable MM/Continuum Approaches to Model Chiroptical Properties of Strongly Interacting Solute-Solvent Systems. *Int. J. Quantum Chem.* **2016**, *116*, 1532−1542.
(35) Giovannini, T.; Puglisi, A.; Ambrosetti, M.; Cappelli, C. Polarizable QM/MM approach with fluctuating charges and fluctuating dipoles: the QM/FQF$\mu$ model. *J. Chem. Theory Comput.* **2019**, *15*, 2233−2245.
(36) Giovannini, T.; Riso, R. R.; Ambrosetti, M.; Puglisi, A.; Cappelli, C. Electronic transitions for a fully polarizable qm/mm approach based on fluctuating charges and fluctuating dipoles: linear and corrected linear response regimes. *J. Chem. Phys.* **2019**, *151*, 174104.
(37) Giovannini, T.; Grazioli, L.; Ambrosetti, M.; Cappelli, C. Calculation of ir spectra with a fully polarizable qm/mm approach based on fluctuating charges and fluctuating dipoles. *J. Chem. Theory Comput.* **2019**, *15*, 5495−5507.
(38) Loco, D.; Polack, É.; Caprasecca, S.; Lagardère, L.; Lipparini, F.; Piquemal, J.-P.; Mennucci, B. A QM/MM approach using the AMOEBA polarizable embedding: from ground state energies to electronic excitations. *J. Chem. Theory Comput.* **2016**, *12*, 3654−3661.
(39) Loco, D.; Buda, F.; Lugtenburg, J.; Mennucci, B. The Dynamic Origin of Color Tuning in Proteins Revealed by a Carotenoid Pigment. *J. Phys. Chem. Lett.* **2018**, *9*, 2404−2410.
(40) Loco, D.; Lagardère, L.; Adjoua, O.; Piquemal, J.-P. Atomistic polarizable embeddings: energy, dynamics, spectroscopy, and reactivity. *Acc. Chem. Res.* **2021**, *54*, 2812−2822.
(41) Lipparini, F.; Cappelli, C.; Scalmani, G.; De Mitri, N.; Barone, V. Analytical first and second derivatives for a fully polarizable QM/classical hamiltonian. *J. Chem. Theory Comput.* **2012**, *8*, 4270−4278.
(42) Giovannini, T.; Olszòwka, M.; Cappelli, C. Effective Fully Polarizable QM/MM Approach To Model Vibrational Circular Dichroism Spectra of Systems in Aqueous Solution. *J. Chem. Theory Comput.* **2016**, *12*, 5483−5492.
(43) Giovannini, T.; Olszówka, M.; Egidi, F.; Cheeseman, J. R.; Scalmani, G.; Cappelli, C. Polarizable Embedding Approach for the Analytical Calculation of Raman and Raman Optical Activity Spectra of Solvated Systems. *J. Chem. Theory Comput.* **2017**, *13*, 4421−4435.
(44) Giovannini, T.; Ambrosetti, M.; Cappelli, C. A polarizable embedding approach to second harmonic generation (SHG) of molecular systems in aqueous solutions. *Theor. Chem. Acc.* **2018**, *137*, 74.
(45) Giovannini, T.; Lafiosca, P.; Chandramouli, B.; Barone, V.; Cappelli, C. Effective yet Reliable Computation of Hyperfine Coupling Constants in Solution by a QM/MM Approach: Interplay Between Electrostatics and Non-electrostatic Effects. *J. Chem. Phys.* **2019**, *150*, 124102.
(46) Giovannini, T.; Macchiagodena, M.; Ambrosetti, M.; Puglisi, A.; Lafiosca, P.; Lo Gerfo, G.; Egidi, F.; Cappelli, C. Simulating vertical excitation energies of solvated dyes: From continuum to polarizable discrete modeling. *Int. J. Quantum Chem.* **2019**, *119*, No. e25684.
(47) Gómez, S.; Giovannini, T.; Cappelli, C. Absorption spectra of xanthines in aqueous solution: A computational study. *Phys. Chem. Chem. Phys.* **2020**, *22*, 5929−5941.
(48) Rick, S. W.; Stuart, S. J.; Berne, B. J. Dynamical fluctuating charge force fields: Application to liquid water. *J. Chem. Phys.* **1994**, *101*, 6141−6156.
(49) Rick, S. W.; Stuart, S. J.; Bader, J. S.; Berne, B. J. Fluctuating charge force fields for aqueous solutions. *J. Mol. Liq.* **1995**, *65*−*66*, 31−40.
(50) Rick, S. W.; Berne, B. J. Dynamical Fluctuating Charge Force Fields: The Aqueous Solvation of Amides. *J. Am. Chem. Soc.* **1996**, *118*, 672−679.
(51) Folkestad, S. D.; Kjønstad, E. F.; Myhre, R. H.; Andersen, J. H.; Balbi, A.; Coriani, S.; Giovannini, T.; Goletto, L.; Haugland, T. S.; Hutcheson, A.; et al. e T 1.0: An open source electronic structure program with emphasis on coupled cluster and multilevel methods. *J. Chem. Phys.* **2020**, *152*, 184103.
(52) Stern, H. A.; Kaminski, G. A.; Banks, J. L.; Zhou, R.; Berne, B. J.; Friesner, R. A. Fluctuating charge, polarizable dipole, and combined models: parameterization from ab initio quantum chemistry. *J. Phys. Chem. B* **1999**, *103*, 4730−4737.
(53) Naserifar, S.; Brooks, D. J.; Goddard, W. A., III; Cvicek, V. Polarizable charge equilibration model for predicting accurate electrostatic interactions in molecules and solids. *J. Chem. Phys.* **2017**, *146*, 124117.
(54) Goldberg, D. E.; Holland, J. H. Genetic algorithms and machine learning. *Mach. Learn.* **1988**, *3*, 95.
(55) Kramer, O. *Genetic Algorithm Essentials*; Springer, 2017; pp 11−19.
(56) Garrett, A. *Inspyred*, (version 1.0. 1) inspired intelligence, 2012.
(57) Tonda, A. Inspyred: Bio-inspired algorithms in Python. *Genet. Program. Evolvable Mach.* **2020**, *21*, 269−272.
(58) Chen, J.; Martínez, T. J. Charge conservation in electronegativity equalization and its implications for the electrostatic properties of fluctuating-charge models. *J. Chem. Phys.* **2009**, *131*, 044114.
(59) Abraham, M. J.; Murtola, T.; Schulz, R.; Páll, S.; Smith, J. C.; Hess, B.; Lindahl, E. GROMACS: High Performance Molecular Simulations through Multi-Level Parallelism from Laptops to Supercomputers. *SoftwareX* **2015**, *1*−*2*, 19−25.
(60) Wang, J.; Wolf, R. M.; Caldwell, J. W.; Kollman, P. A.; Case, D. A. Development and testing of a general amber force field. *J. Comput. Chem.* **2004**, *25*, 1157−1174.
(61) Wang, J.; Wang, W.; Kollman, P. A.; Case, D. A. Automatic atom type and bond type perception in molecular mechanical calculations. *J. Mol. Graph. Model.* **2006**, *25*, 247−260.
(62) Wang, J.; Wang, W.; Kollman, P. A.; Case, D. A. Antechamber: an accessory software package for molecular mechanical calculations. *J. Am. Chem. Soc.* **2001**, *222*, U403.
(63) Sousa da Silva, A. W.; Vranken, W. F. ACPYPE-Antechamber python parser interface. *BMC Res. Notes* **2012**, *5*, 367.


https://doi.org/10.1021/acs.jctc.1c00763
J. Chem. Theory Comput. 2021, 17, 7146−7156

(64) Jorgensen, W. L.; Chandrasekhar, J.; Madura, J. D.; Impey, R. W.; Klein, M. L. Comparison of simple potential functions for simulating liquid water. *J. Chem. Phys.* **1983**, *79*, 926−935.
(65) Bayly, C. I.; Cieplak, P.; Cornell, W.; Kollman, P. A. A well-behaved electrostatic potential based method using charge restraints for deriving atomic charges: the RESP model. *J. Phys. Chem.* **1993**, *97*, 10269−10280.
(66) Bussi, G.; Donadio, D.; Parrinello, M. Canonical sampling through velocity rescaling. *J. Chem. Phys.* **2007**, *126*, 014101.
(67) Essmann, U.; Perera, L.; Berkowitz, M. L.; Darden, T.; Lee, H.; Pedersen, L. G. A smooth particle mesh Ewald method. *J. Chem. Phys.* **1995**, *103*, 8577−8593.
(68) Berendsen, H. J. C.; Postma, J. P. M.; van Gunsteren, W. F.; DiNola, A.; Haak, J. R. Molecular dynamics with coupling to an external bath. *J. Chem. Phys.* **1984**, *81*, 3684−3690.
(69) Corni, S.; Cammi, R.; Mennucci, B.; Tomasi, J. Electronic excitation energies of molecules in solution within continuum solvation models: Investigating the discrepancy between state-specific and linear-response methods. *J. Chem. Phys.* **2005**, *123*, 134512.
(70) Duchemin, I.; Guido, C. A.; Jacquemin, D.; Blase, X. The Bethe−Salpeter formalism with polarisable continuum embedding: reconciling linear-response and state-specific features. *Chem. Sci.* **2018**, *9*, 4430−4443.
(71) Guido, C. A.; Chrayteh, A.; Scalmani, G.; Mennucci, B.; Jacquemin, D. Simple Protocol for Capturing Both Linear-Response and State-Specific Effects in Excited-State Calculations with Continuum Solvation Models. *J. Chem. Theory Comput.* **2021**, *17*, 5155.
(72) Frisch, M. J.; Trucks, G. W.; Schlegel, H. B.; Scuseria, G. E.; Robb, M. A.; Cheeseman, J. R.; Scalmani, G.; Barone, V.; Petersson, G. A.; Nakatsuji, H.; Li, X.; Caricato, M.; Marenich, A. V.; Bloino, J.; Janesko, B. G.; Gomperts, R.; Mennucci, B.; Hratchian, H. P.; Ortiz, J. V.; Izmaylov, A. F.; Sonnenberg, J. L.; Williams-Young, D.; Ding, F.; Lipparini, F.; Egidi, F.; Goings, J.; Peng, B.; Petrone, A.; Henderson, T.; Ranasinghe, D.; Zakrzewski, V. G.; Gao, J.; Rega, N.; Zheng, G.; Liang, W.; Hada, M.; Ehara, M.; Toyota, K.; Fukuda, R.; Hasegawa, J.; Ishida, M.; Nakajima, T.; Honda, Y.; Kitao, O.; Nakai, H.; Vreven, T.; Throssell, K.; Montgomery, J. A., Jr.; Peralta, J. E.; Ogliaro, F.; Bearpark, M. J.; Heyd, J. J.; Brothers, E. N.; Kudin, K. N.; Staroverov, V. N.; Keith, T. A.; Kobayashi, R.; Normand, J.; Raghavachari, K.; Rendell, A. P.; Burant, J. C.; Iyengar, S. S.; Tomasi, J.; Cossi, M.; Millam, J. M.; Klene, M.; Adamo, C.; Cammi, R.; Ochterski, J. W.; Martin, R. L.; Morokuma, K.; Farkas, O.; Foresman, J. B.; Fox, D. J. *Gaussian 16*, Revision A.03; Gaussian Inc.: Wallingford CT, 2016.
(73) Kosenkov, D.; Slipchenko, L. V. Solvent effects on the electronic transitions of p-nitroaniline: A QM/EFP study. *J. Phys. Chem. A* **2011**, *115*, 392−401.
(74) Marenich, A. V.; Cramer, C. J.; Truhlar, D. G. Electronic absorption spectra and solvatochromic shifts by the vertical excitation model: solvated clusters and molecular dynamics sampling. *J. Phys. Chem. B* **2015**, *119*, 958−967.
(75) Scalmani, G.; Frisch, M. J.; Mennucci, B.; Tomasi, J.; Cammi, R.; Barone, V. Geometries and properties of excited states in the gas phase and in solution: Theory and application of a time-dependent density functional theory polarizable continuum model. *J. Chem. Phys.* **2006**, *124*, 094107.
(76) Stähelin, M.; Burland, D. M.; Rice, J. E. Solvent dependence of the second order hyperpolarizability in p-nitroaniline. *Chem. Phys. Lett.* **1992**, *191*, 245−250.
(77) Wang, C.-K.; Wang, Y.-H.; Su, Y.; Luo, Y. Solvent dependence of solvatochromic shifts and the first hyperpolarizability of para-nitroaniline: a nonmonotonic behavior. *J. Chem. Phys.* **2003**, *119*, 4409−4412.
(78) Thomsen, C. L.; Thøgersen, J.; Keiding, S. R. Ultrafast charge-transfer dynamics: studies of p-nitroaniline in water and dioxane. *J. Phys. Chem. A* **1998**, *102*, 1062−1067.
(79) Kovalenko, S. A.; Schanz, R.; Farztdinov, V. M.; Hennig, H.; Ernsting, N. P. Femtosecond relaxation of photoexcited para-nitroaniline: solvation, charge transfer, internal conversion and cooling. *Chem. Phys. Lett.* **2000**, *323*, 312−322.
(80) Eriksen, J. J.; Sauer, S. P. A.; Mikkelsen, K. V.; Christiansen, O.; Jensen, H. J. A.; Kongsted, J. Failures of TDDFT in describing the lowest intramolecular charge-transfer excitation in para-nitroaniline. *Mol. Phys.* **2013**, *111*, 1235−1248.
(81) Giovannini, T.; Ambrosetti, M.; Cappelli, C. Quantum Confinement Effects on Solvatochromic Shifts of Molecular Solutes. *J. Phys. Chem. Lett.* **2019**, *10*, 5823−5829.
(82) Santoro, F.; Jacquemin, D. Going beyond the vertical approximation with time-dependent density functional theory. *Wiley Interdiscip. Rev.: Comput. Mol. Sci.* **2016**, *6*, 460−486.
(83) Novaki, L. P.; El Seoud, O. A. Solvatochromism in pure solvents: Effects of the molecular structure of the probe. *Ber. Bunsen. Phys. Chem.* **1996**, *100*, 648−655.
(84) Brooker, L. G. S.; Keyes, G. H.; Sprague, R. H.; VanDyke, R. H.; VanLare, E.; VanZandt, G.; White, F. L.; Cressman, H. W. J.; Dent, S. G., Jr. Color and constitution. X. 1 Absorption of the merocyanines2. *J. Am. Chem. Soc.* **1951**, *73*, 5332−5350.
(85) da Silva, D. C.; Ricken, I.; Silva, M. A. d. R.; Machado, V. G. Solute−solvent and solvent−solvent interactions in the preferential solvation of Brooker's merocyanine in binary solvent mixtures. *J. Phys. Org. Chem.* **2002**, *15*, 420−427.
(86) Morley, J. O.; Morley, R. M.; Fitton, A. L. Spectroscopic studies on Brooker's merocyanine. *J. Am. Chem. Soc.* **1998**, *120*, 11479−11488.
(87) Cavalli, V.; da Silva, D. C.; Machado, C.; Machado, V. G.; Soldi, V. The fluorosolvatochromism of Brooker's merocyanine in pure and in mixed solvents. *J. Fluoresc.* **2006**, *16*, 77−86.
(88) Abdel-Halim, S. T.; Awad, M. K. Absorption, fluorescence, and semiempirical ASED-MO studies on a typical Brooker's merocyanine dye. *J. Mol. Struct.* **2005**, *754*, 16−24.
(89) Jacques, P. On the relative contributions of nonspecific and specific interactions to the unusual solvtochromism of a typical merocyanine dye. *J. Phys. Chem.* **1986**, *90*, 5535−5539.
(90) Abdel-Halim, S. T.; Abdel-Kader, M. H.; Steiner, U. E. Thermal cis-trans isomerization of solvatochromic merocyanines: linear correlations between solvent polarity and adiabatic and diabatic transition energies. *J. Phys. Chem.* **1988**, *92*, 4324−4328.
(91) Reichardt, C. Pyridinium N-phenolate betaine dyes as empirical indicators of solvent polarity: Some new findings. *Pure Appl. Chem.* **2004**, *76*, 1903−1919.
(92) Reichardt, C. Polarity of ionic liquids determined empirically by means of solvatochromic pyridinium N-phenolate betaine dyes. *Green Chem.* **2005**, *7*, 339−351.
(93) Santoro, F.; Cappelli, C.; Barone, V. Effective Time-Independent Calculations of Vibrational Resonance Raman Spectra of Isolated and Solvated Molecules Including Duschinsky and Herzberg−Teller Effects. *J. Chem. Theory Comput.* **2011**, *7*, 1824−1839.
(94) Laio, A.; Parrinello, M. Escaping free-energy minima. *Proc. Natl. Acad. Sci. U.S.A.* **2002**, *99*, 12562−12566.


https://doi.org/10.1021/acs.jctc.1c00763
J. Chem. Theory Comput. 2021, 17, 7146−7156

# Supporting Information - QM/Fluctuating Charge Protocol to Compute Solvatochromic Shifts

Matteo Ambrosetti, Sulejman Skoko, Tommaso Giovannini,* and Chiara Cappelli*

*Scuola Normale Superiore, Piazza dei Cavalieri 7, 56126 Pisa, Italy.*

E-mail: tommaso.giovannini@sns.it; chiara.cappelli@sns.it

Table S1: FQ optimal parameters (electronegativity $\chi$ and chemical hardness $\eta$) obtained by exploiting the parametrization procedure. All atomic electronegativities are reported as differences with respect to the least electronegative atom, i.e. Hydrogen ($\Delta\chi_{X-H}$). All data are given in a.u.

| Solvent | $\Delta\chi_{C-H}$ | $\Delta\chi_{N-H}$ | $\Delta\chi_{O-H}$ | $\eta_H$ | $\eta_C$ | $\eta_N$ | $\eta_O$ |
|---|---|---|---|---|---|---|---|
| DIO | 0.09 | – | 0.14 | 0.58 | 0.40 | – | 0.46 |
| ACN | 0.04 | 0.16 | – | 0.57 | 0.38 | 0.45 | – |
| MET | 0.18 | – | 0.37 | 0.52 | 0.17 | – | 0.95 |
| WTR | – | – | 0.15 | 0.44 | – | – | 0.54 |

Table S2: QM/PCM $\omega_0$, LR, cLR and cLR$^2$ excitation energies of PNA, QB, MER and BET dissolved in the selected solvents. All data are reported in eV.

| **PNA** | | | | |
|---|---|---|---|---|
| Solvent | $\omega_0$ | LR | cLR | cLR$^2$ |
| DIO | 4.15 | 4.04 | 4.07 | 3.96 |
| THF | 4.00 | 3.88 | 3.90 | 3.78 |
| ACN | 3.93 | 3.82 | 3.84 | 3.73 |
| MET | 3.93 | 3.83 | 3.85 | 3.74 |
| WTR | 3.92 | 3.81 | 3.84 | 3.73 |
| **QB** | | | | |
| Solvent | $\omega_0$ | LR | cLR | cLR$^2$ |
| DIO | 2.32 | 2.30 | 2.23 | 2.21 |
| THF | 2.51 | 2.49 | 2.39 | 2.37 |
| ACN | 2.61 | 2.59 | 2.48 | 2.47 |
| MET | 2.61 | 2.59 | 2.49 | 2.47 |
| WTR | 2.62 | 2.61 | 2.50 | 2.48 |
| **MER** | | | | |
| Solvent | $\omega_0$ | LR | cLR | cLR$^2$ |
| THF | 2.82 | 2.58 | 2.80 | 2.57 |
| ACN | 2.86 | 2.66 | 2.82 | 2.63 |
| ETH | 2.85 | 2.65 | 2.81 | 2.61 |
| WTR | 2.87 | 2.68 | 2.83 | 2.64 |
| **BET** | | | | |
| Solvent | $\omega_0$ | LR | cLR | cLR$^2$ |
| DIO | 1.94 | 1.92 | 1.78 | 1.75 |
| ACN | 2.60 | 2.58 | 2.34 | 2.33 |
| MET | 2.59 | 2.58 | 2.34 | 2.33 |
| WTR | 2.64 | 2.63 | 2.38 | 2.37 |

Table S3: QM/FQ $\omega_0$, LR, cLR and cLR$^2$ excitation energies of PNA, QB, MER and BET dissolved in the selected solvents. All data are reported in eV.

| **PNA** | | | | |
|---|---|---|---|---|
| Solvent | $\omega_0$ | LR | cLR | cLR$^2$ |
| DIO | 3.86 | 3.72 | 3.78 | 3.64 |
| THF | 3.86 | 3.74 | 3.80 | 3.68 |
| ACN | 3.77 | 3.67 | 3.73 | 3.63 |
| MET | 3.70 | 3.56 | 3.65 | 3.45 |
| WTR | 3.61 | 3.46 | 3.57 | 3.41 |
| **QB** | | | | |
| Solvent | $\omega_0$ | LR | cLR | cLR$^2$ |
| DIO | 2.64 | 2.62 | 2.55 | 2.53 |
| THF | 2.59 | 2.57 | 2.51 | 2.49 |
| ACN | 2.80 | 2.78 | 2.74 | 2.72 |
| MET | 3.30 | 3.26 | 3.17 | 3.13 |
| WTR | 3.46 | 3.41 | 3.35 | 3.30 |
| **MER** | | | | |
| Solvent | $\omega_0$ | LR | cLR | cLR$^2$ |
| THF | 2.87 | 2.63 | 2.85 | 2.62 |
| ACN | 3.00 | 2.83 | 2.98 | 2.81 |
| ETH | 3.26 | 2.98 | 3.19 | 2.90 |
| WTR | 3.38 | 3.18 | 3.33 | 3.13 |
| **BET** | | | | |
| Solvent | $\omega_0$ | LR | cLR | cLR$^2$ |
| DIO | 2.45 | 2.43 | 2.22 | 2.20 |
| ACN | 2.95 | 2.94 | 2.79 | 2.78 |
| MET | 3.57 | 3.55 | 3.30 | 3.49 |
| WTR | 3.90 | 3.88 | 3.71 | 3.69 |

Table S4: QM/EE Excitation energies (eV) of the studied molecules dissolved in the selected solvents. Computed excitation energies in gas-phase (VAC) are also given.

| Solute | VAC | DIO | THF | ACN | ETH | MET | WTR |
|---|---|---|---|---|---|---|---|
| PNA | 4.33 | 4.00 | 4.03 | 3.87 | – | 3.84 | 3.83 |
| QB | 2.14 | 2.40 | 2.42 | 2.61 | – | 2.80 | 2.90 |
| MER | 2.92 | – | 2.79 | 2.86 | 2.88 | – | 2.97 |
| BET | 1.66 | 1.97 | – | 2.51 | – | 2.81 | 2.90 |

Table S5: Experimental excitation energies (eV) of the studied molecules dissolved in the selected solvents. Experimental excitation energies in gas-phase (VAC) are also given.

| Solute | VAC | DIO | THF | ACN | ETH | MET | WTR |
|---|---|---|---|---|---|---|---|
| PNA[1,2] | 4.26 | 3.54 | 3.42 | 3.39 | – | 3.35 | 3.26 |
| QB[3] | – | 2.19 | 2.21 | 2.38 | – | 2.63 | 2.80 |
| MER[4,5] | – | – | 2.02 | 2.18 | 2.41 | – | 2.79 |
| BET[6] | 1.18 | 1.56 | – | 1.98 | – | 2.40 | 2.74 |

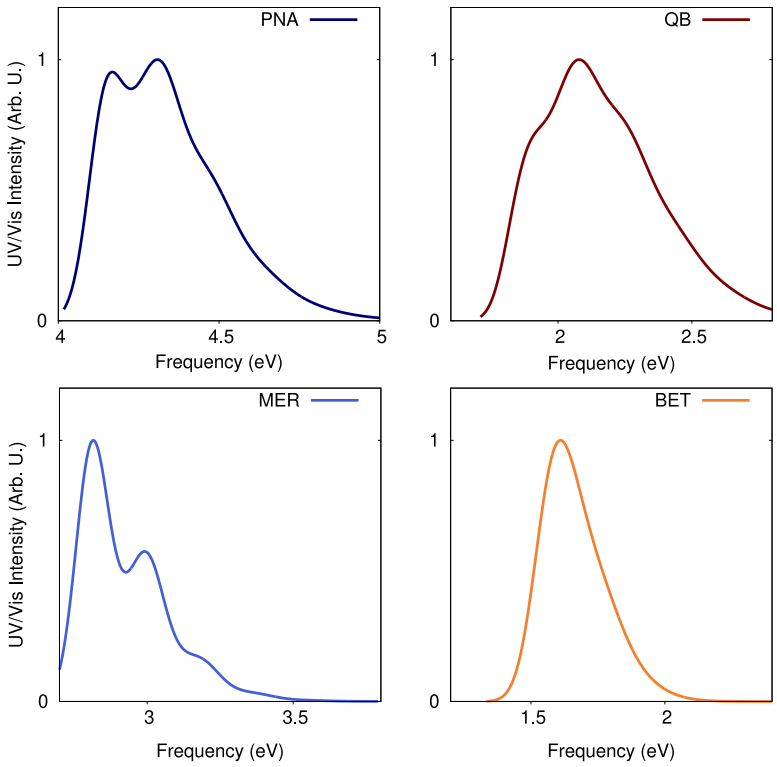


Figure S1: Gas-phase PNA, QB, MER and BET Vibronic Vertical Gradient (VG) UV/Vis Intensities.

Table S6: Gas-phase PNA, QB, MER and BET Vertical and Vibronic Excitation energies maxima. All data are given in eV.

| Solute | Vertical | Vibronic (VG) |
|---|---|---|
| PNA | 4.33 | 4.31 |
| QB | 2.14 | 2.08 |
| MER | 2.92 | 2.82 |
| BET | 1.66 | 1.61 |

# References


(1) Kovalenko, S.; Schanz, R.; Farztdinov, V.; Hennig, H.; Ernsting, N. Femtosecond relaxation of photoexcited para-nitroaniline: solvation, charge transfer, internal conversion and cooling. *Chem. Phys. Lett.* **2000**, *323*, 312–322.

(2) Stähelin, M.; Burland, D.; Rice, J. Solvent dependence of the second order hyperpolarizability in p-nitroaniline. *Chem. Phys. Lett.* **1992**, *191*, 245–250.

(3) Novaki, L. P.; El Seoud, O. A. Solvatochromism in pure solvents: Effects of the molecular structure of the probe. *Berichte der Bunsengesellschaft für physikalische Chemie* **1996**, *100*, 648–655.

(4) Morley, J. O.; Morley, R. M.; Fitton, A. L. Spectroscopic studies on Brooker's merocyanine. *J. Am. Chem. Soc.* **1998**, *120*, 11479–11488.

(5) Cavalli, V.; da Silva, D. C.; Machado, C.; Machado, V. G.; Soldi, V. The fluorosolvatochromism of Brooker's merocyanine in pure and in mixed solvents. *J. Fluoresc.* **2006**, *16*, 77–86.

(6) Reichardt, C. Solvatochromic dyes as solvent polarity indicators. *Chem. Rev.* **1994**, *94*, 2319–2358.

# CHAPTER 5

# Towards a Cost-Effective Modeling of Fluorescence in the Condensed Phase

Dyes and Pigments 215 (2023) 111227

Contents lists available at ScienceDirect

Dyes and Pigments

journal homepage: www.elsevier.com/locate/dyepig

# Towards a cost-effective modeling of fluorescence in the condensed phase

Sulejman Skoko [a], Cosimo Micheletti [b], Emanuele Grifoni [a], Franco Egidi [a,1], Tommaso Giovannini [a], Andrea Pucci [b], Chiara Cappelli [a,*]

[a] Scuola Normale Superiore, Piazza dei Cavalieri, 7, Pisa, 56126, Italy
[b] Dipartimento di Chimica e Chimica Industriale, Università di Pisa, Via G. Moruzzi 13, Pisa, 56124, Italy

ARTICLE INFO

*Keywords:*
QM/MM
QM/FQ
Molecular dynamics
Stokes shift
Excitation energies
Solvent effects

ABSTRACT

We propose a synergistic computational/experimental investigation of fluorescence spectra in aqueous solution. As a powerful tool to analyze and interpret experimental findings, we develop a reliable and cost-effective computational protocol, which is able to correctly describe the solute-solvent interactions which can highly affect the spectral signal. To this purpose, the model not only takes into account specific, strong hydrogen bonding interactions, but also the dynamical aspects of the solvation phenomenon in both the ground and, remarkably, excited state. The computational protocol is tested against the reproduction of experimentally measured spectra of representative water soluble fluorescent dyes. An almost perfect agreement is reported, thus confirming the reliability of the methodology, that paves the way for a cost-effective investigation of ES properties of solvated systems.

## 1. Introduction

Among the many properties that can be computed by exploiting quantum mechanics (QM), the accurate prediction of spectral features of molecular systems embedded in an external environment is still one of the major challenges of computational chemistry [1]. This is due to the large number of degrees of freedom which need to be simultaneously described, making a full QM treatment unfeasible at reasonable computational cost [2]. Furthermore, from the physico-chemical point of view, a full QM description is unnecessary because the measured spectral fingerprints are usually related to a small portion of the system, the chromophore, whose electronic properties are perturbed by the presence of the environment. The latter on the other hand is a crucial component of the whole system, affecting the molecular response of the target system, but it does not itself determine the measured spectrum [1,3]. For this reason, the most successful theoretical approaches to deal with this problem belong to the family of focused models [4]. Within such a paradigm, the target system is described at the QM level, whereas the environment is included at a lower level of theory.

In particular, the most efficient methods, in terms of computational cost and accuracy, are the QM/Molecular Mechanics (QM/MM) approaches [5,6], in which the environment is described by means of classical force fields (FF). What separates all the different QM/MM approaches is the way they treat the QM/MM interaction, which may include the mutual polarization between the two layers (polarizable QM/MM approaches) [7–11] and, in rare cases, non-electrostatic effects such as Pauli repulsion and dispersion interactions [12–14].

QM/MM methods are particularly advantageous if strong, specific, molecule-environment interactions take place, as is the case for aqueous solutions [1,15]. Among the plethora of the different QM/MM approaches developed in the literature, the polarizable QM/Fluctuating Charge (QM/FQ) [1,4,16–18] has been shown to yield a physically consistent description of aqueous solutions, in particular when coupled with an accurate description of Pauli repulsion forces [19]. The resulting QM/FQ + rep approach, coupled with an adequate sampling of the solute-solvent phase-space, indeed represents the state-of-the-art model to describe molecular properties and spectroscopies of aqueous solutions [1].

Despite its potential, to date QM/FQ + rep has been applied to describe ground state (GS) properties only [1,14]. In this paper, we extend QM/FQ + rep to the description of fluorescence spectra, by also proposing a computational protocol which is able to take into account the peculiar features of solute-solvent interactions related to this phenomenon. In fact, despite the fundamental importance of fluorescence in many fields [20–22], theoretically consistent descriptions for general solute-solvent couples are still lacking. This is especially true for models

* Corresponding author.
*E-mail address:* chiara.cappelli@sns.it (C. Cappelli).
[1] present address: Software for Chemistry & Materials BVDe Boelelaan 10831081 HV Amsterdam The Netherlands

https://doi.org/10.1016/j.dyepig.2023.111227
Received 27 October 2022; Received in revised form 7 March 2023; Accepted 7 March 2023
Available online 15 March 2023

capable at the same time to describe the phase space of the electronically excited solvated system and include the effects of intermolecular interactions, such as hydrogen bonds. Indeed, differently from the GS, for which a plethora of approaches can indeed be exploited, the ES sampling is far from trivial. Clearly, this is primarily due to the fact that such a sampling requires in principle a QM description of, at least, a portion of the system, which is usually the chromophore undergoing the electronic transition. Moreover, when dealing with solvated systems, the reorganization of the solvent around the molecule in its ES also needs to be correctly described. The two aforementioned issues, which are absent for gas-phase simulations, have amply hampered the development of computational studies of ES-related properties at the QM/MM level. Indeed, the development of cost-effective, yet accurate computational protocols for describing ES-related properties bridges a gap in the field of fully atomistic approaches for spectroscopy, paving the way to the reliable modeling of optical properties of chromophores embedded in complex environments, including biological matrices and surfaces.

In this paper, the aspects mentioned above are considered by means of a computational protocol, which couples QM/FQ + rep to classical MD simulations. To make classical MD simulations able to correctly sample the ES, we force FF terms to mimic ES properties, i.e. energies, gradients and Hessian, and electronic density in terms of electric charges. The approach is tested by inter-playing computational data and experimental spectra measured on purpose for selected fluorescent dyes in aqueous solution.

The manuscript is organized as follows: in the next section, we discuss how to properly describe the fluorescence properties at the QM/MM level from a physico-chemical perspective, by also focusing on the sampling of both the GS and ES. The approach is then applied to the calculation of absorption and emission spectra of acetone, and four fluorescent dyes, namely fluorescein, basic violet 16, basic yellow 40 and acridine orange, dissolved in aqueous solution. Conclusions and perspectives end the manuscript.

## 2. QM/MM modeling of fluorescence

In the fluorescence processes (Fig. 1), as a result of the absorption of a photon, a vertical excitation of the solute brings a molecule from the GS to a new electronic level while maintaining the original geometry (A). From that, nonradiative relaxation processes bring the system to a lower vibrational state within the same electronic level (B), and finally fluorescence occurs when the excited molecule falls back to the GS (C) [23]. The theoretical description of the processes above is relatively easy

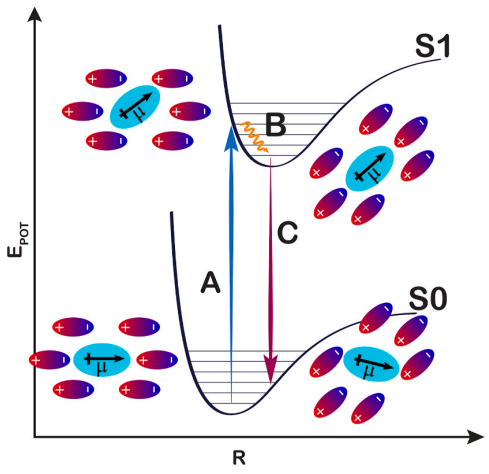


**Fig. 1.** Schematic representation of absorption (A), non-radiative relaxation (B), and emission transitions (C).

in case of a single molecule in the gas-phase, the only delicate aspect of the simulation being the choice of electronic structure method selected to model the ES. In fact, once GS and ES geometries are obtained, vertical excitations A and C may be computed straightforwardly. Choosing the appropriate electronic structure method is still crucial, and this is true for both gas and condensed phase simulations. In this work we resort to Time-Dependent Density Functional Theory (TD-DFT), which can yield reasonably accurate results for most organic systems at low computational cost. Clearly, intrinsic limitations of the chosen electronic structure method are not washed away by the addition of water to the system, no matter how accurately the environment is modeled. TDDFT, for instance, is notoriously unreliable in the modeling of charge-transfer states [24], unless long range corrected functionals are employed. Therefore, the appropriateness of the chosen electronic structure method for the system and property needs always to be checked.

For solute dissolved in solvent, the situation is more difficult and requires further considerations due to solute-solvent interactions and the dynamics of the solvent surrounding the molecule, which can rearrange as a result of the electronic transitions. In fact, different solvation regimes can be considered due to the different time scales associated with the processes depicted in Fig. 1. First, when the solute lies in the GS, the whole system (solute + solvent) is in the so-called equilibrium regime, i.e. all solvent degrees of freedom (electronic, vibrational, rotational and translational) are relaxed and in equilibrium with the solute's ground state. Notice that such an equilibrium is not static, and a single snapshot of the system is not able to account for the intrinsic dynamical effects of the solvation phenomenon. For this reason, the phase-space representing the GS of the entire system needs to be adequately sampled in order to provide a consistent picture [8,25–27]. Indeed, different approaches can be exploited to perform this step, ranging from classical MD simulations to nuclear ensemble (based on Wigner distribution) or enhanced sampling techniques [28–34], and particular care is needed in case of floppy molecules, which can display different local minima (vide infra).

Independently of the sampling method for the GS, the absorption process (A in Fig. 1) is then simulated by calculating the vertical excitations at the QM/MM level on representative structures. At this point, an additional consideration is needed. In fact, the timescale associated to this process is of the order of femtoseconds, and makes the electronic degrees of freedom of the solvent able to readjust to the different solute density, whereas its slower degrees of freedom remain frozen to the solute's GS. This creates a so-called non-equilibrium regime, which has been amply discussed in the context of continuum solvation approaches [35]. By looking at the problem from the TD-DFT perspective, the solvent can be readjusted to the transition densities by assuming that the excitation of the solute is directly associated with the excitation of the solvent [36–38]. However, the solvent fast degrees of freedom can also be re-equilibrated to the excited state density, in a state-specific vision. Such a state-specific equilibration is usually taken into account in an approximated way, by resorting to the so-called corrected Linear Response (cLR), where the polarization sources are obtained as a response to the density of the excited state [36–38]. It is clear that cLR describes the complete fluorescence process depicted in Fig. 1 in a more physically-consistent way, because it includes both polarization and equilibration effects.

During the nonradiative relaxation process, the vibrational degrees of freedom of both the solute and the solvent relax, bringing the system to a novel equilibrium situation, being the lifetime of the ES molecule long enough to allow for such a reorganization. Therefore, the emission process (C, in Fig. 1) takes place from a peculiar situation in which the solvent is in equilibrium with the solute lying in the ES. Indeed, while the majority of the observables need input structures sampled in their electronic GS, fluorescence estimates require excited electronic structures whose dynamic description is far from trivial [23]. A correct sampling of ES structures should be performed by keeping the solute

under constant excitation and letting the solvent molecules free to adapt their positions according to the new state of the solute. This could be done employing ES molecular dynamics (MD) simulations, whereas standard FF parameters are fitted on GS structures and therefore cannot be used to describe ES geometries.

Independently of the method exploited to sample the ES PES, the emission energy is finally computed on a set of representative snapshots at the QM/MM level [39]. A particular attention must be paid at this step to correctly account for the solvation regime. In fact, similarly to the absorption process, also in this case, the vertical transition implies that the solvent fast degrees of freedom readjust to the state-specific solute density [36]. Note that this is conceptually different from the absorption process: in this case, the polarization sources are in equilibrium with the ES density, and the fast degrees of freedom relax to the GS density. Again, this creates a non-equilibrium solvation regime, which is accounted for by computing the cLR emission energies at the QM/MM level.

To conclude this discussion, it is worth noticing that we have described the fluorescence process by commenting on the different solvation regime to which the solute undergoes. In order to effectively describe them without resorting to a full quantum-mechanical description of the system, polarizable embedding, which is indeed able to describe the fast degrees of freedom in terms of a set of polarization sources, is a valuable approach. In fact, in electrostatic embedding, the electrostatic interaction is described by a set of multipoles, usually limited to electric charge, which are fixed and do not vary as a function of the changes in the QM density. This means that the solvation regime is always of equilibrium by definition, and eventual good results are mostly due to error cancellation.

### 2.1. Sampling the ground and excited states

From the above discussion, it is clear that one of the crucial aspects of modeling fluorescence by means of a QM/MM approaches is a proper sampling of both GS and ES phase-spaces. As detailed above, such a sampling may be carried out by resorting to MD. In the context of QM/MM approaches, the GS sampling is usually carried out by means of standard classical MD, which can provide accurate results in case of semi-rigid solutes, for which few minima need to be sampled [1,23]. If this is not the case, different approaches to refine the commonly used classical FF have been developed [13,40–43], based on the reparametrization of selected degrees of freedom on reference data, usually obtained at the QM level [41]. In principle, many other approaches can be exploited to sample the GS phase-space of floppy molecules, ranging from QM/MM MD simulations to meta-dynamics [31,32]. Among them, it is worth mentioning the Joyce procedure [41], which provides a re-parametrization of classical FF's bond and dihedral terms on QM reference data. Joyce is particularly robust and allows for an accurate PES sampling of very floppy molecules [41].

Differently form GS, the ES sampling is particularly difficult. The first intuitive approach would be to perform a GS MD simulation to adequately sample the GS PES. From a set of representative, uncorrelated snapshots, ES QM/MM MD simulations can then be carried out to take into account the vibrational relaxations on the ES PES. However, ab-initio calculations are suited for handling excited states (ES) dynamics, but they come with a great computational cost that severely hampers extensive sampling [44,45]. Moreover, due to the presence of high-frequency motions occurring during the relaxation of photo-excited systems, first principles ES MD simulations require extremely short integration time steps that limit the time scale that can be explored. This is due to the fact that molecule gains additional kinetic energy in the ES and returns vibrationally hot in the GS [45–47].

We here propose a good compromise that meets extended sampling and relatively inexpensive computational cost, defined within classical MD simulations. Since FF parameters can be tuned to better reproduce the physical behavior of any given system [48–50], the same algorithms that automate FF refinement in the GS can be used to fit classical potentials of molecular systems in their excited configurations [41,51]. Here, equilibrium distances and angles are taken according to reference structures whose electronic levels are set in the excited state of interest. The resulting FF is therefore constructed to mimic the dynamic behavior a the system constantly kept under excitation, thus allowing to collect a very large number of ES structures at the cost of a classical MD simulation.

Such a procedure has pros and cons. As stated above, the timescale associated with the non-radiative process (B in Fig. 1) allows the vibrational degrees of freedom of both solute and solvent to relax to the ES equilibrium geometry. Therefore, the sampling of ES geometry through classical MD simulations, which usually last nanoseconds (instead of picoseconds), may be questioned. However, it should be considered that each uncorrelated GS configuration undergoes the same process depicted in Fig. 1, with a different ES equilibrium geometry. Therefore, sampling the ES PES by means of a classical MD simulation, adequately reparametrized to the specific state of interest, is a pragmatic approach in which the relaxation process itself is avoided entirely, and justifiable due to Kasha's rule. Finally note that, within such a procedure, the sampling of the ES is only accurately treated if the selected level of theory correctly describes the state of interest.

It is worth remembering that all these refining techniques need to beforehand fix which degrees of freedom need to be refined. Among these degrees of freedom, non-bonded interactions are the most complex to refine since they are the resultant of many different interactions that in classical FFs are usually expressed as the summation of two contributions: Coulomb and van der Waals components [52]. In our modeling, by moving from GS to ES, we update Coulomb forces by setting atomic partial charges according to the selected electronic excited state, whereas van der Waals terms are kept frozen to those defining the GS, according to other approaches proposed in the literature [39]. Finally, it is worth mentioning that in this work we neglect to include quantum-mechanical vibronic effects in the modeling, which can affect the shape of the band. A full vibronic treatment could be done, however it would require geometry optimization on a large number of solute-solvent representative structures taken from the classical sampling, followed by full Hessian calculations for both GS and ES in order to obtain the normal vibrational modes and thus produce a vibronic bandshape for each structure. In this work, we instead keep the classical treatment of the nuclear degrees of freedom that emerges from the parametrized MD and use an empirical broadening factor for spectra.

### 2.2. QM/FQ + rep to account for Pauli Repulsion effects

As explained above, in order to describe solvent effects on both absorption and emission spectra, we exploit a fully polarizable QM/MM approach based on the FQ force field, which further accounts for Pauli repulsion effects on the QM density. In this approach, named QM/FQ + rep, the QM/MM interaction energy $E^{\text{int}}_{\text{QM/MM}}$ is decomposed as follows:

$$E^{\text{int}}_{\text{QM/MM}} = E^{\text{ele}}_{\text{QM/MM}} + E^{\text{pol}}_{\text{QM/MM}} + E^{\text{rep}}_{\text{QM/MM}} \quad (1)$$

where the electrostatic ($E^{\text{ele}}_{\text{QM/MM}}$), polarization ($E^{\text{pol}}_{\text{QM/MM}}$) and Pauli repulsion ($E^{\text{rep}}_{\text{QM/MM}}$) terms are defined. The electrostatic and polarization contributions are calculated by using the polarizable QM/FQ approach, where MM atoms are represented by means of the FQ force field [1,4,15]. This means that each atom of the MM portion is represented by a charge ($q$), which varies as a response to differences in atomic electronegativities and to the QM electrostatic potential. In this way, the FQs are polarized by the QM density, and they polarize back the QM density by entering the QM Hamiltonian, in a mutual polarization fashion.

Pauli Repulsion interactions are modeled by exploiting the approach proposed by some of the present authors [12]. A set of *s*-type gaussian functions is included on each MM molecule to mimic the presence of a

QM density in the MM portion ($\rho_{MM}$). In our model, $E^{rep}_{QM/MM}$ is written as the opposite of an exchange integral [12].

$$E^{rep}_{QM/MM} = \frac{1}{2}\int \frac{d\mathbf{r_1}d\mathbf{r_2}}{r_{12}}\rho_{QM}(\mathbf{r_1},\mathbf{r_2})\rho_{MM}(\mathbf{r_2},\mathbf{r_1}) \quad (2)$$

where the density $\rho_{MM}$ is defined as a combination of s-gaussian type functions which are localized in bond and lone pair regions. The explicit expression for $\rho_{MM}$ in the case of water can be found in Ref. 12. Note that $E^{rep}_{QM/MM}$ in Eq. (2) explicitly depends on the QM density $\rho_{QM}$, thus it enters the QM Hamiltonian, so that its effects propagate to properties and spectra [19]. QM/FQ + rep, when coupled with appropriate sampling of the solute-solvent phase-space, has been shown to provide a physically consistent modeling of several molecular properties and spectroscopies of aqueous solutions [13,14,19,53]

## 3. Experimental methods

Fluorescein disodium salt (Merck), Acridine Orange hydrochloride hydrate (Merck) were used without further purification. Basic violet 16 and basic yellow 40 were kindly provided by Gruppo Colle (Italy) and used as received. The water used to prepare the solutions was purified by a Millipore Milli-Q water purification system. In all cases fluorophore concentration of $3*10^{-6}$ M was studied. In the case of Fluorescein, a 0.1 M NaOH water solution was used as solvent [54]. Spectrophotometric measurements were carried out at 25 °C on a Cary 5000 UV–Vis–NIR spectrophotometer (Agilent), while fluorescence measurements were performed on a Horiba Jobin–Yvon Fluorolog-3 spectrofluorometer equipped with a 450 W Xenon arc lamp, double-grating excitation and single-grating emission monochromator. Quartz spectrophotometric cells with path length of 1 cm were used.

## 4. Computational Details

We test different sampling techniques on acetone. Despite its small size, acetone displays a huge Stokes shift and is characterized by large solvatochromic shift when moving from the gas-phase to aqueous solution [55–57]. For sampling the electronic GS when dissolved water, we perform three different MD runs, which are here summarized (more details are reported in Section S1 in the Electronic Supporting Information - ESI):

1. 20 ns classical MD simulation exploiting GAFF ($MD_{GAFF}$) [58]. The TIP3P force field was used to describe water molecules [59]. RESP charges are computed on the QM/PCM optimized ground state geometry at the CAM-B3LYP/aug-cc-pVDZ level.
2. Based on the $MD_{GAFF}$ run, an adiabatic QM/MM MD ($MD_{QM/MM}$) is performed. In particular, a snapshot with velocities calibrated at 300 K is extracted from $MD_{GAFF}$, which is then cut in a spherical shape centered on the acetone of radius 15 Å. The obtained droplet is partitioned into three layers: (i) QM layer (acetone); (ii) a first, mobile, MM layer including all water molecules within a radius of 10 Å from the solute, which are allowed to move during the QM/MM dynamics; (iii) a second, frozen MM layer, constituted by the remaining water molecules. The extracted droplet is first optimized at the CAM-B3LYP/aug-cc-pVDZ/TIP3P level. Then, a 20 ps QM/MM adiabatic run is performed, by treating the QM portion at the CAM-B3LYP/aug-cc-pVDZ level. $MD_{QM/MM}$ is performed by using the COBRAMM package [60].
3. Classical 20 ns MD simulation performed by exploiting a classical force field obtained by fitting calculated reference QM/PCM energies, gradients, and Hessian according to the JOYCE procedure ($MD_{REFINED}$). The TIP3P force field was used to describe water molecules [59]. RESP charges are computed on the QM/PCM optimized ground state and excited state geometry at the CAM-B3LYP/aug-cc-pVDZ level.

In order to sample the ES of acetone in aqueous solution, we perform a 20 ns classical MD simulation based on a fitted force field. In particular, we first define the classical force field by fitting calculated reference QM/PCM excited state energies, gradients, and Hessian by following the procedure implemented in JOYCE [41]. Also, in order to additionally improve the intramolecular potential defined by the dihedral angle $\delta$ reported in Fig. 2 (which mainly determines the emission spectrum, vide infra), we perform a refinement of such term by employing a genetic algorithm [61] (see also Section S2 in the ESI).

For acetone, we first focus on the calculation of vacuo-to-water solvatochromic shifts for both the absorption and the emission processes. To this end, the reference gas-phase vertical excitation/emission energies need to be computed. Here, we follow the strategy proposed in Ref. 62, i.e. we perform additional GS and ES MD runs of acetone in gas-phase. In particular, for the GS, we have exploited the three different GS MD simulations discussed above by removing the aqueous environment. Therefore, $MD_{QM/MM}$ in this case is actually an ab-initio MD simulation of acetone in gas-phase, whereas the JOYCE procedure is used to obtain a refined force field based on calculated gas-phase energies, gradients and Hessians for both the GS and ES $MD_{REFINED}$. From all MD runs, we then extract 200 uncorrelated snapshots (every 100 ps for $MD_{GAFF}$ and $MD_{REFINED}$; every 100 fs for $MD_{QM/MM}$), which are cut in spherical droplets with radius 15 Å centered on the solute.

The developed protocol is then applied to four selected fluorescent probes, namely Flurescein (F), Acridine orange (A), Basic violet 16 (V) and Basic yellow 40 (Y). The FF resulting from the JOYCE procedure is then used to run GS and ES 20 ns classical MD simulations (see also Section S1 in the Electronic Supplementary Information – ESI). For all chromophores, 200 snapshots are extracted (one every 100 ps), and cut in a spherical shape centered on the solute with radius 20 Å.

Polarizable QM/FQ + rep TD-DFT calculations are then performed on all extracted snapshots. In all cases, acetone constitutes the QM part, whereas water molecules are described by means of the polarizable FQ FF, by exploiting the parametrization proposed in Ref. 13. Pauli repulsion effects are included by means of the model proposed in Ref. 12. Finally, absorption/emission energies of each snapshot are calculated at the CAM-B3LYP/aug-cc-pVDZ/FQ + rep level, and averaged with a Gaussian band shape (full width at half maximum = 0.25 eV) to obtain the final spectra. The emission intensities are proportional to $D\omega^3$ where $\omega$ is the frequency of the transition and $D$ is the emission dipole strength. This expression matches the reported experimental observable.

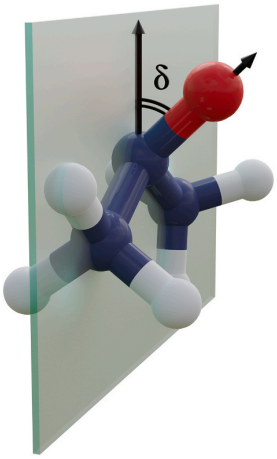


**Fig. 2.** Graphical depiction of acetone improper dihedral angle $\delta$.

## 5. Results and discussion

### 5.1. Acetone in aqueous solution

We first discuss the absorption properties of acetone as dissolved in aqueous solution. In particular, as stated above, we focused on the dark transition $n \rightarrow \pi^*$, because it exhibits a relatively large vacuo-to-water solvatochromic shift [55–57]. As stated above, the GS solute-solvent phase space is sampled by using three different MD runs, namely $MD_{GAFF}$, $MD_{REFINED}$ and $MD_{QM/MM}$. Absorption spectra computed for 200 uncorrelated snapshots extracted from each MD run are graphically depicted in Fig. 3, where raw absorption data are shown as stick spectra.

From the inspection of Fig. 3, the role of the dynamical nature of the solvation phenomenon, which is responsible for the inhomogeneous band broadening of the final averaged spectrum, is evident. In fact, there is large variability both in the excitation energy values and oscillator strengths as a function of the extracted snapshot. Although broadening is observed for all MD simulations, it is particularly accentuated for $MD_{GAFF}$, both with and without the inclusion of QM/MM Pauli repulsion. For both $MD_{REFINED}$ and $MD_{QM/MM}$ simulations, instead, the inclusion of quantum confinement effects lead to a shrinking of the computed $n \rightarrow \pi^*$ band. Also, for these two MDs, the description of repulsion effects yields a significant shift of the computed excitation energy of about 0.12–0.14 eV. For both MDs, an almost perfect agreement with the experimental spectrum is reported (see Fig. 3), whereas for $MD_{GAFF}$, a discrepancy of 0.29 (QM/FQ) and 0.32 (QM/FQ + rep) eV is obtained.

To deeply understand the differences between MD simulations, the potential of mean force (PMF) as a function of $\delta$ dihedral distribution function is computed (see Fig. 2) for $MD_{GAFF}$, $MD_{REFINED}$ and $MD_{QM/MM}$ and further compared to the QM/PCM scan, on which the FF used in $MD_{REFINED}$ has been parametrized (see Fig. 4a). While the distributions by $MD_{REFINED}$ and $MD_{QM/MM}$ almost perfectly resemble the QM/PCM curve, $MD_{GAFF}$ predicts a very flat curve. In fact, by exploiting GAFF parameters, high energy structures can be sampled, consequently affecting $n \rightarrow \pi^\star$ transition energies. To quantify the effects of such a distribution on both excitation energies and oscillator strengths, in Fig. 4b excitation energies computed for all 200 uncorrelated snapshots as a function of $\delta$ are plotted and colored depending on oscillator strengths. While $MD_{REFINED}$ and $MD_{QM/MM}$ report almost the same, very localized, distribution, for $MD_{GAFF}$ a larger spread is predicted, thus justifying also the larger inhomogeneous broadening reported in Fig. 3.

To further analyze computed results, in Fig. 5 we report the vacuo-to-water absorption solvatochromic shifts for the three different MD samplings, both in the gas-phase and in aqueous solution (see also Computational Details section). By comparing energy differences such as vacuum-to-water shifts, systematic errors associated with a specific choice of functional/basis set are reduced [37], thus allowing for a

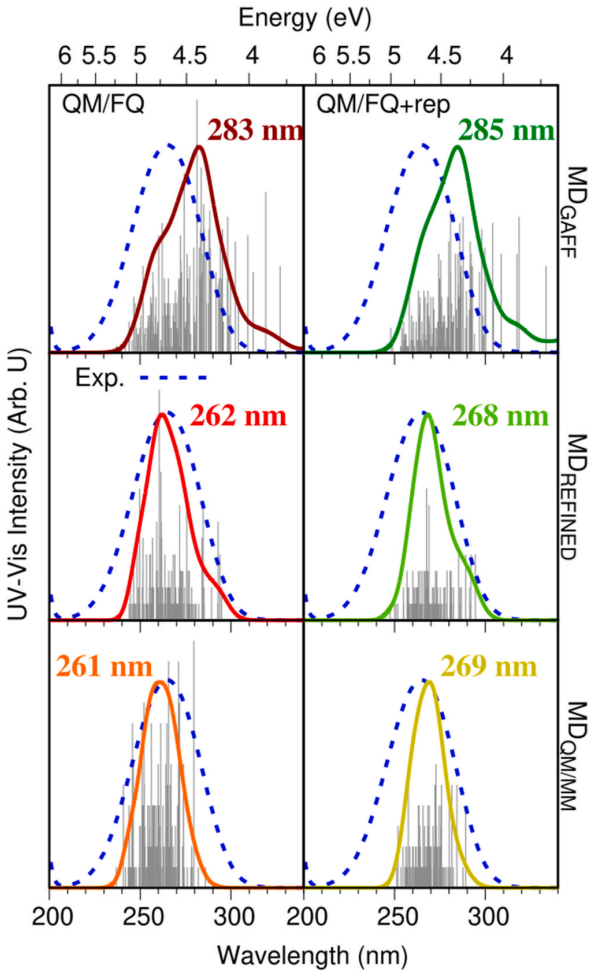


**Fig. 3.** Acetone QM/FQ (left) and QM/FQ + rep (right) absorption raw data (sticks) and convoluted spectra (FWHM = 0.25 eV, solid line) as obtained from $MD_{GAFF}$, $MD_{REFINED}$ and $MD_{QM/MM}$ calculations. The experimentally measured experimental absorption spectrum is also reported as a blue dashed line.

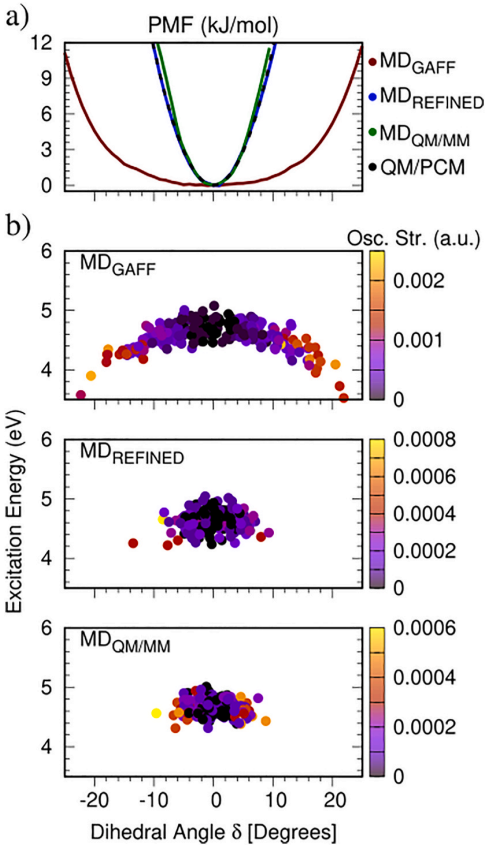


**Fig. 4.** (a) QM/PCM, $MD_{GAFF}$, $MD_{REFINED}$ and $MD_{GAFF}$ Acetone GS Potential of Mean Force (kJ/mol). (b) Excitation energies and oscillator strengths as a function of acetone improper dihedral angle $\delta$.

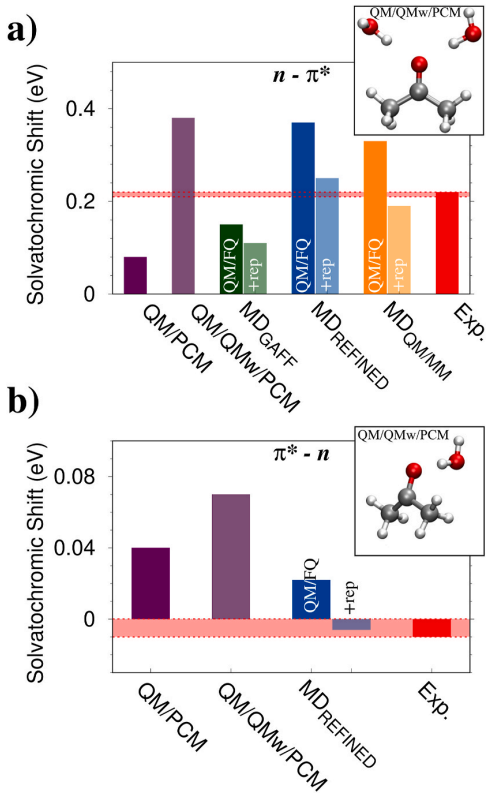


**Fig. 5.** Acetone QM/FQ and QM/FQ + rep absorption (a) and emission (b) solvatochromic shifts as computed from $MD_{GAFF}$, $MD_{REFINED}$ and $MD_{QM/MM}$ runs. The experimental reference value, together with its uncertainty, is graphically depicted in red.

better comparison with experimental data. As it can be noticed, while QM/FQ and QM/FQ + rep results obtained by exploiting the $MD_{GAFF}$ trajectory consistently underestimate the experimental value, $MD_{REFINED}$ and $MD_{QM/MM}$ QM/FQ + rep shifts are in almost perfect agreement (discrepancy of ~ 0.3 eV) with experiments. QM/MM results can also be compared with an implicit description of the solvent (QM/PCM), which underestimates the absorption shift probably due to the lack of the description of specific HB interactions. The implicit description can be refined by including two hydrogen-bonded water molecules in the QM region (QM/QMw/PCM, see Fig. 5a).However, also in this case, an overestimated shift is reported, which is most likely due to neglecting the dynamical nature of the solvation. In particular, Fig. 5a clearly shows the role of correctly including electrostatics (+polarization), quantum confinement effects, and dynamical effects in the prediction of absorption solvatochromic shifts, remarkably in line with previous studies of some of us [14,19].

We now move to fluorescence. As explained above, to sample the solute-solvent phase-space in the excited state, we resort to a classical MD simulation based on a force field adequately refined to reproduce ES energies, gradients and Hessian, together with a correct accounting for changes in the electronic density. From the resulting $MD_{REFINED}$ simulation, 200 uncorrelated snapshots are extracted, and fluorescence spectra are simulated by exploiting both QM/FQ and QM/FQ + rep, by also including cLR corrections [38], which may particularly affect the molecular response of the excited state. Both QM/FQ and QM/FQ + rep cLR raw spectra associated to the $\pi^* \rightarrow n$ transition are graphically depicted in Fig. 6, together with their gaussian convolution. Differently from absorption, repulsive interactions only slightly affect the averaged

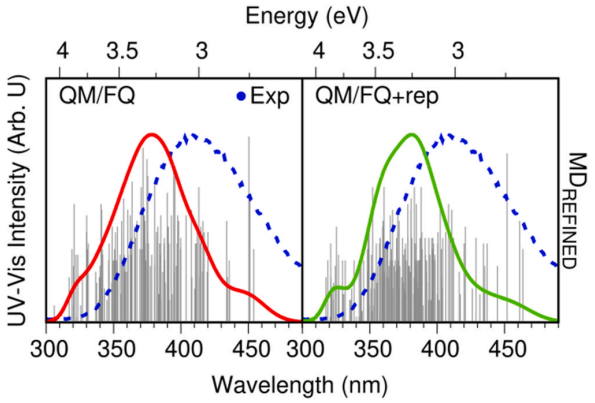


**Fig. 6.** Acetone QM/FQ (red, left) and QM/FQ + rep (green, right) emission raw data (sticks) together with their Gaussian convolution (solid lines, FWHM = 0.25 eV). Snapshots are extracted from $MD_{REFINED}$. The experimental spectrum is also reported as a blue dashed line.

emission energy, thus yielding an emission solvatochromic shift of about ~ −0.01 eV, which is in very good agreement with the experimental shift (see Fig. 5b and Tabs. S2–S3 in the ESI). This is related to the larger number of hydrogen-bonded solvent molecules, and the resulting shorter HB distance which are predicted for the GS, as compared to ES (see Fig. S2 in the ESI). Indeed, QM/FQ + rep is the only method that can reproduce the experimental negative solvatochromic shift, while QM/FQ yields a positive shift. Also both implicit QM/PCM and cluster QM/QMw/PCM models (the latter constructed by including a single water molecule in the QM region) overestimate the emission solvatochromic shift, most likely due to neglecting dynamical solvent effects and the lack of specific interactions in QM/PCM calculations.

In Fig. 6, the measured experimental spectrum is also graphically depicted. In this case, a small shift (~ 0.25 eV) between computed and experimental peaks is reported. However, computed and experimental solvatochromic shifts (~ −0.01 eV) are in perfect agreement, thus demonstrating the robustness of our approach (see Fig. 5b and Tabs. S2–S3 in the ESI). We also note that QM/FQ and QM/FQ + rep do not provide the same spreading in energies and intensities as a function of the snapshot, thus resulting in a different description of the band inhomogeneous broadening, from which a sharper emission peak is described by QM/FQ + rep.

To further analyze computed data, in Fig. 7a we report the ES PMF as a function of the dihedral angle $\delta$ (see Fig. 2). The most relevant change with respect to the GS equilibrium geometry is the pyrimidalization of the C═O group. In fact, the acetone ES is characterized by a distorted geometry with $\delta \sim 20°$. This deformation drastically affects the electronic structure of the molecule, and is therefore crucial to correctly describe ES properties. Fig. 7 clearly shows the almost perfect reproduction of $\delta$-PMF by $MD_{REFINED}$. It is worth noting that such a good agreement could not be obtained by exploiting the JOYCE procedure (see Fig. S1 in the ESI). In Fig. 7b, the dependence of emission energy on $\delta$ is reported; clearly, the large $\delta$ variability strongly affects emission energies and the oscillator strengths for both QM/FQ and QM/FQ + rep approaches. However, the distribution of both excitation energies and oscillator strengths are similar for the two methods, showing that, in this case, repulsive contributions do not largely affect the molecular response.

We finally move to compare computed and experimental Stokes shift (emission - absorption energies), see Fig. 8. As a result of the reliable sampling reproduced by $MD_{REFINED}$, the computed Stokes shift is in good agreement with its experimental counterpart, with an error of about 17%. Indeed, our value is particularly impressive considering the almost perfect agreement with the results reported in Refs. 63 and 64, which

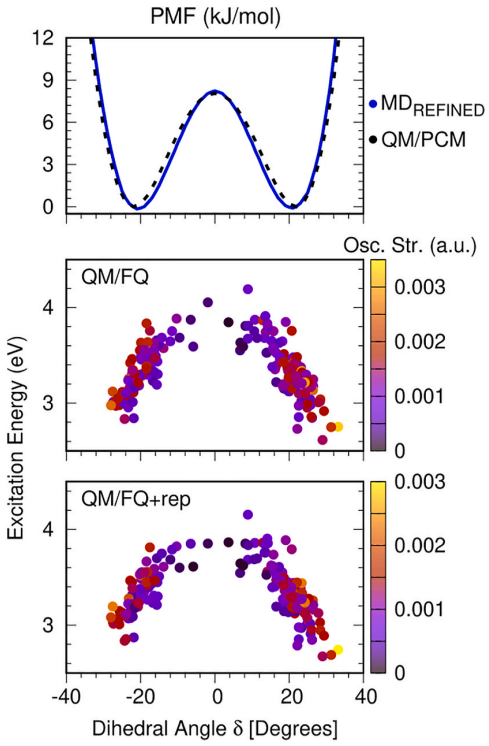


**Fig. 7.** (a) QM/PCM and $MD_{REFINED}$ Acetone ES Potential of Mean Force (kJ/mol). (b) Emission energy and oscillator strength as a function of the improper dihedral angle $\delta$.

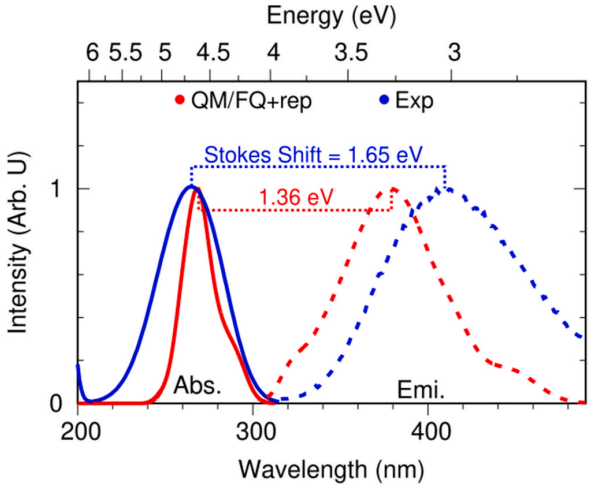


**Fig. 8.** Comparison between computed QM/FQ + rep (red, based on $MD_{REFINED}$) and experimental (blue) absorption (solid lines) and emission (dashed lines) spectra of acetone. Computed (red) and experimental (blue) Stokes Shifts are also highlighted.

have been obtained by exploiting much more computationally demanding QM/MM MD simulations for both GS and ES. This is probably due to the near perfect match between the QM scan and $MD_{REFINED}$ PMFs. Such findings demonstrate once again the robustness of our approach, which can yield results qualitatively and quantitatively in agreement with higher level calculations, however at much lower computational cost.

## 6. Fluorescent dyes

By properly parametrizing classical FFs for both GS and ES, we have been able to collect a statistically relevant set of configurations, successfully used to compute acetone absorption and emission energies by means of the polarizable QM/FQ + rep approach. Hence, we extend the approach to four more challenging chemically fluorescent dyes (Fig. 9), namely fluorescein (F) [65,66], basic violet 16 (V) [67], basic yellow 40 (Y) [68], and acridine orange (A) [69,70]. Such molecules have been chosen because they are commercially available and are used for a plethora of applications, such as fluorescence markers for biological matrices, surgical cancer imaging and therapy [71], textiles [72] and dopants in photovoltaic applications [73,74].

In order to accurately predict absorption and fluorescence spectra of the four dyes in aqueous solution, two classical MDs are performed to adequately sample the GS and the ES. We first optimize molecular structures in the GS and the first singlet ES (S1), by modeling solvent effects by means of the implicit PCM approach. In all cases, the first electronic excitation is characterized by a bright, pure HOMO-LUMO transition, with $\pi - \pi^*$ nature. The involved molecular orbitals (MOs) are graphically depicted in Fig. S3 in the ESI.

Optimized GS and ES geometries are graphically superimposed in Fig. S4 in the ESI. Differently from acetone, the superposition between S0 and S1 optimized geometries is almost perfect. Thus, in this case, the S1 minimum geometry is not characterized by floppy dihedral angles, as for acetone $\delta$ angle. For this reason, the re-parametrization of the FF is performed through QM/PCM calculations according to the JOYCE scheme for both S0 and S1 states of each dye, without any further refining process.

To analyze GS and ES MD simulations, in Fig. S5 in the ESI. the radial distribution functions (RDF, $g(r)$) are depicted for the main Hydrogen acceptor and donor groups of each system. We first note that hydrogen bonding (HB) interactions with the water molecules are not present in case of **V**, that in contrast with **F**, **Y** and **A**. This applies to both GS and ES simulations, which are indeed almost identical as a result of the similarity in GS and ES geometries. Among the studied dyes, **F** displays the highest number of HBs with the solvent, provided by the carboxylic and the two carbonyl groups, both acting as HB acceptor groups. Similarly, **Y**

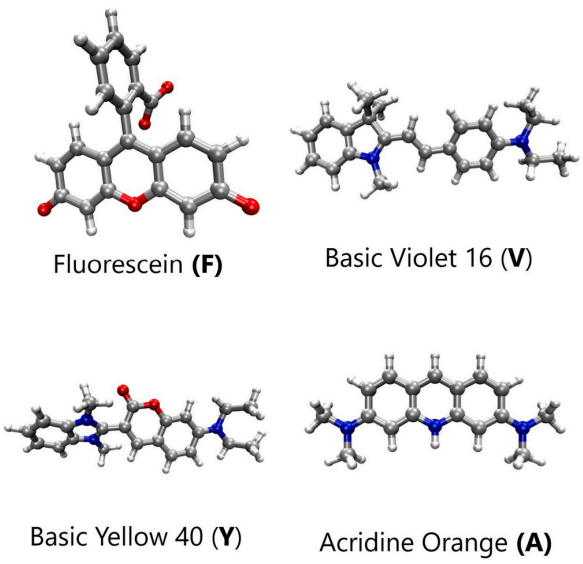


**Fig. 9.** Molecular structures of the four investigated fluorophores.

acts as HB acceptor (via O2, see Fig. S5 in the ESI). On the other hand, **A** is the only dye which acts as HB donor via the hydrogen atom of the amino group. Thus, the selected dyes are characterized by a large variety of different interactions with the external environment, thus being ideal candidates to demonstrate the versatility of our computational protocol.

We finally move to the comparison between calculated and experimental absorption and emission spectra, which are graphically depicted in Fig. 10. Calculated spectra are obtained at the most sophisticated level of theory (i.e. QM/FQ + rep) by averaging on 200 uncorrelated snapshots extracted from GS and ES MD runs. We first note that computed absorption/emission transition energies are blueshifted with respect to experimental data. This is probably due to a systematic error introduced by the particular choice of density functional/basis set exploited in this work. As stated above, to reduce such systematic errors, energy differences need to be considered. In this case, we therefore analyze Stokes shifts, which are also reported in Fig. 10. Computed Stokes shifts range between 0.11 (F) and 0.30 (Y), and are significantly smaller than that predicted for acetone $n \rightarrow \pi^*$ transition. This is a direct consequence of the similarity between GS and ES optimized geometries. The comparison with measured shifts clearly depicts an almost perfect agreement with our calculated data, with the largest discrepancy displayed by **V**. However, in this case the computed error is of about 0.04 eV, which is comparable to the chemical accuracy (1 kcal/mol). Therefore, the reported results clearly demonstrate the reliability and robustness of our computational approach.

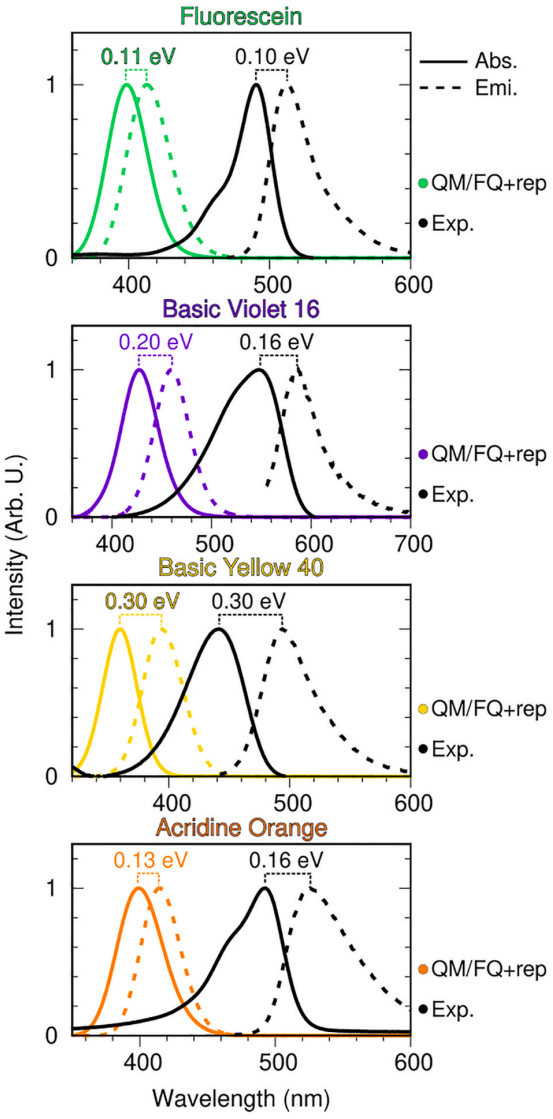


**Fig. 10.** Comparison between computed QM/FQ + rep (colored line) and experimental (black line) absorption (solid line) and emission (dashed line) spectra of the four studied dyes. Computed (colored) and experimental (black) Stokes Shifts are also indicated.

## 7. Summary and conclusions

We have presented a synergistic experimental/computational study of emission properties of molecular systems in aqueous solution. To accurately model ES-related properties, we propose a novel cost-effective computational protocol, which can potentially bridge a gap in fully atomistic approaches to molecular spectroscopy of solvated systems. In fact, the method conceptually involves two main steps: a pragmatic approach to obtain an accurate sampling of the molecule-environment phase space with the molecule in its excited state, followed by QM/MM modeling of its emission properties, that fully takes molecule-environment interactions into consideration.

The first step of the protocol involves the sampling of the configuration space, based on a re-parametrization of classical FFs based on ES QM reference data, such as energies, gradients and Hessian. Changes in the electronic density are also taken into account by employing atomic charges based on the ES QM calculations. The resulting FF that combines these two ingredients, possibly together with a refinement of flexible dihedral angles in the ES, is able to correctly sample the molecule in its ES. Subsequently, the model employs state-of-the-art quantum-mechanical simulations, describing the aqueous environment through a polarizable QM/MM method based on Fluctuating Charges, with the additional inclusion of Pauli repulsion effects. The developed protocol has been firstly tested against the reproduction of the absorption and emission spectral features of acetone in aqueous solution which, despite its small size, is particularly challenging due to the pyramidalization of the C═O group in the first ES. Our method not only provides an almost perfect agreement with our measured experimental data, but also with more sophisticated, and much more computationally demanding, approaches. To further demonstrate the applicability of the approach, we have studied four fluorescent dyes, which are characterized by a large variety of interactions with the aqueous environment. Also in this case, the proper sampling of the GS/ES, together with the correct description of the main physico-chemical interactions in aqueous solution by means of the QM/FQ + rep method, is able to accurately reproduce the main experimental spectral features.

Remarkably, the proposed methodology is not limited to the peculiar case of aqueous solutions, but paves the way to a reliable description of ES properties of target systems embedded in generic environments, including biological matrices and surfaces, at reasonably low computational cost.

## CRediT authorship contribution statement

**Sulejman Skoko:** Formal analysis, and, Investigation, calculations, Writing – original draft. **Cosimo Micheletti:** Formal analysis, and, Investigation, experimental spectra. **Emanuele Grifoni:** Formal analysis, and, Investigation, MD, Writing – original draft. **Franco Egidi:** Computational, Methodology, Software, Writing – review & editing. **Tommaso Giovannini:** Computational, Methodology, Software, Writing – review & editing. **Andrea Pucci:** Experimental, Methodology, Writing – review & editing, Supervision. **Chiara Cappelli:** Conceptualization, computational, Methodology, Writing – review & editing, Supervision, and, Project administration, All authors have given approval to the final version of the manuscript.

## Declaration of competing interest

The authors declare that they have no known competing financial interests or personal relationships that could have appeared to influence the work reported in this paper.

## Data availability

Data will be made available on request.

## Acknowledgements

This work has received funding from Ministero dell'Università e della Ricerca (MUR) under the FARE 2020 (MORE-Plasmon-R20YTA2BKZ) project. We gratefully acknowledge the Center for High Performance Computing (CHPC) at SNS for providing the computational infrastructure.

## Appendix A. Supplementary data

Supplementary data to this article can be found online at https://doi.org/10.1016/j.dyepig.2023.111227.

## References

[1] Giovannini T, Egidi F, Cappelli C. Molecular spectroscopy of aqueous solutions: a theoretical perspective. Chem Soc Rev 2020;49(16):5664–77.
[2] Sisto A, Stross C, van der Kamp MW, O'Connor M, McIntosh-Smith S, Johnson GT, et al. Atomistic non-adiabatic dynamics of the LH2 complex with a gpu-accelerated ab initio exciton model. Phys Chem Chem Phys 2017;19(23):14924–36.
[3] Olsen JMH, Kongsted J. Molecular properties through polarizable embedding. Adv Quant Chem 2011;61:107–43.
[4] Cappelli C. Integrated QM/polarizable MM/continuum approaches to model chiroptical properties of strongly interacting solute-solvent systems. Int J Quant Chem 2016;116(21):1532–42.
[5] Warshel A, Levitt M. Theoretical studies of enzymic reactions: dielectric, electrostatic and steric stabilization of the carbonium ion in the reaction of lysozyme. J Mol Biol 1976;103(2):227–49.
[6] Senn HM, Thiel W. QM/MM methods for biomolecular systems. Angew Chem Int Ed 2009;48(7):1198–229.
[7] Boulanger E, Thiel W. Solvent boundary potentials for hybrid QM/MM computations using classical drude oscillators: a fully polarizable model. J Chem Theor Comput 2012;8(11):4527–38.
[8] Bondanza M, Nottoli M, Cupellini L, Lipparini F, Mennucci B. Polarizable embedding QM/MM: the future gold standard for complex (bio) systems? Phys Chem Chem Phys 2020;22(26):14433–48.
[9] Olsen JM, Aidas K, Kongsted J. Excited states in solution through polarizable embedding. J Chem Theor Comput 2010;6(12):3721–34.
[10] Olsen JMH, Steinmann C, Ruud K, Kongsted J. Polarizable density embedding: a new QM/QM/MM-based computational strategy. J Phys Chem A 2015;119(21):5344–55.
[11] Curutchet C, Muñoz-Losa A, Monti S, Kongsted J, Scholes GD, Mennucci B. Electronic energy transfer in condensed phase studied by a polarizable QM/MM model. J Chem Theor Comput 2009;5(7):1838–48.
[12] Giovannini T, Lafiosca P, Cappelli C. A general route to include pauli repulsion and quantum dispersion effects in QM/MM approaches. J Chem Theor Comput 2017;13(10):4854–70.
[13] Giovannini T, Lafiosca P, Chandramouli B, Barone V, Cappelli C. Effective yet reliable computation of hyperfine coupling constants in solution by a QM/MM approach: interplay between electrostatics and non-electrostatic effects. J Chem Phys 2019;150:124102.
[14] Marrazzini G, Giovannini T, Egidi F, Cappelli C. Calculation of linear and non-linear electric response properties of systems in aqueous solution: a polarizable quantum/classical approach with quantum repulsion effects. J Chem Theor Comput 2020;16(11):6993–7004.
[15] Giovannini T, Egidi F, Cappelli C. Theory and algorithms for chiroptical properties and spectroscopies of aqueous systems. Phys Chem Chem Phys 2020;22:22864–79.
[16] Carnimeo I, Cappelli C, Barone V. Analytical gradients for MP2, double hybrid functionals, and TD-DFT with polarizable embedding described by fluctuating charges. J Comput Chem 2015;36(31):2271–90.
[17] Caricato M, Lipparini F, Scalmani G, Cappelli C, Barone V. Vertical electronic excitations in solution with the EOM-CCSD method combined with a polarizable explicit/implicit solvent model. J Chem Theor Comput 2013;9(7):3035–42.
[18] Ambrosetti M, Skoko S, Giovannini T, Cappelli C. Quantum mechanics/fluctuating charge protocol to compute solvatochromic shifts. J Chem Theor Comput 2021;17(11):7146–56.
[19] Giovannini T, Ambrosetti M, Cappelli C. Quantum confinement effects on solvatochromic shifts of molecular solutes. J Phys Chem Lett 2019;10(19):5823–9.
[20] Lakowicz JR. Principles of fluorescence spectroscopy. Springer; 2006.
[21] Demchenko AP. Introduction to fluorescence sensing. Springer Science & Business Media; 2008.
[22] Valeur B, Berberan-Santos MN. Molecular fluorescence: principles and applications. John Wiley & Sons; 2012.
[23] Mennucci B. Modeling absorption and fluorescence solvatochromism with QM/classical approaches. Int J Quant Chem 2015;115(18):1202–8.
[24] Toulouse J, Colonna Fmc, Savin A. Long-range–short-range separation of the electron-electron interaction in density-functional theory. Phys Rev A 2004;70:062505. URL: https://link.aps.org/doi/10.1103/PhysRevA.70.062505. 10.1103/PhysRevA.70.062505.
[25] Kjellgren ER, Haugaard Olsen JM, Kongsted J. Importance of accurate structures for quantum chemistry embedding methods: which strategy is better? J Chem Theor Comput 2018;14(8):4309–19.
[26] Gómez S, Giovannini T, Cappelli C. Absorption spectra of xanthines in aqueous solution: a computational study. Phys Chem Chem Phys 2020;22(10):5929–41.
[27] Skoko S, Ambrosetti M, Giovannini T, Cappelli C. Simulating absorption spectra of flavonoids in aqueous solution: a polarizable QM/MM study. Molecules 2020;25(24):5853.
[28] Debnath J, Invernizzi M, Parrinello M. Enhanced sampling of transition states. J Chem Theor Comput 2019;15(4):2454–9.
[29] Trizio E, Parrinello M. From enhanced sampling to reaction profiles. J Phys Chem Lett 2021;12(35):8621–6.
[30] Bussi G, Laio A. Using metadynamics to explore complex free-energy landscapes. Nat Rev Phys 2020;2(4):200–12.
[31] Laio A, Gervasio FL. Metadynamics: a method to simulate rare events and reconstruct the free energy in biophysics, chemistry and material science. Rep Prog Phys 2008;71(12):126601.
[32] Laio A, Parrinello M. Escaping free-energy minima. P Natl Acad Sci 2002;99(20):12562–6.
[33] Crespo-Otero R, Barbatti M. Spectrum simulation and decomposition with nuclear ensemble: formal derivation and application to benzene, furan and 2-phenylfuran. In: Marco antonio chaer nascimento. Springer; 2014. p. 89–102.
[34] Barbatti M, Sen K. Effects of different initial condition samplings on photodynamics and spectrum of pyrrole. Int J Quant Chem 2016;116(10):762–71.
[35] Tomasi J, Mennucci B, Cammi R. Quantum mechanical continuum solvation models. Chem Rev 2005;105(8):2999–3094.
[36] Caricato M, Mennucci B, Tomasi J, Ingrosso F, Cammi R, Corni S, Scalmani G. Formation and relaxation of excited states in solution: a new time dependent polarizable continuum model based on time dependent density functional theory. J Chem Phys 2006;124(12):124520.
[37] Loco D, Polack É, Caprasecca S, Lagardere L, Lipparini F, Piquemal JP, et al. A QM/MM approach using the amoeba polarizable embedding: from ground state energies to electronic excitations. J Chem Theor Comput 2016;12(8):3654–61.
[38] Giovannini T, Riso RR, Ambrosetti M, Puglisi A, Cappelli C. Electronic transitions for a fully polarizable QM/MM approach based on fluctuating charges and fluctuating dipoles: linear and corrected linear response regimes. J Chem Phys 2019;151(17):174104.
[39] Loco D, Gelfand N, Jurinovich S, Protti S, Mezzetti A, Mennucci B. Polarizable qm/classical approaches for the modeling of solvation effects on uv–vis and fluorescence spectra: an integrated strategy. J Phys Chem A 2018;122(1):390–7.
[40] Giovannini T, Del Frate G, Lafiosca P, Cappelli C. Effective computational route towards vibrational optical activity spectra of chiral molecules in aqueous solution. Phys Chem Chem Phys 2018;20:9181–97.
[41] Barone V, Cacelli I, De Mitri N, Licari D, Monti S, Prampolini G. Joyce and Ulysses: integrated and user-friendly tools for the parameterization of intramolecular force fields from quantum mechanical data. Phys Chem Chem Phys 2013;15(11):3736–51.
[42] Campetella M, De Mitri N, Prampolini G. Automated parameterization of quantum-mechanically derived force-fields including explicit sigma holes: a pathway to energetic and structural features of halogen bonds in gas and condensed phase. J Chem Phys 2020;153(4):044106.
[43] Vilhena J, Greff da Silveira L, Livotto PR, Cacelli I, Prampolini G. Automated parameterization of quantum mechanically derived force fields for soft materials and complex fluids: development and validation. J Chem Theor Comput 2021;17(7):4449–64.
[44] Westermayr J, Marquetand P. Machine learning and excited-state molecular dynamics. Mach Learn: Sci Technol 2020;1(4):043001.
[45] Nelson TR, White AJ, Bjorgaard JA, Sifain AE, Zhang Y, Nebgen B, Fernandez-Alberti S, Mozyrsky D, Roitberg AE, Tretiak S. Non-adiabatic excited-state molecular dynamics: theory and applications for modeling photophysics in extended molecular materials. Chem Rev 2020;120(4):2215–87.
[46] Weingart O. Combined quantum and molecular mechanics (QM/MM) approaches to simulate ultrafast photodynamics in biological systems. Curr Org Chem 2017;21(7):586–601.
[47] Weingart O, Nenov A, Altoè P, Rivalta I, Segarra-Martí J, Dokukina I, Garavelli M. Cobramm 2.0—a software interface for tailoring molecular electronic structure calculations and running nanoscale (qm/mm) simulations. J Mol Model 2018;24(9):1–30.
[48] Hopfinger AJ, Pearlstein RA. Molecular mechanics force-field parameterization procedures. J Comput Chem 1984;5:486–99. URL: https://onlinelibrary.wiley.com/doi/10.1002/jcc.540050510. 10.1002/jcc.540050510.
[49] Cole DJ, Mones L, Csányi G. A machine learning based intramolecular potential for a flexible organic molecule. Faraday Discuss 2020;224:247–64. URL: http://xlink.rsc.org/?DOI=D0FD00028K. 10.1039/D0FD00028K.

[50] Mayne CG, Saam J, Schulten K, Tajkhorshid E, Gumbart JC. Rapid parameterization of small molecules using the force field toolkit. J Comput Chem 2013;34:2757–70. URL: https://onlinelibrary.wiley.com/doi/10.1002/jcc.23422. 10.1002/jcc.23422.
[51] Barone V, Bloino J, Monti S, Pedone A, Prampolini G. Fluorescence spectra of organic dyes in solution: a time dependent multilevel approach. Phys Chem Chem Phys 2011;13(6):2160–6.
[52] Wang J, Wolf RM, Caldwell JW, Kollman PA, Case DA. Development and testing of a general amber force field. J Comput Chem 2004;25(9):1157–74.
[53] Gomez S, Giovannini T, Cappelli C. Multiple facets of modeling electronic absorption spectra of systems in solution. ACS Phys Chem Au 2023;3(1):1–16.
[54] Umberger JQ, LaMer VK. The kinetics of diffusion controlled molecular and ionic reactions in solution as determined by measurements of the quenching of fluorescence. J Am Chem Soc 1945;67(7):1099–109.
[55] Aidas K, Mikkelsen KV, Mennucci B, Kongsted J. Fluorescence and phosphorescence of acetone in neat liquid and aqueous solution studied by qm/mm and pcm approaches. Int J Quant Chem 2011;111(7–8):1511–20.
[56] Catalán J, Catalán JP. On the solvatochromism of the n-$\pi^*$ electronic transitions in ketones. Phys Chem Chem Phys 2011;13(9):4072–82.
[57] Renge I. Solvent dependence of n-$\pi^*$ absorption in acetone. J Phys Chem 2009;113 (40):10678–86.
[58] Wang J, Wolf RM, Caldwell JW, Kollman PA, Case DA. Development and testing of a general amber force field. J Comput Chem 2004;25(9):1157–74. https://doi.org/10.1002/jcc.20035. 10.1002/jcc.20035.
[59] Mark P, Nilsson L. Structure and dynamics of the tip3p, spc, and spc/e water models at 298 k. J Phys Chem A 2001;105(43):9954–60.
[60] Mai S, Mohamadzade A, Marquetand P, González L, Ullrich S. Simulated and experimental time-resolved photoelectron spectra of the intersystem crossing dynamics in 2-thiouracil. Molecules 2018;23(11):2836.
[61] Kramer O. Genetic algorithms. Cham: Springer International Publishing; 2017, ISBN 978-3-319-52156-5. p. 11–9. https://doi.org/10.1007/978-3-319-52156-5_2. 10.1007/978-3-319-52156-5_2.
[62] Marenich AV, Cramer CJ, Truhlar DG. Electronic absorption spectra and solvatochromic shifts by the vertical excitation model: solvated clusters and molecular dynamics sampling. J Phys Chem B 2015;119(3):958–67.
[63] Ma H, Ma Y. Solvent effect on electronic absorption, fluorescence, and phosphorescence of acetone in water: revisited by quantum mechanics/molecular mechanics (QM/MM) simulations. J Chem Phys 2013;138(22):224505.
[64] Öhrn A, Karlström G. Hybrid Monte Carlo simulations of vertical electronic transitions in acetone in aqueous solution. Theor Chem Acc 2007;117(3):441–9.
[65] Sjöback R, Nygren J, Kubista M. Absorption and fluorescence properties of fluorescein. Spectrochim Acta 1995;51(6):L7–21.
[66] Klonis N, Sawyer WH. Spectral properties of the prototropic forms of fluorescein in aqueous solution. J Fluoresc 1996;6(3):147–57.
[67] Rashidian M, Dorranian D, Darani SA, Saghafi S, Ghoranneviss M. Nonlinear responses and optical limiting behavior of basic violet 16 dye under cw laser illumination. Optik 2009;120(18):1000–6.
[68] Nassar MM. Intraparticle diffusion of basic red and basic yellow dyes on palm fruit bunch. Water Sci Technol 1999;40(7):133–9.
[69] Hayashi M, Sofuni T, Ishidate Jr M. An application of acridine orange fluorescent staining to the micronucleus test. Mutat Res Lett 1983;120(4):241–7.
[70] Tejada RI, Mitchell JC, Norman A, Marik JJ, Friedman S. A test for the practical evaluation of male fertility by acridine orange (ao) fluorescence. Fertil Steril 1984; 42(1):87–91.
[71] Byvaltsev VA, Bardonova LA, Onaka NR, Polkin RA, Ochkal SV, Shepelev VV, Aliyev MA, Potapov AA. Acridine orange: a review of novel applications for surgical cancer imaging and therapy. Front Oncol 2019;9:925.
[72] Clark M. Handbook of textile and industrial dyeing: principles, processes and types of dyes. Elsevier; 2011.
[73] Kazim S, Zulfequar M, Haq MM, Bhatnagar P, Husain M. Electrical and optical properties of thin films based on poly [2-methoxy-5 (2'-ethyl hexyloxy)-1, 4-phenylene vinylene] doped with acridine orange dye with possible photovoltaic applications. Sol Energy Mater Sol Cell 2007;91(15–16):1462–6.
[74] Minei P, Iasilli G, Ruggeri G, Pucci A. Luminescent solar concentrators from waterborne polymer coatings. Coatings 2020;10(7):655.

# Electronic Supporting Information - Towards a Cost-Effective Modeling of Fluorescence in the Condensed Phase

Sulejman Skoko,[†] Cosimo Micheletti,[‡] Emanuele Grifoni,[†] Franco Egidi,[†] Tommaso Giovannini,[†] Andrea Pucci,[‡] and Chiara Cappelli*[,†]

†*Scuola Normale Superiore, Piazza dei Cavalieri 7, 56126 Pisa, Italy.*

‡*Dipartimento di Chimica e Chimica Industriale, Università di Pisa, Via G. Moruzzi 13, 56124 Pisa, Italy.*

E-mail: chiara.cappelli@sns.it

## Contents

**S1 Computational Details** **S2**

**S2 Genetic Algorithm Procedure** **S2**

**S3 Acetone in aqueous solution** **S5**

**S4 Dyes in aqueous solution** **S7**

**References** **S9**

# S1 Computational Details

All classical Ground and Excited State MD simulations ($MD_{GAFF}$ and $MD_{REFINED}$, see main text) were performed by following the same computational protocol. First, RESP charges were computed at the optimized ground state and optimized S1 state by employing CAM-B3LYP/aug-cc-pVDZ at PCM level. Electrostatic interactions were treated by using particle-mesh Ewald (PME) method with a grid spacing of 0.16 Å and a spline interpolation of order 4.[1] The cross-interactions for Lennard-Jones terms were calculated using the Lorentz-Berthelot mixing rules and intramolecular interactions between atom pairs separated up to three bonds were excluded. The TIP3P force field was used to describe water molecules.[2] A single solute molecule was dissolved in a cubic box containing at least 3500 water molecules for acetone MD and at least 4000 water molecules in case of dye(s) MDs. The molecular systems were initially brought to 0 K applying the steepest descent minimization procedure and then heated to 298.15 K in an NVT ensemble using the velocity-rescaling[3] method with an integration time step of 0.1 fs and a coupling constant of 0.1 ps for 100 ps. A 200 ps long NPT run was then performed, using the Parrinello–Rahman barostat and a coupling constant of 1.0 ps, to obtain a uniform distribution of molecules in the box and for thermalization purposes. 20 ns long production runs were then carried out in the NVT ensemble, with 1 fs time step. All MD runs were performed by using the GROMACS package.[4]

# S2 Genetic Algorithm Procedure

In order to refine dihedral angle parameters, we exploited a genetic algorithm (GA), which is an evolutionary algorithm that mimics the process of natural selection.[5] In particular, we used the Pyevolve module[6] to refine the potential energy surface of the $\delta$ dihedral angle of acetone (see Fig. 2 in the main text). In the standard parametrization engines such us ANTECHAMBER[7] or JOYCE,[8] improper dihedral angles are usually described as harmonic term due to their common rigidity. However this is not the case of acetone in its first excited

state (S1), where a semi-flexible nature can be clearly been identified in Fig. 7 in the main text (Black line). In order to obtain a correct description of the energy profile, we exploit the following dihedral energetic energy $E_\delta$:

$$E_\delta = \frac{V_1}{2}[1 + cos(n_1\phi_1 - \gamma_1)] + \frac{V_2 b}{2}[1 + cos(n_2\phi_2 - \gamma_2)] \tag{S1}$$

which depends on seven parameters: $V_1$, $V_2$, $n_1$, $n_2$, $\gamma_1$, $\gamma_2$ and $b$, which can assume only 0 or 1 values. In this way, the algorithm is flexibility enough to exploit one or two torsion terms to properly fit the energy scan of the dihedral angle. In order to construct the cost function, we first set our reference data set as QM/PCM energy (CAM-B3LYP/aug-cc-pvdz) obtained by a conformational scan of the dihedral angle $\delta$ in between -40 and 40 degrees, with 1 degree step. In addition, we performed a classical MD conformational scan of acetone by taking into account only non-bonded terms into account. Then, RMSD is obtained as a square difference between reference data set, the sum of $E_{MMscan}$ and torsion energies obtained by using parameters randomly selected by the GA at each generations for each degree; the score function was then defined as 1/RMSD. The potential mean forces (PMF) as a function of the dihedral angles obtained by using the GA-derived FF are graphically depicted in Fig. S1, together with the PMF obtained by using JOYCE-derived FF.

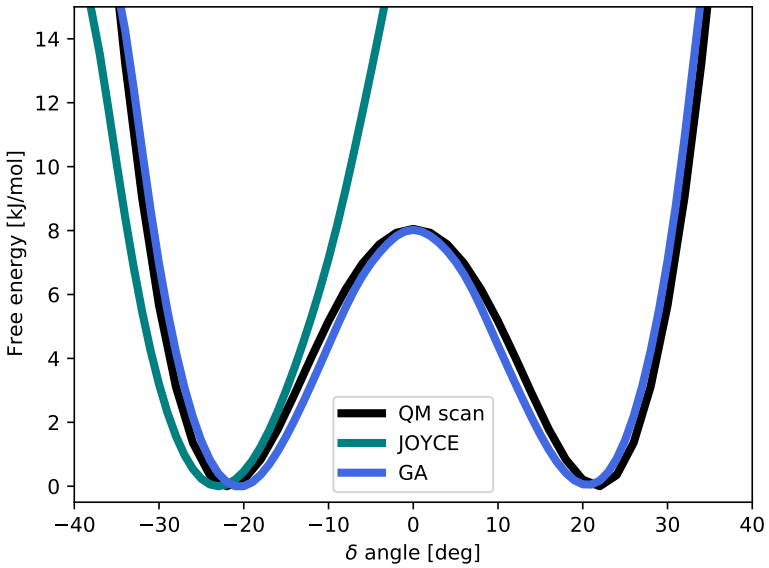


Figure S1: Potential of mean force (PMF) of the improper dihedral angle $\delta$ obtained by using JOYCE and GA derived FFs. The reference QM scan is also depicted as a black line.

# S3 Acetone in aqueous solution

Table S1: Experimental absorption and emission energies of acetone in gas phase and aqueous solution. (t.w.: this work)

| Gas Phase | Aqueous solution | Solvatochromic shift |
|---|---|---|
| 4.46,[9] 4.47[10] | 4.68 (t.w.) | 0.21-0.22 |
| 3.04[10] | 3.03, 3.04[10] | 0.0 ± 0.01 |

Table S2: QM/FQ and QM/FQ+rep (in parentheses) absorption and emission energies (eV) as computed from $MD_{GAFF}$, $MD_{REFINED}$ and $MD_{QM/MM}$. $QM_{QM/PCM}$in parenthesis in case of $QM_{PCM}$.

| Absorption Energy | | | | |
|---|---|---|---|---|
| | $MD_{GAFF}$ | $MD_{REFINED}$ | $MD_{QM/MM}$ | $QM_{PCM}$ |
| Vacuum | 4.25 | 4.37 | 4.42 | 4.46 |
| Water | 4.39 (4.36) | 4.74 (4.62) | 4.75 (4.61) | 4.56 (4.84) |

| Emission Energy | | | | |
|---|---|---|---|---|
| | $MD_{GAFF}$ | $MD_{REFINED}$ | $MD_{QM/MM}$ | $QM_{PCM}$ |
| Vacuum | - | 3.282 | - | 3.17 |
| Water | - | 3.304 (3.276) | - | 3.21 (3.24) |

Table S3: QM/FQ and QM/FQ+rep (in parentheses) calculated absorption and emission solvatochromic shifts ($\Delta_{abs}$ and $\Delta_{ems}$, respectively) as computed from $MD_{GAFF}$, $MD_{REFINED}$ and $MD_{QM/MM}$. The $MD_{REFINED}$ Stokes shifts ($\Delta_{Stokes}$) are also reported, together with QM/PCM and QM/QMw/PCM results. All energies are given in eV.

| | $MD_{GAFF}$ | $MD_{REFINED}$ | $MD_{QM/MM}$ | QM/PCM | QM/QMw/PCM | Exp |
|---|---|---|---|---|---|---|
| $\Delta_{abs}$ | 0.15 (0.11) | 0.37 (0.25) | 0.33 (0.19) | 0.08 | 0.38 | 0.21-0.22 |
| $\Delta_{ems}$ | - | 0.022 (-0.006) | - | 0.04 | 0.07 | -0.01 - 0.0 |
| $\Delta_{Stokes}$ | - | 1.44 (1.35) | - | 1.33 | 1.60 | 1.65 |

Table S4: Calculation times for classical MD and adiabatic QM/MM for S0 and S1 state of Acetone. 1 fs timestep.

| State | $MD_{GAFF}$ or $MD_{REFINED}$ | $MD_{QM/MM}$ |
|---|---|---|
| S0 | 69.15 ns/day | 5.3 ps/day |
| S1 | 69.15 ns/day | 1.4 ps/day |

Table S5: Acetone QM/FQ and QM/FQ+rep full width at half maximum (FWHM, eV) as obtained from $MD_{GAFF}$, $MD_{REFINED}$and $MD_{QM/MM}$calculations. The experimental FWHM is also given

| Sampling | Method | FWHM (eV) |
|---|---|---|
| $MD_{GAFF}$ | QM/FQ | 0.42 |
| | QM/FQ+rep | 0.42 |
| $MD_{REFINED}$ | QM/FQ | 0.48 |
| | QM/FQ+rep | 0.26 |
| $MD_{QM/MM}$ | QM/FQ | 0.46 |
| | QM/FQ+rep | 0.38 |
| Exp | | 0.74 |

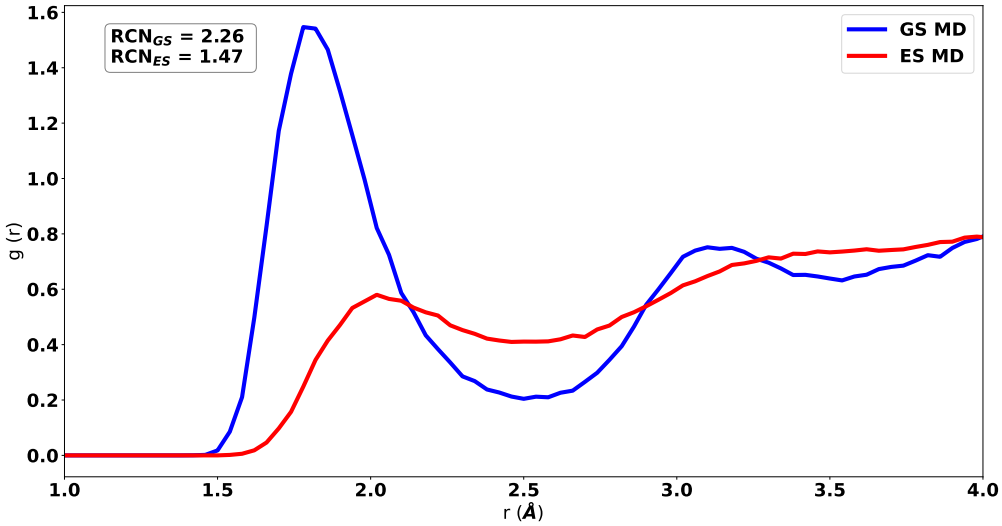


Figure S2: Radial distribution functions (RDFs) between Acetone Oxygen atom and water Hydrogen atoms obtained from ground state (GS) and excited state (ES) $MD_{REFINED}$ trajectories. The running coordination numbers (RCN) are reported.

# S4 Dyes in aqueous solution

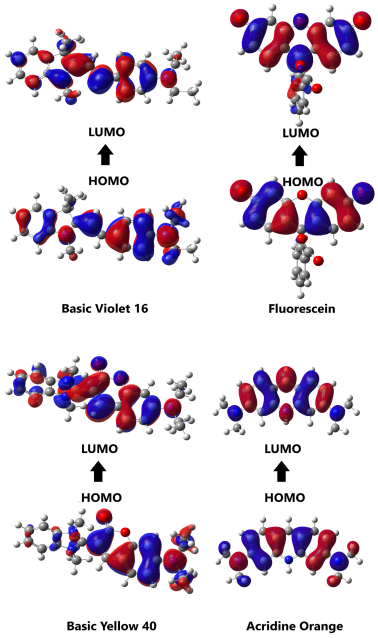


Figure S3: Molecular Orbitals involved in the first electronic transition of the studied fluorophore. Isovalue: 0.02.

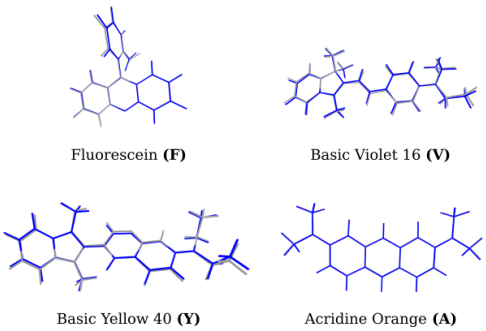


Figure S4: Superposition of ground state (blue) and excited state S1 (grey) geometries.

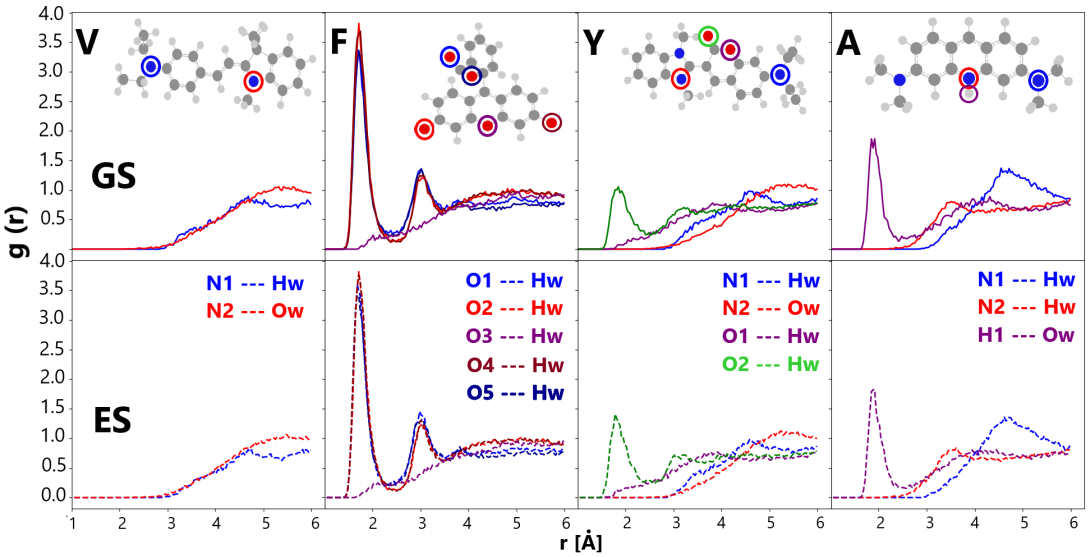


Figure S5: Basic Violet 16 (V), Fluorescein (F), Basic Yellow 40 (Y) and Acridine Orange (A) GS (solid line) and ES (dashed line) Radial Distribution Functions (RDF) between highlighted atoms (see top panel) and the specified water atoms (Hw, Ow).

Table S6: Basic Violet 16 (V), Fluorescein (F), Basic Yellow 40 (Y) and Acridine Orange (A) calculated and experimental FWHM for absorption and emission spectra.

| Molecule | Abs. | | Abs. | |
|---|---|---|---|---|
| | Calc. | Exp. | Calc. | Exp. |
| **V** | 0.32 | 0.32 | 0.24 | 0.20 |
| **F** | 0.26 | 0.18 | 0.26 | 0.16 |
| **Y** | 0.32 | 0.36 | 0.32 | 0.28 |
| **A** | 0.30 | 0.20 | 0.24 | 0.26 |

# References


(1) Darden, T.; York, D.; Pedersen, L. Particle mesh Ewald: An Nlog(N) method for Ewald sums in large systems. *J. Chem. Phys.* **1993**, *98*, 10089–10092.

(2) Mark, P.; Nilsson, L. Structure and dynamics of the TIP3P, SPC, and SPC/E water models at 298 K. *J. Phys. Chem. A* **2001**, *105*, 9954–9960.

(3) Bussi, G.; Donadio, D.; Parrinello, M. Canonical sampling through velocity rescaling. *J. Chem. Phys.* **2007**, *126*, 014101.

(4) Pronk, S.; Pall, S.; Schulz, R.; Larsson, P.; Bjelkmar, P.; Apostolov, R.; Shirts, M. R.; Smith, J. C.; Kasson, P. M.; van der Spoel, D.; Hess, B.; Lindahl, E. GROMACS 4.5: a high-throughput and highly parallel open source molecular simulation toolkit. *Bioinformatics* **2013**, *29*, 845–854.

(5) Kramer, O. *Genetic Algorithm Essentials*; Springer International Publishing: Cham, 2017; pp 11–19.

(6) Perone, C. S. Pyevolve: A Python Open-Source Framework for Genetic Algorithms. *SIGEVOlution* **2009**, *4*, 12–20.

(7) Sousa da Silva, A. W.; Vranken, W. F. ACPYPE-Antechamber python parser interface. *BMC research notes* **2012**, *5*, 1–8.

(8) Barone, V.; Cacelli, I.; De Mitri, N.; Licari, D.; Monti, S.; Prampolini, G. J oyce and U lysses: integrated and user-friendly tools for the parameterization of intramolecular force fields from quantum mechanical data. *Phys. Chem. Chem. Phys.* **2013**, *15*, 3736–3751.

(9) Renge, I. Solvent Dependence of n- $\pi^*$ Absorption in Acetone. *J. Phys. Chem.* **2009**, *113*, 10678–10686.

(10) Catalán, J.; Catalán, J. P. On the solvatochromism of the n-$\pi^*$ electronic transitions in ketones. *Phys. Chem. Chem. Phys.* **2011**, *13*, 4072–4082.

# CHAPTER 6

## Summary and Conclusions

In this Thesis, some applications of a computational protocol, based on the polarizable QM/FQ model, to reproduce electronic absorption/fluoresce spectra and generally excited state properties, have been presented.
As a sampling method, MD has been used, which has been refined so to improve the description of the directionality of HB interactions (intermolecular) and the quality of interatomic potentials (intramolecular).
In the first part of the Thesis, UV-Vis absorption spectra of four flavonoids, dissolved in aqueous solution have been simulated by exploiting the fully polarizable QM/FQ approach combined with MD simulations, which are performed by either including or discarding off-site VSs. MD analysis has shown that both $MD_{noVS}$ and $MD_{VS}$ explore the configurational space in a similar way, whereas a different description of solute–solvent HB interactions is observed. Computed QM/FQ spectra of each flavonoid on a set of snapshots extracted from both MD trajectories have been analyzed, in light of solute–solvent HB interactions. In particular, the presence of a larger number of potential HB sites, as in the case of Quercetin and Myricetin as compared to Luteolin and Kaempferol, produces a redshift of the first electronic excitation, which has a $\pi \rightarrow \pi^{\star}$ nature. Finally, the comparison between computed and experimental spectra shows that $MD_{VS}$ provides the best agreement, especially due to a better HB description.
In the second part, the applicability of QM/FQ has been extended to different solvents of various polarities. The novel parametrization has been tested to reproduce solvatochromic shifts of four dyes dissolved in various solvents, and has also demonstrated a good level of transferability for molecules with similar chemical structures. Results obtained for all solvents have been compared with experimental shifts, as also obtained by exploiting

other computational approaches. Remarkably, in most cases, QM/FQ results are in much better agreement with the experimental values than other approaches, which lack the description of polarization effects (QM/EE) or any atomistic description of the solvent molecules (QM/PCM).

In the last part of the thesis, we have presented the first extension of QM/FQ to fluorescence spectra. Emission is a complex phenomenon, which requires specific computational protocols to be accurately modelled. Our computational protocol involves two main steps: 1) a pragmatic approach to obtain an accurate sampling of the excited molecule-solvent phase space, followed by 2) a reliable QM/MM modeling of emission properties, that fully takes molecule-environment interactions into consideration. In order to achieve accurate sampling in the first step, re-parametrization of classical FFs based on ES QM reference data has been done. State-of-the-art quantum-mechanical simulations, describing the aqueous environment through the QM/FQ approach, with the additional inclusion of Pauli repulsion effects, have been employed to obtain the final spectra. The protocol has been first tested against the reproduction of the absorption and emission solvatochromic shifts of the Acetone, then compared with experimental data. As a result, our method not only provides an almost perfect agreement with measured experimental data, but also with more sophisticated, and much more computationally demanding, approaches. To further demonstrate the applicability of the approach, four fluorescent dyes have been studied. Remarkably, the model accurately reproduced the Stokes shift of all dyes in aqueous solution, which further proves that a proper sampling of the GS/ES and a physically consistent description of the main physicochemical solute-solvent interactions make the model able to accurately reproduce a variety of experimental spectral features.

To conclude, the results of this Thesis, and the developed protocols, pave the way for future QM/FQ studies of excited state properties and spectra of systems embedded in generic environments, including different solutions, biological matrices, and surfaces, with the possibility of studying multiple excited states, at a reasonably low computational cost.

# Bibliography


[1] Welton, T.; Reichardt, C. *Solvents and solvent effects in organic chemistry*; John Wiley & Sons, 2011.

[2] De Alencastro, R. B.; Da Motta Neto, J. D.; Zerner, M. C. *International Journal of Quantum Chemistry* **1994**, *52*, 361–377.

[3] Dreuw, A.; Head-Gordon, M. *Chemical reviews* **2005**, *105*, 4009–4037.

[4] Stanton, J. F.; Bartlett, R. J. *The Journal of chemical physics* **1993**, *98*, 7029–7039.

[5] Jacquemin, D.; Wathelet, V.; Perpete, E. A.; Adamo, C. *J. Chem. Theory Comput.* **2009**, *5*, 2420–2435.

[6] Jacquemin, D.; Perpete, E. A.; Scuseria, G. E.; Ciofini, I.; Adamo, C. *J. Chem. Theory Comput.* **2008**, *4*, 123–135.

[7] Laurent, A. D.; Jacquemin, D. *Int. J. Quantum Chem.* **2013**, *113*, 2019–2039.

[8] Li, J.; Cramer, C. J.; Truhlar, D. G. *Int. J. Quantum Chem.* **2000**, *77*, 264–280.

[9] Silva-Junior, M. R.; Schreiber, M.; Sauer, S. P.; Thiel, W. *J. Chem. Phys.* **2008**, *129*, 104103.

[10] Caricato, M.; Trucks, G. W.; Frisch, M. J.; Wiberg, K. B. *J. Chem. Theory Comput.* **2010**, *6*, 370–383.

[11] Isegawa, M.; Peverati, R.; Truhlar, D. G. *J. Chem. Phys.* **2012**, *137*, 244104.

[12] Isegawa, M.; Truhlar, D. G. *J. Chem. Phys.* **2013**, *138*, 134111.

[13] Alipour, M. *Theor. Chem. Acc.* **2016**, *135*, 67.

[14] Maier, T. M.; Bahmann, H.; Arbuznikov, A. V.; Kaupp, M. *J. Chem. Phys.* **2016**, *144*, 074106.

[15] Jacquemin, D.; Planchat, A.; Adamo, C.; Mennucci, B. *J. Chem. Theory and Comput.* **2012**, *8*, 2359–2372.

[16] Jacquemin, D.; Mennucci, B.; Adamo, C. *Phys. Chem. Chem. Phys.* **2011**, *13*, 16987–16998.

[17] Reichardt, C. *Chem. Soc. Rev.* **1992**, *21*, 147–153.

[18] Buncel, E.; Rajagopal, S. *Acc. Chem. Res.* **1990**, *23*, 226–231.

[19] Reichardt, C. *Chem. Rev.* **1994**, *94*, 2319–2358.

[20] Cannelli, O.; Giovannini, T.; Baiardi, A.; Carlotti, B.; Elisei, F.; Cappelli, C. *Phys. Chem. Chem. Phys.* **2017**, *19*, 32544–32555.

[21] Prampolini, G.; Bellina, F.; Biczysko, M.; Cappelli, C.; Carta, L.; Lessi, M.; Pucci, A.; Ruggeri, G.; Barone, V. *Chemistry Eur. J.* **2013**, *19*, 1996–2004.

[22] Tosi, I.; Segado Centellas, M.; Campioli, E.; Iagatti, A.; Lapini, A.; Sissa, C.; Baldini, L.; Cappelli, C.; Di Donato, M.; Sansone, F.; Santoro, F.; Terenziani, F. *ChemPhysChem* **2016**, *17*, 1686–1706.

[23] Carlotti, B.; Cesaretti, A.; Cannelli, O.; Giovannini, T.; Cappelli, C.; Bonaccorso, C.; Fortuna, C. G.; Elisei, F.; Spalletti, A. *J. Phys. Chem. C* **2018**, *122*, 2285–2296.

[24] Lapini, A.; Fabbrizzi, P.; Piccardo, M.; di Donato, M.; Lascialfari, L.; Foggi, P.; Cicchi, S.; Biczysko, M.; Carnimeo, I.; Santoro, F.; Cappelli, C.; Righini, R. *Phys. Chem. Chem. Phys.* **2014**, *16*, 10059–10074.

[25] Budzák, S.; Laurent, A. D.; Laurence, C.; Medved', M.; Jacquemin, D. *J. Chem. Theory Comput.* **2016**, *12*, 1919–1929.

[26] Mennucci, B.; Cappelli, C.; Guido, C. A.; Cammi, R.; Tomasi, J. *The Journal of Physical Chemistry A* **2009**, *113*, 3009–3020.

[27] Marenich, A. V.; Cramer, C. J.; Truhlar, D. G.; Guido, C. A.; Mennucci, B.; Scalmani, G.; Frisch, M. J. *Chem. Sci.* **2011**, *2*, 2143–2161.

[28] Labat, F.; Le Bahers, T.; Ciofini, I.; Adamo, C. *Acc. Chem. Res.* **2012**, *45*, 1268–1277.

[29] Tomasi, J.; Cammi, R.; Mennucci, B.; Cappelli, C.; Corni, S. *Phys. Chem. Chem. Phys.* **2002**, *4*, 5697–5712.

[30] Mennucci, B., Cammi, R., Eds. *Continuum Solvation Models in Chemical Physics*; Wiley, New York, 2007.

[31] Tomasi, J.; Mennucci, B.; Cammi, R. *Chem. Rev.* **2005**, *105*, 2999–3094.

[32] Barone, V.; Cossi, M. *J. Phys. Chem A* **1998**, *102*, 1995–2001.

[33] Loco, D.; Polack, É.; Caprasecca, S.; Lagardere, L.; Lipparini, F.; Piquemal, J.-P.; Mennucci, B. *J. Chem. Theory Comput.* **2016**, *12*, 3654–3661.

[34] Cappelli, C.; Mennucci, B.; Monti, S. *J. Phys. Chem. A* **2005**, *109*, 1933–1943.

[35] Egidi, F.; Russo, R.; Carnimeo, I.; D'Urso, A.; Mancini, G.; Cappelli, C. *J. Phys. Chem. A* **2015**, *119*, 5396–5404.

[36] Thole, B. T. *Chem. Phys.* **1981**, *59*, 341–350.

[37] Steindal, A. H.; Ruud, K.; Frediani, L.; Aidas, K.; Kongsted, J. *J. Phys. Chem. B* **2011**, *115*, 3027–3037.

[38] Jurinovich, S.; Curutchet, C.; Mennucci, B. *ChemPhysChem* **2014**, *15*, 3194–3204.

[39] Donati, G.; Wildman, A.; Caprasecca, S.; Lingerfelt, D. B.; Lipparini, F.; Mennucci, B.; Li, X. *J. Phys. Chem. Lett.* **2017**, *8*, 5283–5289.

[40] Giovannini, T.; Egidi, F.; Cappelli, C. *Chemical Society Reviews* **2020**, *49*, 5664–5677.

[41] Giovannini, T.; Egidi, F.; Cappelli, C. *Physical Chemistry Chemical Physics* **2020**, *22*, 22864–22879.

[42] Cappelli, C. *Int. J. Quantum Chem.* **2016**, *116*, 1532–1542.

[43] Giovannini, T.; Olszòwka, M.; Egidi, F.; Cheeseman, J. R.; Scalmani, G.; Cappelli, C. *J. Chem. Theory Comput.* **2017**, *13*, 4421–4435.

[44] Lipparini, F.; Cappelli, C.; Scalmani, G.; De Mitri, N.; Barone, V. *J. Chem. Theory Comput.* **2012**, *8*, 4270–4278.

[45] Lipparini, F.; Cappelli, C.; Barone, V. *J. Chem. Phys.* **2013**, *138*, 234108.

[46] Lipparini, F.; Cappelli, C.; Barone, V. *J. Chem. Theory Comput.* **2012**, *8*, 4153–4165.

[47] Giovannini, T.; Riso, R. R.; Ambrosetti, M.; Puglisi, A.; Cappelli, C. *J. Chem. Phys.* **2019**, *151*, 174104.

[48] Carnimeo, I.; Cappelli, C.; Barone, V. *J. Comput. Chem.* **2015**, *36*, 2271–2290.

[49] Hansson, T.; Oostenbrink, C.; van Gunsteren, W. *Current opinion in structural biology* **2002**, *12*, 190–196.

[50] Monticelli, L.; Tieleman, D. P. *Biomolecular simulations* **2013**, 197–213.

[51] Barone, V.; Cacelli, I.; De Mitri, N.; Licari, D.; Monti, S.; Prampolini, G. *Physical Chemistry Chemical Physics* **2013**, *15*, 3736–3751.

[52] Faheem, A. B.; Kim, J.-Y.; Bae, S.-E.; Lee, K.-K. *Journal of Molecular Liquids* **2021**, *337*, 116579.

[53] Wang, J.; Wolf, R. M.; Caldwell, J. W.; Kollman, P. A.; Case, D. A. *Journal of computational chemistry* **2004**, *25*, 1157–1174.

[54] Vanommeslaeghe, K.; Hatcher, E.; Acharya, C.; Kundu, S.; Zhong, S.; Shim, J.; Darian, E.; Guvench, O.; Lopes, P.; Vorobyov, I., et al. *Journal of computational chemistry* **2010**, *31*, 671–690.

[55] Shivakumar, D.; Williams, J.; Wu, Y.; Damm, W.; Shelley, J.; Sherman, W. *Journal of chemical theory and computation* **2010**, *6*, 1509–1519.

[56] Wang, J.; Kollman, P. A. *Journal of Computational Chemistry* **2001**, *22*, 1219–1228.

[57] Harder, E.; Damm, W.; Maple, J.; Wu, C.; Reboul, M.; Xiang, J. Y.; Wang, L.; Lupyan, D.; Dahlgren, M. K.; Knight, J. L., et al. *Journal of chemical theory and computation* **2016**, *12*, 281–296.

[58] Macchiagodena, M.; Mancini, G.; Pagliai, M.; Barone, V. *Physical Chemistry Chemical Physics* **2016**, *18*, 25342–25354.

[59] Egidi, F.; Giovannini, T.; Del Frate, G.; Lemler, P. M.; Vaccaro, P. H.; Cappelli, C. *Phys. Chem. Chem. Phys.* **2019**, *21*, 3644–3655.

[60] Lamoureux, G.; MacKerell Jr, A. D.; Roux, B. *J. Chem. Phys.* **2003**, *119*, 5185–5197.

[61] Lamoureux, G.; Roux, B. *J. Chem. Phys.* **2003**, *119*, 3025–3039.

[62] Anisimov, V. M.; Lamoureux, G.; Vorobyov, I. V.; Huang, N.; Roux, B.; MacKerell, A. D. *J. Chem. Theory Comput.* **2005**, *1*, 153–168.

[63] Lemkul, J. A.; Huang, J.; Roux, B.; MacKerell Jr, A. D. *Chem. Rev.* **2016**, *116*, 4983–5013.

[64] Geerke, D.; van Gunsteren, W. F. *Mol. Phys.* **2007**, *105*, 1861–1881.

[65] Boulanger, E.; Thiel, W. *J. Chem. Theory Comput.* **2012**, *8*, 4527–4538.

[66] Geerke, D. P.; Thiel, S.; Thiel, W.; van Gunsteren, W. F. *J. Chem. Theory Comput.* **2007**, *3*, 1499–1509.

[67] Boulanger, E.; Thiel, W. *J. Chem. Theory Comput.* **2014**, *10*, 1795–1809.

[68] Huang, J.; Simmonett, A. C.; Pickard IV, F. C.; MacKerell Jr, A. D.; Brooks, B. R. *J. Chem. Phys.* **2017**, *147*, 161702.

[69] Caprasecca, S.; Jurinovich, S.; Viani, L.; Curutchet, C.; Mennucci, B. *J. Chem. Theory Comput.* **2014**, *10*, 1588–1598.

[70] Jurinovich, S.; Pescitelli, G.; Di Bari, L.; Mennucci, B. *Phys. Chem. Chem. Phys.* **2014**, *16*, 16407–16418.

[71] Curutchet, C.; Muñoz-Losa, A.; Monti, S.; Kongsted, J.; Scholes, G. D.; Mennucci, B. *J. Chem. Theory Comput.* **2009**, *5*, 1838–1848.

[72] Curutchet, C.; Kongsted, J.; Muñoz-Losa, A.; Hossein-Nejad, H.; Scholes, G. D.; Mennucci, B. *J. Am. Chem. Soc.* **2011**, *133*, 3078–3084.

[73] Loco, D.; Jurinovich, S.; Cupellini, L.; Menger, M. F.; Mennucci, B. *Photochem. Photobiol. Sci.* **2018**, *17*, 552–560.

[74] Caprasecca, S.; Cupellini, L.; Jurinovich, S.; Loco, D.; Lipparini, F.; Mennucci, B. *Theor. Chem. Acc.* **2018**, *137*, 84.

[75] Ren, S.; Lipparini, F.; Mennucci, B.; Caricato, M. *Journal of Chemical Theory and Computation* **2019**, *15*, 4485–4496.

[76] Thompson, M. A. *J. Phys. Chem.* **1996**, *100*, 14492–14507.

[77] Marini, A.; Muñoz-Losa, A.; Biancardi, A.; Mennucci, B. *J. Phys. Chem. B* **2010**, *114*, 17128–17135.

[78] Jacobson, L. D.; Herbert, J. M. *J. Chem. Phys.* **2010**, *133*, 154506.

[79] Shi, Y.; Xia, Z.; Zhang, J.; Best, R.; Wu, C.; Ponder, J. W.; Ren, P. *J. Chem. Theory Comput.* **2013**, *9*, 4046–4063.

[80] Dziedzic, J.; Mao, Y.; Shao, Y.; Ponder, J.; Head-Gordon, T.; Head-Gordon, M.; Skylaris, C.-K. *J. Chem. Phys.* **2016**, *145*, 124106.

[81] Loco, D.; Buda, F.; Lugtenburg, J.; Mennucci, B. *J. Phys. Chem. Lett.* **2018**, *9*, 2404–2410.

[82] Loco, D.; Cupellini, L. *Int. J. Quantum Chem.* **2018**, DOI: 10.1002/qua.25726.

[83] Mao, Y.; Shao, Y.; Dziedzic, J.; Skylaris, C.-K.; Head-Gordon, T.; Head-Gordon, M. *J. Chem. Theory Comput.* **2017**, *13*, 1963–1979.

[84] Nottoli, M.; Mennucci, B.; Lipparini, F. *Physical Chemistry Chemical Physics* **2020**, *22*, 19532–19541.

[85] Rick, S. W.; Stuart, S. J.; Berne, B. J. *J. Chem. Phys.* **1994**, *101*, 6141–6156.

[86] Rick, S. W.; Stuart, S. J.; Bader, J. S.; Berne, B. *J. Mol. Liq.* **1995**, *65*, 31–40.

[87] Rick, S. W.; Berne, B. J. *J. Am. Chem. Soc.* **1996**, *118*, 672–679.

[88] Lipparini, F.; Egidi, F.; Cappelli, C.; Barone, V. *J. Chem. Theory Comput.* **2013**, *9*, 1880–1884.

[89] Egidi, F.; Carnimeo, I.; Cappelli, C. *Opt. Mater. Express* **2015**, *5*, 196–209.

[90] Giovannini, T.; Olszowka, M.; Cappelli, C. *J. Chem. Theory Comput.* **2016**, *12*, 5483–5492.

[91] Giovannini, T.; Del Frate, G.; Lafiosca, P.; Cappelli, C. *Phys. Chem. Chem. Phys.* **2018**, *20*, 9181–9197.

[92] Giovannini, T.; Ambrosetti, M.; Cappelli, C. *Theor. Chem. Acc.* **2018**, *137*, 74.

[93] Giovannini, T.; Macchiagodena, M.; Ambrosetti, M.; Puglisi, A.; Lafiosca, P.; Lo Gerfo, G.; Egidi, F.; Cappelli, C. *Int. J. Quantum Chem.* **2018**, e25684.

[94] Egidi, F.; Lo Gerfo, G.; Macchiagodena, M.; Cappelli, C. *Theor. Chem. Acc.* **2018**, *137*, 82.

[95] Di Remigio, R.; Giovannini, T.; Ambrosetti, M.; Cappelli, C.; Frediani, L. *J. Chem. Theory Comput.* **2019**, *15*, 4056–4068, PMID: 31244130.

[96] Giovannini, T.; Ambrosetti, M.; Cappelli, C. *J. Phys. Chem. Lett.* **2019**, *10*, 5823–5829.

[97] Mortier, W. J.; Van Genechten, K.; Gasteiger, J. *J. Am. Chem. Soc.* **1985**, *107*, 829–835.

[98] Sanderson, R. *Science* **1951**, *114*, 670–672.

[99] Lipparini, F.; Barone, V. *J. Chem. Theory Comput.* **2011**, *7*, 3711–3724.

[100] Ohno, K. *Theor. Chim. Acta* **1964**, *2*, 219–227.

[101] Giovannini, T.; Puglisi, A.; Ambrosetti, M.; Cappelli, C. *J. Chem. Theory Comput.* **2019**, *15*, 2233–2245.

[102] Giovannini, T.; Grazioli, L.; Ambrosetti, M.; Cappelli, C. *Journal of Chemical Theory and Computation* **2019**, *15*, 5495–5507.

[103] Gómez, S. A.; Rojas-Valencia, N.; Gómez, S.; Egidi, F.; Cappelli, C.; Restrepo, A. *ChemBioChem* **2021**, *22*, 724–732.

[104] Marrazzini, G.; Giovannini, T.; Egidi, F.; Cappelli, C. *J. Chem. Theory Comput.* **2020**, *16*, 6993–7004.

[105] Giovannini, T.; Lafiosca, P.; Cappelli, C. *J. Chem. Theory Comput.* **2017**, *13*, 4854–4870.

[106] Giovannini, T.; Lafiosca, P.; Chandramouli, B.; Barone, V.; Cappelli, C. *J. Chem. Phys.* **2019**, *150*, 124102.

[107] Tkatchenko, A.; Scheffler, M. *Phys. Rev. Lett.* **2009**, *102*, 073005.

[108] Tkatchenko, A.; Romaner, L.; Hofmann, O. T.; Zojer, E.; Ambrosch-Draxl, C.; Scheffler, M. *MRS bulletin* **2010**, *35*, 435–442.

[109] Tkatchenko, A.; DiStasio Jr, R. A.; Car, R.; Scheffler, M. *Phys. Rev. Lett.* **2012**, *108*, 236402.

[110] Hermann, J.; DiStasio, R. A.; Tkatchenko, A. *Chem. Rev.* **2017**, *117*, 4714–4758.

[111] Giovannini, T.; Egidi, F.; Cappelli, C. *Chem. Soc. Rev.* **2020**, *49*, 5664–5677.